

Contact mechanics in glassy polymers

Citation for published version (APA):

Breemen, van, L. C. A. (2009). *Contact mechanics in glassy polymers*. [Phd Thesis 1 (Research TU/e / Graduation TU/e), Mechanical Engineering]. Technische Universiteit Eindhoven.
<https://doi.org/10.6100/IR642891>

DOI:

[10.6100/IR642891](https://doi.org/10.6100/IR642891)

Document status and date:

Published: 01/01/2009

Document Version:

Publisher's PDF, also known as Version of Record (includes final page, issue and volume numbers)

Please check the document version of this publication:

- A submitted manuscript is the version of the article upon submission and before peer-review. There can be important differences between the submitted version and the official published version of record. People interested in the research are advised to contact the author for the final version of the publication, or visit the DOI to the publisher's website.
- The final author version and the galley proof are versions of the publication after peer review.
- The final published version features the final layout of the paper including the volume, issue and page numbers.

[Link to publication](#)

General rights

Copyright and moral rights for the publications made accessible in the public portal are retained by the authors and/or other copyright owners and it is a condition of accessing publications that users recognise and abide by the legal requirements associated with these rights.

- Users may download and print one copy of any publication from the public portal for the purpose of private study or research.
- You may not further distribute the material or use it for any profit-making activity or commercial gain
- You may freely distribute the URL identifying the publication in the public portal.

If the publication is distributed under the terms of Article 25fa of the Dutch Copyright Act, indicated by the "Taverne" license above, please follow below link for the End User Agreement:

www.tue.nl/taverne

Take down policy

If you believe that this document breaches copyright please contact us at:

openaccess@tue.nl

providing details and we will investigate your claim.

Contact mechanics in glassy polymers

Contact mechanics in glassy polymers/ by Lambert C.A. van Breemen.
Technische Universiteit Eindhoven, 2009.

A catalogue record is available from the Eindhoven University of Technology Library
ISBN 978-90-386-1861-6
NUR 971

Reproduction: University Press Facilities, Eindhoven, The Netherlands.
Cover design: Mark van Dosselaar.

This research forms part of the research programme of the Dutch Polymer Institute (DPI),
Technology Area Performance Polymers, DPI project #584.

Contact mechanics in glassy polymers

PROEFSCHRIFT

ter verkrijging van de graad van doctor aan de
Technische Universiteit Eindhoven, op gezag van de
rector magnificus, prof.dr.ir. C.J. van Duijn, voor een
commissie aangewezen door het College voor
Promoties in het openbaar te verdedigen
op maandag 22 juni 2009 om 16.00 uur

door

Lambèrt Cécile Angelo van Breemen

geboren te Velsen

Dit proefschrift is goedgekeurd door de promotoren:

prof.dr.ir. H.E.H. Meijer

en

prof.dr.ir. J.M.J. den Toonder

Copromotor:

dr.ir. L.E. Govaert

Contents

Summary	ix
1 Introduction	1
1.1 Tribology in a historical perspective	1
1.2 Simplifying complex tribological phenomena	2
1.3 Surface mechanics	4
1.4 Model and experimental requirements	6
Constitutive model	6
Indentation set-up	7
Single-asperity scratch set-up	8
1.5 Scope of this thesis	8
2 Constitutive modelling of polymer glasses: a multi-mode approach	11
Abstract	11
2.1 Introduction	13
2.2 Modelling	15
Numerical modelling	15
Spectrum determination	18
2.3 Experimental	22
Materials and sample preparation	22
Techniques	23
Numerical simulations	23
2.4 Results and discussion	23
Material characterization	23
Spectrum validation	25
Applications	27
2.5 Conclusions	31

3	Constitutive modelling of polymer glasses: a multi-mode-multi-process approach	33
	Abstract	33
3.1	Introduction	35
3.2	Materials and Methods	36
	Materials	36
	Methods	37
3.3	Phenomenology	37
3.4	Constitutive modelling	42
	The EGP-model for thermorheologically simple polymers	42
	Extension to thermorheologically complex polymers	44
3.5	Results and discussion	49
	Parameter characterization	49
	Application to PS and PLLA	49
	Application to PMMA	53
3.6	Conclusions	54
4	Flat-tip micro-indentation of glassy polymers	57
	Abstract	57
4.1	Introduction	59
4.2	Phenomenology	60
4.3	Experimental and numerical	62
	Materials and sample preparation	62
	Techniques	63
	Numerical simulations	64
4.4	Results and discussion	64
	Thermorheologically simple behaviour: PC	64
	Thermorheologically complex behaviour: PMMA	69
4.5	Conclusion	72
5	Single-asperity sliding friction	73
	Abstract	73
5.1	Introduction	75
5.2	Experimental	77
	Sample preparation	77
	Techniques	78
	Choice of tip geometry	79
	Effect of sample tilt	79
	Dependence on sliding velocity	80
5.3	Modelling	83
	Constitutive model	83

Finite element mesh	84
Influence of sliding velocity without friction	86
Influence of sliding velocity with friction	86
Influence of tip geometry	87
5.4 Conclusions	90
6 Conclusions, recommendations and challenges	93
6.1 Conclusions	93
6.2 Recommendations	95
6.3 Challenges	100
References	103
Samenvatting	114
Dankwoord	117
Curriculum vitae	119
List of publications	121

Summary

Polymers, primarily semi-crystalline, are widely used in applications where low friction is required; examples are cups in artificial hip joints, bearings and gears. Until now there is no clear indication why some polymers display low friction and others don't. In this thesis a systematic identification of the role of the intrinsic properties of glassy polymers on single-asperity sliding friction experiments is performed. The problem is analysed using a hybrid numerical/experimental technique. In the numerical part the interaction between indenter and polymer is studied by means of a constitutive model capturing the intrinsic behaviour of glassy polymers, where the interaction between tip and polymer can be influenced by the incorporation of existing friction models. The experimental section concerns the development of reproducible sliding friction experiments, which in a later stage can be compared with simulations before conclusions can be drawn. Starting point is the constitutive model developed in our group over the last decade, which accurately captures the deformation response of glassy polymers, including strain localization phenomena as well as life time predictions.

The choice for glassy polymers is, therefore, clearly not motivated by their relevance in low friction applications, but only because they represent a well-characterized class of polymers that allow quantitative predictions. First however some drawbacks of the existing model must be removed. The pre-yield regime itself is highly non-linear and thus correct modelling thereof is important in all simulations where non-homogeneous deformation is applied, like e.g. in indentation and sliding friction. Nevertheless, at present the pre-yield region is modelled as a compressible linear elastic solid and, as a result, details of indentation and unloading are not described quantitatively. The straightforward solution is to extend the existing model to include a spectrum of relaxation times in the pre-yield regime, via use of a multi-mode approach. The thus improved model now indeed also quantitatively predicts the indentation response of polycarbonate for different types of indenter geometries. A second drawback of the existing model is that it cannot deal with multiple relaxation mechanisms, as occur in cases where more than one molecular transition contributes to the stress. This behaviour typically manifests itself when high strain rates are applied, demonstrating a change in slope in the dependence of yield

stress on the logarithm of strain rate. Solution of this problem requires a model extension by incorporation of a second, additional, flow process with its own non-linearity, that is, a multi-process approach. A material which manifests this type of mechanical response is poly(methyl methacrylate); a quantitative prediction of its indentation response is achieved.

Generally the friction force is regarded to be an additive composition of a deformation- and an adhesion-related component, suggesting that components operate and contribute independently. Although decomposition in independent contributions is impossible to verify in an experimental set-up, it can be conveniently studied by using a numerical approach. Simulations with no adhesive interaction between tip and polymer show almost no influence of sliding velocity on friction force, whereas experiments show a significant influence. In case of an additive decomposition, this would imply a rate-dependence of the adhesive component. By inclusion of the Amontons-Coulomb friction law, which creates an interaction between tip and polymer, the suggested additive decomposition is proved not to be applicable and the large macroscopic deformation response proves to be the result of small changes in local processes. When interaction is taken into account, a bow wave is formed in front of the sliding tip, which leads to an increase in contact area between tip and polymer and results in an increase in friction force. As a consequence the experimentally observed time-dependent behaviour of the friction force can solely be attributed to a polymer's intrinsic deformation response. Furthermore the influence of a polymer's intrinsic material properties, such as strain hardening and the thermodynamic state, on the friction force can be studied conveniently.

CHAPTER ONE

Introduction

1.1 Tribology in a historical perspective

According to the Oxford dictionary [128] tribology is the science and technology of interacting surfaces in relative motion. It includes the study and application of the principles of friction, lubrication and wear. The word "tribology" is derived from the Greek "tribo" meaning to rub, and "logos" meaning principle or logic.

Leonardo da Vinci (1452–1519) was the first to state two laws of friction. The first law being that frictional resistance is the same for two different objects of the same weight, but making contacts over a different width and length. The second is that the force needed to overcome friction is doubled when the weight is doubled. Three centuries later (1699) Guillaume Amontons published the rediscovery of these laws of friction; they were later verified and extended by Charles-Augustin de Coulomb in 1781 to what is known as the three laws of friction:

1. The force of friction is directly proportional to the applied load, Amontons' 1st law.
2. The force of friction is independent of the apparent area of contact, Amontons' 2nd law.
3. Kinetic friction is independent of the sliding velocity, Coulomb's law.

These three laws are attributed to dry friction only, since lubrication modifies the tribological properties significantly. All these observations lead to the formulation of the Amontons-Coulomb law of friction:

$$\mu_a = \frac{F_f}{F_n}, \quad (1.1)$$

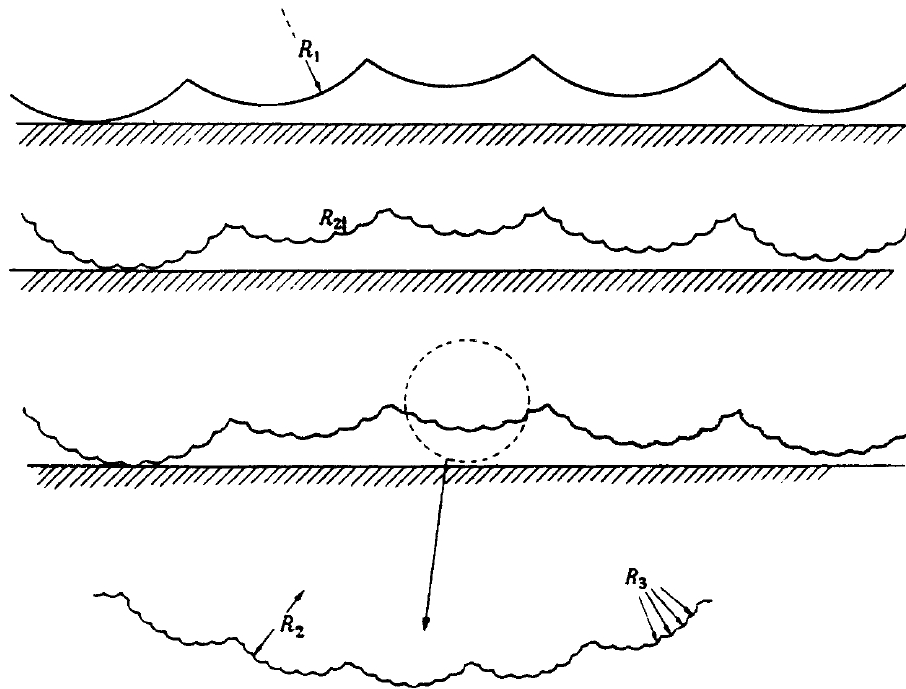


Figure 1.1: Archard's model [3] of multi-asperity roughness.

where μ_a is the apparent friction coefficient which is directly related to F_f , the friction force, and F_n , the normal load applied. Dry as well as lubricated friction theories were further developed in the twentieth century. From the large amount of publications on this subject every year, it can be concluded that friction and wear are rather complex phenomena, influenced by an astonishing amount of variables and still are, even after 500 years of research, not completely understood. To understand the underlying physical properties governing these events, the amount of external variables in an experimental set-up has to be reduced to a minimum. And that is what we are going to do in this thesis.

1.2 Simplifying complex tribological phenomena

For metal-metal interfaces, Bowden et al. [20] applied the adhesion concept of dry friction with great success. This principle is based on the force required to separate two bodies which are in contact, but it does contradict Amontons' second law where friction is independent on apparent area of contact. This contradiction was cleared by the introduction of the concept of real area of contact as proposed by Archard [3]. He based his idea on the hypothesis of 'protuberance on protuberance' or the more usual term as proposed by Bowden and Tabor 'multi-asperity contact' [20], see Figure 1.1. The real area of contact is defined by summing all small areas of contact where atom-to-atom contact takes place. This real contact area definition was statistically further refined by Greenwood and Williamson in their famous paper

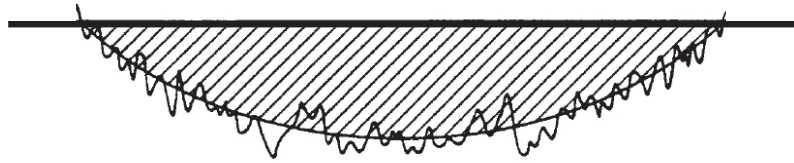


Figure 1.2: New definition of contact area proposed by Greenwood and Wu [65].

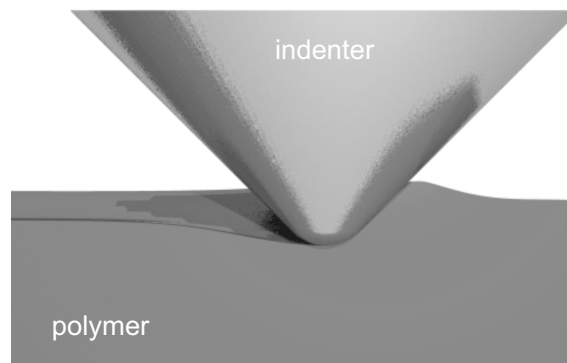


Figure 1.3: Single-asperity contact.

[64]; cited over 1300 times. They emphasize that, to describe contact between two bodies, an exact description of all asperities is of utmost importance. However, in the latest paper of the same Greenwood and Wu [65] entitled "Surface roughness and contact: an apology" they state that the summation of all small contact areas is generally the same to that of a smooth asperity of the same general shape, see Figure 1.2.

Applying this definition to a single-asperity scratch set-up, consisting of a contact area between a deformable polymer surface and a rigid diamond indenter surface, the topological properties of the asperities are obtained from the surface profile. This implies that the polymer can be considered as a flat surface and the indenter as a rigid smooth cone with a top radius and top angle specified by the tip geometry, hence obtaining single-asperity contacts, see Figure 1.3.

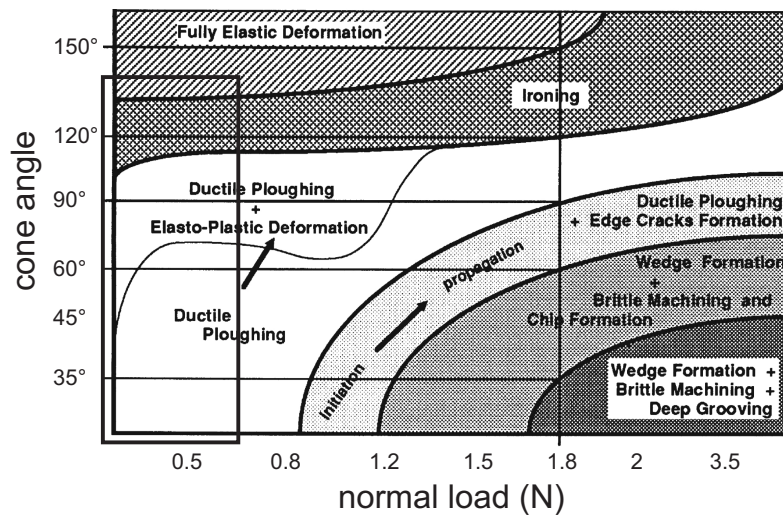
Typically in applications where high wear resistance or good frictional properties are required, semi-crystalline polymers are the obvious choice. As a model material they are not. This is mainly because their mechanical response is highly anisotropic, likewise the underlying failure mechanisms are not well understood and, as a result, characterization turns out to be complex. The choice of a glassy polymer as model material is therefore preferred. The core material to be explored is polycarbonate since this can be considered, from a mechanical point of view, both experimentally and numerically, by far the best characterized material.

Well defined experiments, where the amount of variables is kept at a minimum, are essential for a good understanding of the friction and wear response of any material. Because a single-asperity sliding friction experiment starts either with an initial indentation to a chosen normal force, which is kept constant during sliding, or a transient indentation, caused by an increasing normal force during sliding, the indentation response itself (no sliding), is studied first.

1.3 Surface mechanics

With indentation only, a whole world of thin film mechanics is exposed. Several groups are, or have been, working on obtaining intrinsic mechanical properties, such as the elastic modulus, yield strength and even visco-elastic properties, out of thin films via indentation. There are even groups who claim that they can predict a tensile test from an indentation experiment [81]. This is not realistic, since capturing strain softening out of an indentation test is, due to the local non-homogeneous deformation, that is the deformation around the tip-region, not possible. The largest drawback can, however, be found in the way of analysing the experimental data; typically one uses a method proposed almost fifteen years ago by Oliver and Pharr [110], but the fact that the underlying theory holds for materials responding fully elastically upon unloading, such as inorganic glasses, is commonly neglected. In the case of polymers, which display time-dependent (visco-elastic-visco-plastic) behaviour, this assumption is therefore far from correct. Distinctive material responses like piling-up and sinking-in cannot be captured with this approach. These experimental observations should be captured correctly before assessing single-asperity sliding friction experiments.

Conventionally the single-asperity scratch test is used as a tool to analyse a wide range of surface mechanical properties. In some areas the test is successfully applied in relating properties such as normal hardness to scratch hardness, characterization of coatings, modelling of wear and different material deformation characteristics when subjected to a hard asperity (single-asperity sliding). Especially the group of Briscoe generated a large quantity of experimental data on scratching with a hard asperity on several polymer glasses, be it cones with different top angles and different normal loads applied, resulting in so called scratch maps; an example of such a scratch map for polycarbonate is depicted in Figure 1.4 [23]. These maps give insight in what kind of failure mechanisms occur for different load-tip combinations. Based on these maps, regions of interest are defined which mark the experimental window. Obviously, first the regions which are governed by friction only are of interest (elastic, ironing and ductile ploughing), the marked region in Figure 1.4, before even considering the zones where also a wear response (ductile machining and crack formation to brittle machining) contributed to the behaviour observed.



(a)

response (pictorial)	generic	α
	elastic	180°
	ironing	150°
	ductile ploughing	120°
	ductile machining + cracking	90°
	↕	60°
		30°
	brittle machining	0°

(b)

Figure 1.4: Scratch map of polycarbonate taken from Briscoe [23] with a marked region which is considered in our single-asperity experiments; (a) cone angle versus normal load applied and (b) graphical representation of failure mechanisms observed.

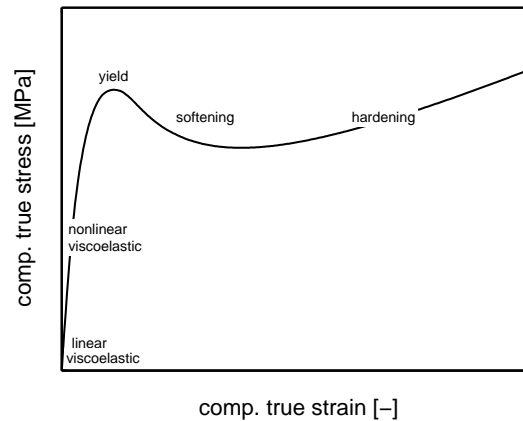


Figure 1.5: Intrinsic stress-strain response as observed in a uniaxial compression test; the specific intrinsic characteristics are denoted.

1.4 Model and experimental requirements

Constitutive model

Both indentation and single-asperity sliding require an adequate constitutive model capturing the intrinsic stress-strain response of polymer glasses. This response is observed when homogeneous deformation is applied to a sample, typically in uniaxial compression. The intrinsic characteristics as depicted in Figure 1.5 result. For the finite element analysis the Eindhoven Glassy Polymer (EGP)-model is employed. This model proves to be quantitative in capturing the yield stress as well as the post-yield response which is governed by strain softening and strain hardening. However, the pre-yield regime is modelled linear elastic whereas in reality a non-linear visco-elastic response is observed (see Figure 1.5). Considering especially the sliding friction experiment, where continuous unloading behind the tip occurs, a correct description of the non-linear visco-elastic characteristics of the intrinsic stress-strain response is required to obtain a quantitative prediction of the measured friction force, and of the post-mortem trace. Therefore the EGP-model is extended to a multi-mode model capturing the non-linear pre-yield regime via a spectrum of relaxation times and corresponding moduli, while keeping the post-yield response unaltered. This improved EGP-model is capable of capturing the complete intrinsic response of polymer glasses that behave thermorheologically simple (Chapter 2).

Thermorheological simplicity, that is a linear dependence of yield stress on the logarithm of strain rate applied, is rather an exception than a rule, since most polymers display a thermorheologically complex response; typically observed at high strain rates and/or low temperatures. It manifests itself as a change in slope when yield stress is plotted versus the logarithm of strain rate applied. The significance of capturing this intrinsic phenomenon is rationalized by the locally high deformation rates, i.e. the material response in the

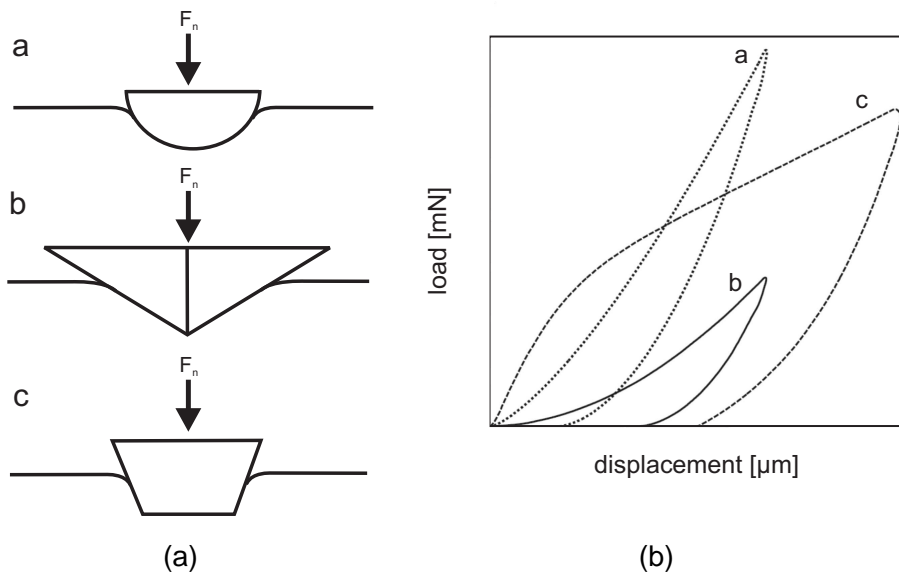


Figure 1.6: Influence of tip geometry on load displacement response: **a** represents a round tip, **b** Berkovich, and **c** flat-tip.

surrounding area of the indenter, as compared to the imposed sliding/indentation rates of the indenter. Consequently the multi-mode EGP-model is extended to a multi-mode-multi-process model capturing the thermorheologically complex behaviour of polymer glasses (Chapter 3). Simulation of indentation and sliding friction experiments requires implementation of the EGP-model in a finite element (FE) program. Here MSC.Marc is used, and implementation is achieved via the user-subroutine HYPELA2.

Indentation set-up

Two types of experiments are performed; the first is indentation, the second single-asperity sliding friction. In an indentation set-up the first choice concerns the type of indenter. Classic indentation uses a Berkovich tip, which is a three sided pyramid. Taking into account that this indenter needs to be modelled fully 3D in a FE analysis, a more obvious choice is a round indenter tip since it can be modelled axi-symmetrically, drastically reducing calculation time. As can be seen in Figure 1.6 a round tip gives a similar indentation response as the Berkovich tip. An alternative tip is the flat-punch indenter, that shows a pronounced difference in the load-displacement curve when compared to the other two indenter tips. Two distinct regimes can be identified, the first linear regime is considered *elastic*, the second *plastic*, with the yield point in-between where a change in slope is seen. Similar to the round indenter, FE modelling can be achieved by using an axi-symmetric model. The choice for the flat-punch indenter has one drawback which is its sensitivity to sample-tip misalignment. This problem was solved [112] by the development of the sample-tilt stage, see Figure 1.7.

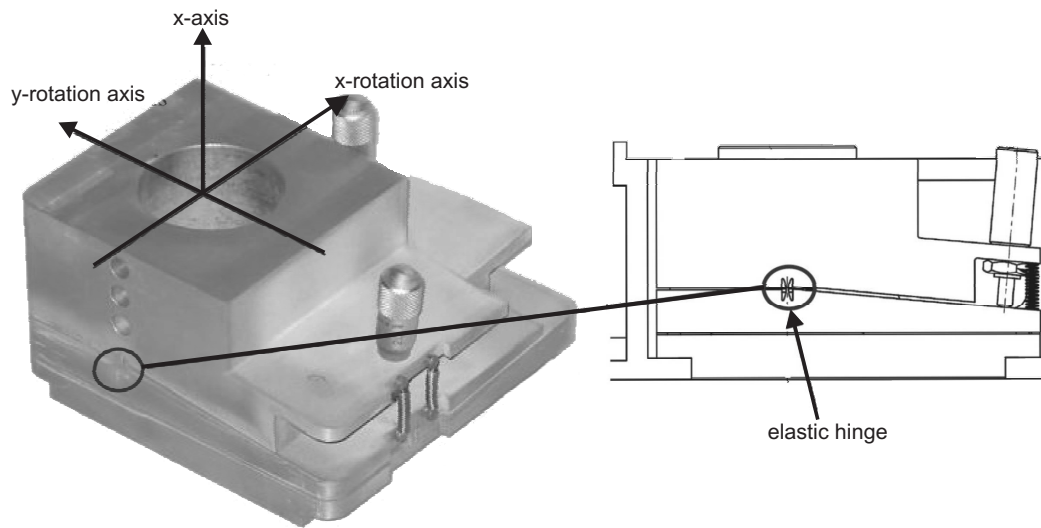


Figure 1.7: Sample-tilt stage based on elastic hinges developed at the TU/e [112].

The predictive capability of the EGP-model is validated for polycarbonate and poly(methyl methacrylate) by comparing experiments with numerical simulations, both performed at different indentation speeds and at different thermodynamic states of the material (Chapter 4).

Single-asperity scratch set-up

For the single-asperity scratch set-up there is also an issue concerning the choice of indenter tip geometry. The two tips selected in this study are cones with top angles of 90° , but with different top radii; one sharp tip with a top radius of $10 \mu\text{m}$, the other blunted with a radius of $50 \mu\text{m}$. The scratch set-up allows a maximum normal force of 500 mN. Considering Figure 1.4, all experiments conducted on polycarbonate are in the regime of ductile ploughing and elasto-plastic deformation, which is the region of interest when examining friction phenomena. The effect of sliding velocity applied on the measured friction force will be demonstrated. Similar to indentation, sample-tip misalignment during sliding will influence the measured friction force. Since the tip needs to be perpendicular to the sample surface, also for a quantitative comparison with numerical simulations, the sample-tilt stage is always employed. Results are presented in Chapter 5.

1.5 Scope of this thesis

In the first two chapters the EGP-model is presented with the multi-mode (Chapter 2), and multi-process (Chapter 3) extensions. In Chapter 4 the model is applied to indentation

experiments performed on two polymer glasses, i.e. polycarbonate and poly(methyl methacrylate); a quantitative prediction is obtained. Chapter 5 concerns the application of the model to a single-asperity scratch experiment, where a quantitative comparison between experiments and simulations is achieved by incorporation of a basic friction model. The thesis ends with some conclusions, recommendations and challenges for further research in Chapter 6.

Constitutive modelling of polymer glasses: a multi-mode approach¹

Abstract

This study aims to create a constitutive model which describes the complete intrinsic finite-strain, non-linear, visco-elastic response of glassy polymers which display thermorheologically simple behaviour. Starting point is the existing constitutive framework of the single-mode Eindhoven Glassy Polymer (EGP) model, which describes yield, and the post-yield response, accurately. To capture the details of the non-linear pre-yield regime, the EGP-model is extended to a multi-mode model, using a spectrum of relaxation times, which shift to shorter time scales under the influence of stress. A new method to extract such a spectrum out of a simple uniaxial extension, or compression, experiment is presented. It is shown that a reference spectrum can be defined which is independent of the strain rate applied and/or the polymer's thermodynamic state. The relaxation times of the reference spectrum simply shift by using a single state parameter capturing the current thermodynamic state of the material. We demonstrate that a quantitative prediction of the complete intrinsic stress-strain response is possible. The only adjustable parameter in the model is the state parameter, but as demonstrated in Engels et al. [46] and Govaert et al. [61] once the details of the formation history of the polymer product are known, this state can directly be computed.

¹partially reproduced from: L.C.A. van Breemen, E.T.J. Klompen, L.E. Govaert and H.E.H. Meijer, Constitutive modelling of polymer glasses: a multi-mode approach, *Journal of the Mechanics and Physics of Solids*, *submitted*

2.1 Introduction

Related to their excellent tribological properties, polymers are frequently used in load-bearing contact situations, like hip-joints, bearings and gears. However, the exact causes for these favourable properties are largely unknown and the relation between intrinsic polymer properties and friction and wear behaviour is blurred given that the measurements to probe them contain too many variables. To understand precisely which intrinsic polymer properties influence the mechanical response, the rise of FEM-based analyses opened up new possibilities. FEM is used to analyse contact phenomena like e.g. indentation [2, 55, 89, 146, 148] and single asperity sliding friction [30, 31, 50, 92]. In the case of polymers, the local deformation, and stress, fields are governed by the strain rate applied, the pressure dependence of the polymer's behaviour and its complex large strain mechanics. An appropriate finite-strain constitutive relation, capturing these intrinsic deformation characteristics, is therefore required. For polymer glasses several constitutive relations are available [21, 32, 35, 59, 85] and two typical time dependencies need to be considered [85]. The first being the rate-dependence, see Figure 2.1(a), the second, the dependence on thermal history, see Figure 2.1(b). To observe the polymer's intrinsic mechanical response, homogeneous deformation is applied to a sample; performing typically a uniaxial compression test. We differentiate between the (non)linear visco-elastic pre-yield regime, on one hand, and, on the other hand, the post-yield behaviour which is governed by strain softening, the decrease in true stress after passing the yield point, and strain hardening, the increase in stress at large deformations. Once the intrinsic response is known from homogeneous compression tests, the material response in inhomogeneous tensile tests can be computed [4, 86, 93, 158, 159].

A landmark in glassy polymer modelling was the work of Haward and Thackray [71], who proposed to model this type of behaviour by two contributions acting in parallel. The first corresponds to a visco-elastic contribution related to inter-molecular interactions that determine the low strain behaviour including yield and strain softening, and the second to a rubber-elastic contribution of the molecular network, accounting for the large strain, strain-hardening response. In this model no explicit use of a yield criterion is made. The deformation is rather determined by a single relaxation time that strongly depends on the equivalent stress. A sharp transition from solid to fluid-like behaviour results, similar to an elasto-plastic response employing a Von Mises yield criterion. The Haward and Thackray approach was extended to a full 3D description by Boyce et al. [21], in what is known as the (Boyce, Parks, Argon) BPA-model [4, 70, 157]. Equivalent approaches are the model developed by the group of Paul Buckley in Oxford [32, 33, 156] and the Eindhoven Glassy Polymer model developed in our group [6, 59, 85, 137, 139, 149]. The basis of this 3D constitutive model was proposed by Tervoort et al. [139] and extended by Govaert et al. [59] [137, 149] to include pressure dependence, strain softening and strain hardening. The latest improvements were incorporated by Klompen et al. [85] who refined the description of the post-yield regime by

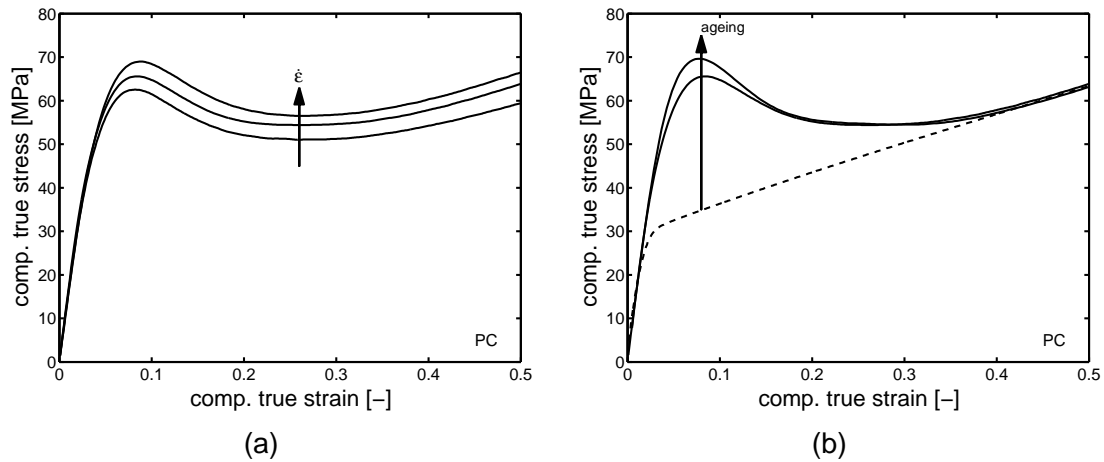


Figure 2.1: Intrinsic stress-strain response of polycarbonate: (a) dependence on strain rate; (b) dependence on thermal history, where the dashed line (- -) is the reference state.

redefining the softening function and by introducing a new reference state, the 'un-aged' state, see the dashed line in Figure 2.1(b). This model, further referred to as the EGP-model, proves accurate in describing yield and post-yield behaviour of glassy polymers. Likewise, it is able to capture experimentally observed phenomena such as necking, crazing and shear banding as well as long-term failure under static load [59, 86, 149].

The model has recently also been applied to quantitatively predict the loading part of an indentation experiment, using a spherical [148] and flat-tip indenter over a wide range of indentation speeds and thermodynamic states [146]. Provided that the modulus, required to describe the correct yield strain and the subsequent post-yield behaviour, has been changed in magnitude, a correct prediction of the indentation response proves possible. An extension of the BPA-model, as proposed by Anand and Ames, was demonstrated to adequately describe a conical-tip indentation experiment on PMMA [2], albeit at a single indentation speed. These studies also show that both, the EGP- and the BPA-model, are incapable of capturing the unloading response. This shortcoming hampers application to, for instance, sliding friction simulations; here continuous unloading during sliding behind the tip occurs, thus a quantitative prediction of the experimental force response is impaired. Since the single-relaxation time approximation cannot account for the multi-relaxation times response observed in polymers, with relaxation times covering tens of decades, a multi-mode extension of the model is required to obtain quantitative predictions. Another motivation for this is that the use of a single relaxation time results in an abrupt transition from elastic to (visco)plastic behaviour, which is rarely seen in practice.

Therefore we introduce a multi-relaxation-times model which captures the non-linearity of the pre-yield regime. The model proposed is a combination of the pre-yield approach from Tervoort et al. [138] and the post-yield response from Klompen et al. [85] and is based on

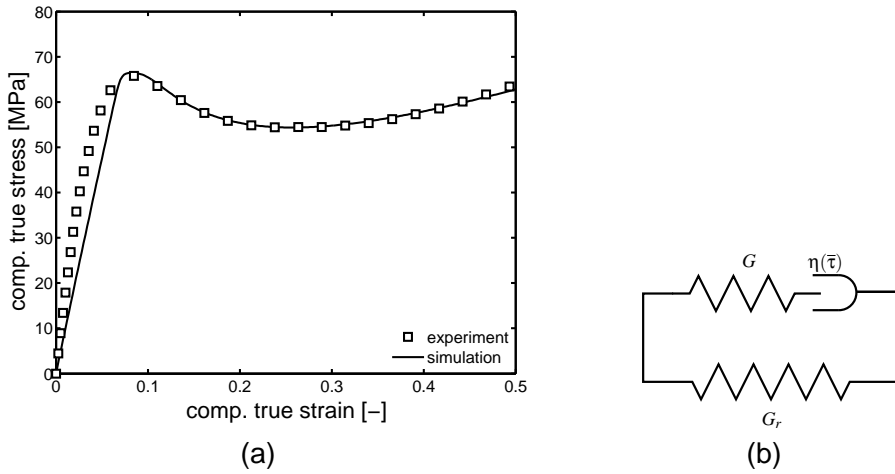


Figure 2.2: (a) Intrinsic stress-strain response of polycarbonate at a strain rate of 10^{-3} s^{-1} ; (b) mechanical analogue for the single-mode EGP-model.

a multi-mode Maxwell model, including time-stress superposition, adequately describing the deformation under monotonic loading. A new characterization method is designed that directly yields a relaxation time spectrum from constant rate compression, or tension, experiments. The spectrum thus obtained not only accurately describes loading curves at different strain rates, but also constant rate loading-unloading contact problems, see Chapter 4. The influence of the thermal history is, as usual, included in an age-dependent state parameter, leading to the definition of a reference state; the un-aged state [85].

2.2 Modelling

Numerical modelling

The single-mode 3D elasto-visco-plastic constitutive model used as basis, accurately captures the post-yield intrinsic deformation characteristics of polymer glasses [59, 85, 86, 138, 139], see Figure 2.2. In the model the total stress is split into the driving stress and the hardening stress [71]:

$$\boldsymbol{\sigma} = \boldsymbol{\sigma}_s + \boldsymbol{\sigma}_r. \quad (2.1)$$

Here $\boldsymbol{\sigma}_r$ represents the hardening stress, which is physically interpreted as a rubber elastic contribution of the orienting entangled network and is mathematically described with a neo-Hookean relation [59, 137]

$$\boldsymbol{\sigma}_r = G_r \tilde{\mathbf{B}}^d, \quad (2.2)$$

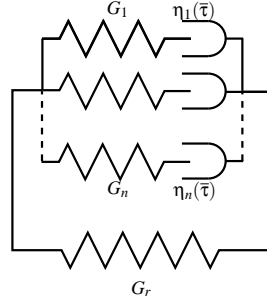


Figure 2.3: Mechanical analog for the multi-mode EGP-model.

where G_r is the strain hardening modulus and $\tilde{\mathbf{B}}^d$ is the deviatoric part of the isochoric left Cauchy-Green strain tensor. The driving stress σ_s is attributed to intermolecular interactions [85, 138] and is split into a hydrostatic and a deviatoric part [6, 139].

The essential difference with the constitutive model presented in Klompen et al. [85] is that the deviatoric part is now modelled as a combination of n parallel linked Maxwell elements [138], see Figure 2.3:

$$\sigma_s = \sigma_s^h + \sum_{i=1}^n \sigma_{s,i}^d = \kappa(J-1)\mathbf{I} + \sum_{i=1}^n G_i \tilde{\mathbf{B}}_{e,i}^d. \quad (2.3)$$

Here κ is the bulk modulus, J the volume change ratio, \mathbf{I} the unity tensor, G the shear modulus and $\tilde{\mathbf{B}}_e$ the elastic part of the isochoric left Cauchy-Green strain tensor. The subscript i refers to a specific mode, $i = [1, 2, 3, \dots, n]$. Because of the time- and history-dependence of the model, the elastic and volumetric strains must be updated by integration of the evolution equations for $\tilde{\mathbf{B}}_{e,i}$ and J :

$$\dot{J} = J \text{tr}(\mathbf{D}) \quad (2.4)$$

$$\dot{\tilde{\mathbf{B}}}_{e,i} = (\tilde{\mathbf{L}} - \mathbf{D}_{p,i}) \cdot \tilde{\mathbf{B}}_{e,i} + \tilde{\mathbf{B}}_{e,i} (\tilde{\mathbf{L}}^c - \mathbf{D}_{p,i}). \quad (2.5)$$

The plastic deformation rate tensors $\mathbf{D}_{p,i}$ are related to the deviatoric stresses $\sigma_{s,i}^d$ by a non-Newtonian flow rule with modified Eyring equations η_i [45, 49, 120]:

$$\mathbf{D}_{p,i} = \frac{\sigma_{s,i}^d}{2\eta_i(\bar{\tau}, p, S_a)}, \quad (2.6)$$

where $\bar{\tau}$, the total equivalent stress, and p , the hydrostatic pressure, depend on the total stress and not on the modal stress, according to

$$\bar{\tau} = \sqrt{\frac{1}{2} \sigma_s^d : \sigma_s^d} \quad ; \quad p = -\frac{1}{3} \text{tr}(\sigma). \quad (2.7)$$

The viscosities are described by an Eyring flow rule, which has been extended [44, 45, 59, 119] to take pressure dependence and intrinsic strain softening into account:

$$\eta_i = \eta_{0,i,ref} \underbrace{\frac{\bar{\tau}/\tau_0}{\sinh(\bar{\tau}/\tau_0)}}_I \underbrace{\exp\left[\frac{\mu p}{\tau_0}\right]}_{II} \underbrace{\exp[S]}_{III}. \quad (2.8)$$

The zero-viscosities, $\eta_{0,i,ref}$, are defined according to the so-called reference (un-aged) state [85]. Part *I* in Equation (2.8) captures the deformation kinetics and can be regarded as a stress-dependent shift factor. For low values of the equivalent stress, $\bar{\tau} < \tau_0$, this part equals unity and, with increasing stress, it decreases exponentially. Part *II* expresses the pressure dependency governed by the parameter μ , while part *III* captures the dependency of the viscosity on the thermodynamic history, expressed in the state parameter S . The formulation chosen implies that the dependence on stress, pressure and thermodynamic state is identical for all relaxation times and that hence time-stress, time-pressure and time-thermodynamic state superposition is assumed to apply. S is related to the equivalent plastic strain ($\bar{\gamma}_p$) according to:

$$S(\bar{\gamma}_p) = S_a \cdot R(\bar{\gamma}_p) \quad \text{where} \quad S \in [0, S_a]. \quad (2.9)$$

The initial thermodynamic state of the material is uniquely defined by the state parameter S_a . If the material is in its reference state, S_a has a value of zero. With increasing age the value of S_a increases, causing an increase in yield stress. For the short term loading conditions, as considered in this study, physical ageing, which is captured by the evolution of $S_a(t)$ [85, 86], is not required; the focus will be on materials with a difference in initial age, as obtained by differences in thermal history, i.e. we take S_a as a constant with different values. The equivalent plastic strain rate ($\dot{\bar{\gamma}}_p$) is coupled to the mode with the highest zero-viscosity, since this mode determines the development of plastic strain. This mode shall be referred to as mode 1, i.e. $i = 1$. The equivalent plastic strain rate is defined as:

$$\dot{\bar{\gamma}}_p = \frac{\bar{\tau}_1}{\eta_1} \quad \text{where} \quad \bar{\tau}_1 = \sqrt{\frac{1}{2} \boldsymbol{\sigma}_{s,1}^d : \boldsymbol{\sigma}_{s,1}^d}. \quad (2.10)$$

The softening function $R(\bar{\gamma}_p)$ describes the strain softening process, i.e. the erasure of thermal history with the onset of plastic deformation. Klompen et al. [85] expressed $R(\bar{\gamma}_p)$ as a function of the equivalent plastic strain ($\bar{\gamma}_p$), by using a modified Carreau-Yasuda relation:

$$R(\bar{\gamma}_p) = \frac{(1 + (r_0 \cdot \exp(\bar{\gamma}_p))^{r_1})^{\frac{r_2-1}{r_1}}}{(1 + r_0^{r_1})^{\frac{r_2-1}{r_1}}} \quad \text{where} \quad R(\bar{\gamma}_p) \in \langle 0, 1 \rangle, \quad (2.11)$$

and r_0 , r_1 and r_2 are fitting parameters. To summarize: the yield stress increases from its reference state with increase of S_a and the momentary stress decreases on the onset of plastic

deformation finally back to its reference state.

Spectrum determination

For small strains the multi-mode EGP-model reduces to a generalized Maxwell model [84, 138] and to obtain the linear EGP-parameters, the linear relaxation-time spectrum needs to be determined. Several methods are available to obtain the linear relaxation function over a sufficiently large time interval. The best documented methods use equivalent time approaches, like time-temperature [51, 109, 127, 141], time-stress [126, 142] or time-strain superposition [109, 143]. We will use the time-stress approach.

Time-stress superposition

Time-stress superposition implies that the non-linearity of the total stress alters the intrinsic time-scale and is sometimes also referred to as a 'stress-clock' [17]. This peculiar non-linearity of stress is frequently used to describe the non-linear visco-elastic behaviour by means of incorporation of a stress reduced time [91] in the Boltzmann integral [126]. For the single-mode model, the viscosity of the dash-pot depends on the current total stress, applied on the mode, through the stress dependent shift function ($a_\sigma(\sigma)$):

$$\begin{aligned} \eta(\sigma) &= \eta_0 a_\sigma(\sigma) \quad \text{where} \\ a_\sigma(\sigma) &= \frac{\sigma/\sigma_0}{\sinh(\sigma/\sigma_0)} \quad \text{with} \quad \sigma_0 = \frac{3}{\sqrt{3}-\mu} \tau_0. \end{aligned} \quad (2.12)$$

The shift-function is set equal to unity for $\sigma < \sigma_0$, leading to a linear response. For values of $\sigma > \sigma_0$, the viscosity decreases exponentially as a function of the applied stress, leading to a stress dependent relaxation time, $\lambda(\sigma)$:

$$\lambda(\sigma) = \lambda_0 a_\sigma(\sigma), \quad (2.13)$$

where λ_0 is the initial characteristic time and σ the stress applied on the mode. The constitutive behaviour of a 1D equivalent of our single-mode non-linear Maxwell element can be expressed in a Boltzmann single integral in its relaxation form [51]:

$$\begin{aligned} \sigma(t) &= \int_{-\infty}^t E(\psi - \psi') \dot{\epsilon}(t') dt' \quad \text{with} \\ \psi &= \int_{-\infty}^t \frac{dt''}{a_\sigma[\sigma(t'')] } \quad \text{and} \quad \psi' = \int_{-\infty}^{t'} \frac{dt''}{a_\sigma[\sigma(t'')]}. \end{aligned} \quad (2.14)$$

Where $\sigma(t)$ is the stress at time t , E is the relaxation modulus and $\dot{\epsilon}$ is the strain rate. The stress reduced time ψ , and the pending stress reduced time ψ' , can be calculated by

integration of the shift factor $a_\sigma(\sigma)$ [83, 126, 138]. This implies that the relaxation time of the Maxwell mode becomes shorter when a higher stress is applied. The multi-mode approach uses an arbitrary number (n) of these parallel linked modes to get a more detailed description of the pre-yield mechanical response. The characteristic visco-elastic function $E(t)$ is expressed as :

$$E(t) = \sum_{i=1}^n E_i \exp\left(-\frac{t}{\lambda_i}\right). \quad (2.15)$$

Equations (2.14) and (2.15) implicitly state that all modes involved are influenced by stress in the same manner.

Relaxation spectrum

In the case of time-stress superposition, the standard approach to determine the linear relaxation spectrum is by constructing a compliance-time master curve from constant stress, i.e. creep, experiments; prime examples of this procedure can be found in Tervoort et al. [138]. The discrete linear relaxation spectrum was derived from a compliance-time master curve by fitting a discrete spectrum of Kelvin-Voigt modes, employing a non-negative least-squares method [90] to obtain physically realistic values. An accurate prediction of constant strain rate experiments at different strain rates, and also of stress relaxation experiments at different strains, was achieved. It should be noted, however, that the number of experiments, and calculation steps, necessary to obtain a suitable spectrum in this manner, are considerable.

In contrast, the method proposed here requires only one set of uniaxial tests, compression or tensile, up to the point of yield at different constant strain rates and, thus, significantly reduces the number of experiments needed. Klompen et al. [85] showed that the non-linearity parameter, σ_0 , can be obtained by plotting the yield stress versus the logarithm of the strain rate where, for a thermorheologically simple material, the slope of this line identifies the non-linearity parameter σ_0 . When the non-linearity is known, the pre-yield regime of one of the tests is used to determine the spectrum of Maxwell modes. To achieve this, the experimental data are corrected by subtracting the hardening stress from the total stress, leaving the driving stress.

For uniaxial compression this yields [85]:

$$\sigma_s(t) = \sigma(t) - \frac{\sqrt{3}}{\sqrt{3} - \mu} G_r \left(\lambda^2 - \frac{1}{\lambda} \right). \quad (2.16)$$

While for uniaxial extension we find:

$$\sigma_s(t) = \sigma(t) - \frac{\sqrt{3}}{\sqrt{3} + \mu} G_r \left(\lambda^2 - \frac{1}{\lambda} \right). \quad (2.17)$$

For a constant strain rate experiment, substitution of Equation (2.15) into Equation (2.14) leads to:

$$\sigma_s(t) = \sum_{i=1}^n \left[E_i \dot{\epsilon} \int_{\infty}^t \exp\left(-\frac{\Psi - \Psi'}{\lambda_i}\right) dt' \right]. \quad (2.18)$$

If the stress non-linearity is known, (a_σ), see Equation (2.12), and by choosing a discrete spectrum of relaxation times, λ_i , thus modes, the integral is evaluated at every experimental time point for each separate relaxation time. The moduli E_i of the modes are unknown and are subsequently determined by fitting the experimental data with Equation (2.18). By dividing the experimental time span t in m equidistant time steps (Δt), the integral of Equation (2.18) is discretised such that:

$$\begin{aligned} \sigma(j\Delta t) &= M_1 \Delta \epsilon E_1 + \dots + M_i \Delta \epsilon E_i \quad \text{with} \\ M_i &= 1 + \exp\left(-\frac{\Psi(2\Delta t) - \Psi(\Delta t)}{\lambda_i}\right) + \dots + \exp\left(-\frac{\Psi(j\Delta t)}{\lambda_i}\right). \end{aligned} \quad (2.19)$$

For $j = 1, 2, \dots, m$ we can introduce a matrix-column notation:

$$\underline{\sigma} = \underline{M} \underline{E}. \quad (2.20)$$

Here $\underline{\sigma}$ contains the stress as a function of time (corrected by using Equation (2.16) or Equation (2.17)), \underline{E} the corresponding moduli and \underline{M} is a diagonal matrix with the summed terms that increase in time. When all moduli are known, the corresponding spectrum of shear moduli, G_i , and zero-shear viscosities, $\eta_{0,i}$, is calculated. This involves the conversion of the relaxation modulus $E(t)$ into the shear relaxation modulus $G(t)$, using the correspondence principle, which states that the appropriate Laplace transform of an elastic response to a stress analysis problem is interchangeable with the Laplace transform of the visco-elastic response. If the volumetric response is chosen to be fully elastic, thus treating the bulk modulus κ as a constant, the elastic conversion formula can be expressed as:

$$G = \frac{3\kappa E}{9\kappa - E} \quad \rightarrow \quad s\bar{G}(s) = \frac{3\kappa_0 s \bar{E}(s)}{9\kappa_0 - s \bar{E}(s)} \quad \text{with} \quad \kappa_0 = \kappa s. \quad (2.21)$$

According to the correspondence principle, the Laplace transforms $\bar{E}(s)$ and $\bar{G}(s)$ are replaced with the Laplace transforms of the corresponding visco-elastic response functions:

$$\bar{E}(s) = \sum_{i=1}^n E_i \frac{\lambda_i}{1 + \lambda_i s} \quad \text{and} \quad \bar{G}(s) = \sum_{i=1}^n G_i \frac{\lambda_i}{1 + \lambda_i s}. \quad (2.22)$$

By combining Equations (2.21) and (2.22), and substitution of the relaxation times λ_i , as obtained from Equation (2.15), a system of equations is obtained which can be solved by

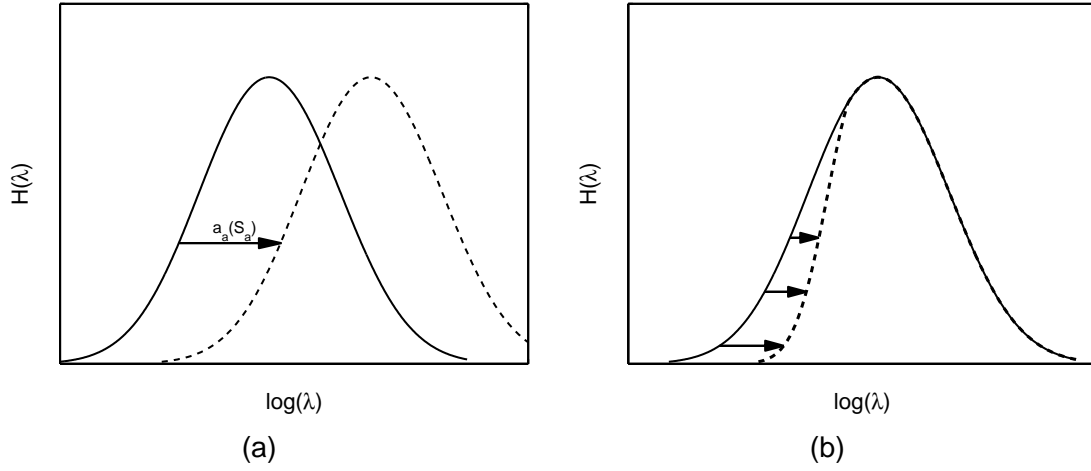


Figure 2.4: (a) Time-ageing time influence on relaxation-time spectrum; (b) influence of sequential ageing on relaxation time spectrum.

means of a non-negative least squares method [90]:

$$\underline{b} = \underline{A}\underline{G} \quad \text{where} \quad \underline{b} = \frac{3\kappa_0 \sum_{i=1}^n E_i \frac{\lambda_i}{1 + \lambda_i \underline{\zeta}}}{9\kappa_0 - \underline{\zeta} \sum_{i=1}^n E_i \frac{\lambda_i}{1 + \lambda_i \underline{\zeta}}} \quad \text{and} \quad \underline{A} = \frac{\lambda_i \underline{\zeta}}{1 + \lambda_i \underline{\zeta}}. \quad (2.23)$$

With the shear moduli stored in \underline{G} , the corresponding zero-shear viscosities are calculated, $\eta_{0,i} = \lambda_i \cdot G_i$. To derive the viscosities, $\eta_{0,i,ref}$, as put forward in Equation (2.8), defined with respect to the reference state, the calculated viscosities have to be corrected for the current thermodynamic state of the material, by equally shifting all viscosities along the time axis to the reference state (un-aged), using the time-ageing time superposition principle, according to:

$$\eta_{0,i,ref} = \eta_{0,i} \cdot a_a(-S_a) \quad \text{where} \quad a_a(S_a) = \exp(S_a). \quad (2.24)$$

This implies that all relaxation times are equally affected by the thermal history. Constructing a master curve, by horizontal shifting only, is in full agreement with the classical approach proposed by Struik [130], which has been proven to apply to many polymer systems [36, 109]. This rationale of time-ageing time superposition is graphically depicted in Figure 2.4(a). It should be noted that there are some experimental observations that suggest a more complex ageing process. A prime example is the observation of Bauwens [9] where PC samples, which were placed on a shelf to age for 3 years at room temperature, displayed a significant increase of the Young's modulus, whereas the yield stress remained unaffected. In our model this could only be explained by a sequential ageing approach. The principle of sequential ageing, as proposed by McCrum [99], states that relaxation times are only influenced if they are equal or less in magnitude than the ageing time itself. The consequence is an asymmetric shift in

the relaxation time spectrum, as is shown in Figure 2.4(b). However, for our applications time-ageing time superposition holds because the experimental time does not surpass the ageing time and thus is applied accordingly.

2.3 Experimental

Materials and sample preparation

The material used in this study is polycarbonate (PC). Uniaxial tensile and compression samples are prepared from Lexan 101R, provided by Sabic Innovative Plastics, while samples for loading geometry comparison are cut from an extruded 3 mm sheet (Makrolon, Bayer).

For uniaxial compression tests, cylindrical samples ($\varnothing 6 \text{ mm} \times 6 \text{ mm}$) are machined from compression moulded plates ($200 \times 200 \times 10 \text{ mm}^3$). First the dried granulate is heated in a mould for 15 minutes at $250 \text{ }^\circ\text{C}$ and next compressed up to 300 kN in five subsequent intervals of 5 minutes, while after each step the force is released to allow for degassing. Finally the mould is placed in a cold press and cooled to room temperature ($20 \text{ }^\circ\text{C}$) under a moderate force of 100 kN.

Tensile bars are injection-moulded on an Arburg Allrounder 320S 150/200, using an Axxicon mould (according to ASTM 638D type III). To change the thermodynamic state of the material, two batches are subjected to annealing treatments of 144 hours at $120 \text{ }^\circ\text{C}$ and 144 hours at $100 \text{ }^\circ\text{C}$, respectively. Subsequently, the samples are air cooled to room temperature ($20 \text{ }^\circ\text{C}$).

To enable direct comparison between different loading geometries and a standard tensile test, tensile bars (according to ASTM 638D type III) with a thickness of 1.7 mm, this to minimize any influence of a processing-induced yield stress distribution over the thickness [61], are milled from the extruded sheet. To change the thermodynamic state of the tensile bars, they are annealed at $120 \text{ }^\circ\text{C}$ for 48 hours. To complete the set of samples, two different loading geometries are added, respectively, planar extension and simple shear. For planar extension, rectangular samples with a dog-bone shaped cross-section are milled from the sheet [60]. The testing region has a thickness of 1.7 mm over a length of 10 mm and a width of 50 mm. Due to the large width-to-length ratio, the contraction of the material is constrained, creating a plane strain condition. The simple shear samples are similar to the planar extension samples, but with a width of 100 mm, this to create an aspect ratio of 10.

Techniques

Uniaxial tension and compression tests are performed on a servo-hydraulic MTS Elastomers Testing System 810, equipped with a thermostatically controlled environmental chamber. The tensile bars are loaded under true strain control, at constant true strain rates of 10^{-4} to 10^{-2} s^{-1} at 20 °C. True strain control is achieved by a clip-on Instron extensometer, with a gauge length of 25 mm, attached to the tensile bar, using calculated input to transform the linear strain to true strain. True stresses are calculated assuming incompressibility. The cylindrically shaped samples are compressed between two parallel flat steel plates at strain rates of 10^{-4} to 10^{-2} s^{-1} at 20 °C. To prevent bulging of the sample due to friction, a thin PTFE film (3M 5480, PTFE skived film tape) is applied at the ends of the sample and the contact area between the plates and tape is lubricated using a 1:1 mixture of detergent and water.

The uniaxial and planar tensile tests, using samples milled from the extruded sheet, are performed on a Zwick Z010 tensile tester, at constant linear strain rates of 10^{-5} to 10^{-1} s^{-1} . The corresponding shear tests are performed on a Zwick 1475 at rates of 10^{-5} to 10^{-2} s^{-1} .

Numerical simulations

All simulations are performed using the finite element package MSC.Marc. The constitutive model is implemented in this package by means of the user subroutine HYPELA2. The uniaxial compression tests are simulated using a single linear quad4 axi-symmetric element. The uniaxial, planar and simple shear samples used in the experiments are meshed in full 3D and consist of 2130, 3760 and 7520 linear brick elements, respectively.

2.4 Results and discussion

Material characterization

The spectrum determination procedure requires a set of input-parameters, more specifically the strain hardening modulus G_r , the elastic bulk modulus κ , the pressure dependence parameter μ and the non-linearity parameter σ_0 . For PC the determination of these parameters, as obtained from uniaxial compression tests, is described in detail in Klompen et al. [85] and the results are tabulated in Table 2.1. In Section 2.2 the procedure of spectrum determination is discussed elaborately, however, the values obtained for a specific spectrum are not completely trivial. Some aspects need closer examination: first its sensitivity to the number of modes and second, since a spectrum is obtained at a specific strain rate and a specific initial age, its dependence on these two parameters.

Table 2.1: Input parameters.

parameter	value	dimension
G_r	26	[MPa]
κ	3750	[MPa]
τ_0	0.7	[MPa]
S_a	—	[—]
μ	0.08	[—]
r_0	0.965	[—]
r_1	50	[—]
r_2	−3	[—]

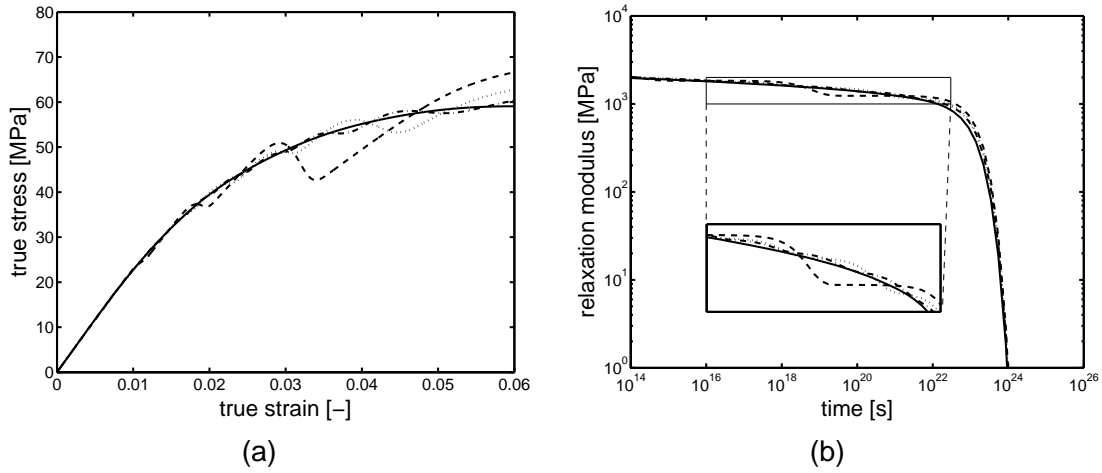


Figure 2.5: Sensitivity to number of modes for: (a) Intrinsic stress-strain response and (b) relaxation modulus versus time; the dashed lines (- -) corresponds to 4 modes, the dotted lines ($\cdot\cdot\cdot$) to 8 modes, the dash-dot lines (- \cdot -) to 12 modes and the solid lines (-) to 17 modes.

Computational times of finite element calculations are strongly influenced by the number of modes used, thus from a numerical point of view one would like to minimize the modes required. The number of modes is directly influenced by the user, as he, or she, decides which discrete relaxation times λ_i are available, whereupon the non-negative least square method decides which of the relaxation times provided are indeed needed to calculate the corresponding moduli E_i . When the routine [144] is limited in the number of relaxation times, this will result in a non smooth relaxation-time curve, and oscillations are observed. The transitions manifest themselves as abrupt bends in the simulated pre-yield regime and will display an apparent softening behaviour, see Figure 2.5. A proper description of the pre-yield regime is obtained by supplying two relaxation times per decade. The lower and upper bound are defined according to:

$$\log(\lambda_{min}) = \log(\psi(t = 0)) - 1 \quad \text{and} \quad \log(\lambda_{max}) = \log(\max(\psi)) + 1, \quad (2.25)$$

where λ_{min} is the minimum, and λ_{max} the maximum relaxation time. Using this predefined relaxation time spectrum, the least squares method eliminates all the relaxation times with a relaxation strength smaller than zero. Whereupon the user decides whether the spectrum obtained is smooth; 17 relaxation times proved to accurately capture the pre-yield regime. To obtain the viscosities as put forward in Equation (2.24), all the fitted relaxation times need to be shifted back to the reference state, which results in the reference spectrum as stated in Table 2.2. To complete the set of model parameters, the three parameters describing the

Table 2.2: Reference spectrum for Polycarbonate Lexan 101R.

mode	$\eta_{0,i,ref} [MPa \cdot s]$	$G_i [MPa]$	$\lambda_i [s]$
1	$2.10 \cdot 10^{11}$	$3.52 \cdot 10^2$	$5.97 \cdot 10^8$
2	$3.48 \cdot 10^9$	$5.55 \cdot 10^1$	$6.27 \cdot 10^7$
3	$2.95 \cdot 10^8$	$4.48 \cdot 10^1$	$6.58 \cdot 10^6$
4	$2.84 \cdot 10^7$	$4.12 \cdot 10^1$	$6.89 \cdot 10^5$
5	$2.54 \cdot 10^6$	$3.50 \cdot 10^1$	$7.26 \cdot 10^4$
6	$2.44 \cdot 10^5$	$3.20 \cdot 10^1$	$7.63 \cdot 10^3$
7	$2.20 \cdot 10^4$	$2.75 \cdot 10^1$	$8.00 \cdot 10^2$
8	$2.04 \cdot 10^3$	$2.43 \cdot 10^1$	$8.40 \cdot 10^1$
9	$1.83 \cdot 10^2$	$2.07 \cdot 10^1$	$8.84 \cdot 10^0$
10	$1.68 \cdot 10^1$	$1.81 \cdot 10^1$	$8.28 \cdot 10^{-1}$
11	$1.51 \cdot 10^0$	$1.54 \cdot 10^1$	$9.81 \cdot 10^{-2}$
12	$1.40 \cdot 10^{-1}$	$1.36 \cdot 10^1$	$1.03 \cdot 10^{-2}$
13	$1.27 \cdot 10^{-2}$	$1.19 \cdot 10^1$	$1.07 \cdot 10^{-3}$
14	$1.10 \cdot 10^{-3}$	$9.80 \cdot 10^0$	$1.12 \cdot 10^{-4}$
15	$1.23 \cdot 10^{-4}$	$1.04 \cdot 10^1$	$1.18 \cdot 10^{-5}$
16	$2.62 \cdot 10^{-6}$	$2.11 \cdot 10^0$	$1.24 \cdot 10^{-6}$
17	$2.14 \cdot 10^{-6}$	$1.64 \cdot 10^1$	$1.30 \cdot 10^{-7}$

shape of the softening function, r_0 , r_1 and r_2 are adopted from Klompen et al. [85], see Table 2.1.

Spectrum validation

Glassy polymers show two typical time dependencies, the first is the strain-rate dependence, the second the dependence on the thermal history [59]. To justify the use of a unique reference spectrum, it should be independent on these two time dependencies. The uniaxial tensile experiment from which the spectrum is obtained, is carried out at a specific strain rate while the sample used has a specific thermal history.

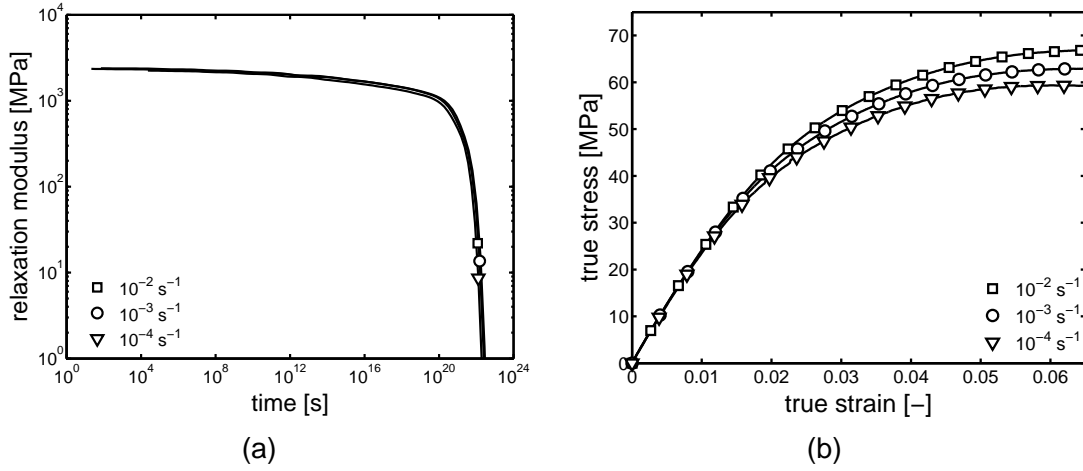


Figure 2.6: (a) Relaxation spectra obtained at three different strain rates (10^{-2} , 10^{-3} and 10^{-4} s^{-1}); (b) corresponding pre-yield regime of the tensile tests, where the markers are the experiments and the solid lines (–) the model prediction.

Strain-rate dependence

To test the dependence on strain rate, injection-moulded tensile bars are subjected to different constant strain rates varying from 10^{-2} to 10^{-4} s^{-1} . Since a strain gauge is used during the experiments, the true stress-true strain path can be constructed and a spectrum is fitted to each of the measurements. Figure 2.6(a) shows relaxation curves calculated with the spectra obtained. Although the spectra are fitted to different measurements they produce coinciding relaxation curves, which suggests that the spectra contain the same relaxation information. Thus a spectrum obtained at a specific strain rate can describe the pre-yield regime at another strain rate. To demonstrate this, the spectrum from Table 2.2 is used to predict the pre-yield regime of the tensile tests, see Figure 2.6(b). Here an excellent prediction of the stress-strain response is obtained over the entire range of strain rates.

Dependence on thermal history

To investigate the influence of ageing, the tensile bars are annealed at two different temperatures (100 °C and 120 °C) for 144 hours, prior to being tested at a strain rate of 10^{-3} s^{-1} whereupon spectra are extracted. The relaxation curves are compared with the data of the untreated tensile bars tested at the same strain rate. A clear difference is found between the three different, thermally-treated samples, see Figure 2.7. Since the difference in yield stress is solely the result of the difference in age, adopting the expression for the stress at yield from Klompen et al. [85], the value of the state parameter S_a , can be calculated:

$$\sigma_y(t) = \sigma_{ref}(\dot{\epsilon}) + \frac{3\tau_0}{\sqrt{3} + \mu} S_a(t) + \frac{\sqrt{3}}{\sqrt{3} + \mu} \sigma_r(\lambda_y). \quad (2.26)$$

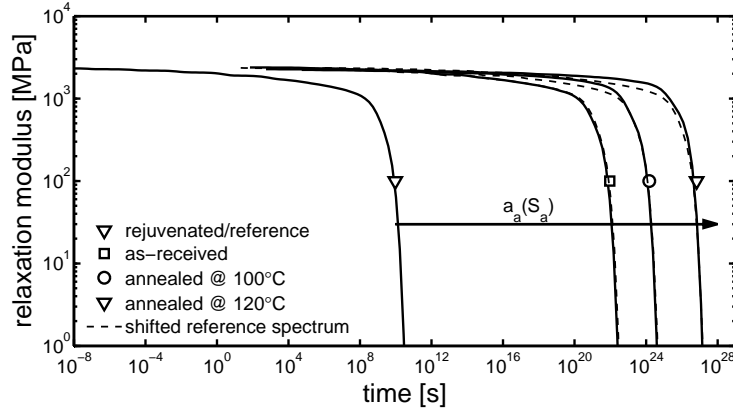


Figure 2.7: Relaxation spectra for different thermal histories which can be shifted from the reference state to their current thermodynamic state with $a_a(S_a)$.

Because the reference stress σ_{ref} , and the hardening stress σ_r are the same for all samples, this expression is reduced to:

$$\Delta\sigma_y = \sigma_y(t) - \sigma_{ref}(\dot{\epsilon}) = \frac{3\tau_0}{\sqrt{3} + \mu} S_a. \quad (2.27)$$

The difference in initial age, reflected in the value of S_a , is calculated from the difference between the yield stress in the reference state and the actual yield stress, $\Delta\sigma_y$. Once the spectra are shifted with $a_a(-S_a)$, as stated in Equation (2.24), the relaxation moduli coincide with the reference relaxation curve, see Figure 2.7. The corresponding stress-strain responses are calculated with the spectrum from Table 2.2 and the known $a_a(S_a)$, see Figure 2.8(a); the experimental data and simulations are in good agreement. To demonstrate that the new multi-mode EGP-model does not affect the large strain response [59, 85], two compression tests are simulated, performed at a constant strain rate of 10^{-3} s^{-1} , but with a difference in initial age. The reference spectrum, $S_a = 0.0$, is shifted with the values of S_a as adopted from Klompen et al. [85], respectively 27.0 and 29.6, see Figure 2.8(b). With the new EGP-model both the pre-yield as well as the post-yield regimes are modelled accurately.

Applications

Now we turn to applications of the new extended EGP-model. The strength of multi-mode modelling manifests itself particularly for all situations where non-homogeneous deformation determines the macroscopic mechanical response. Two situations where non-linear visco-elastic behaviour and inhomogeneous stress conditions greatly influence the macroscopic response are discussed, that is, inhomogeneous tensile tests and notched impact tests, where the latter are used to predict ductile-to-brittle transitions [47]. The application to contact phenomena, namely micro-indentation and single-asperity sliding friction, are dealt with in

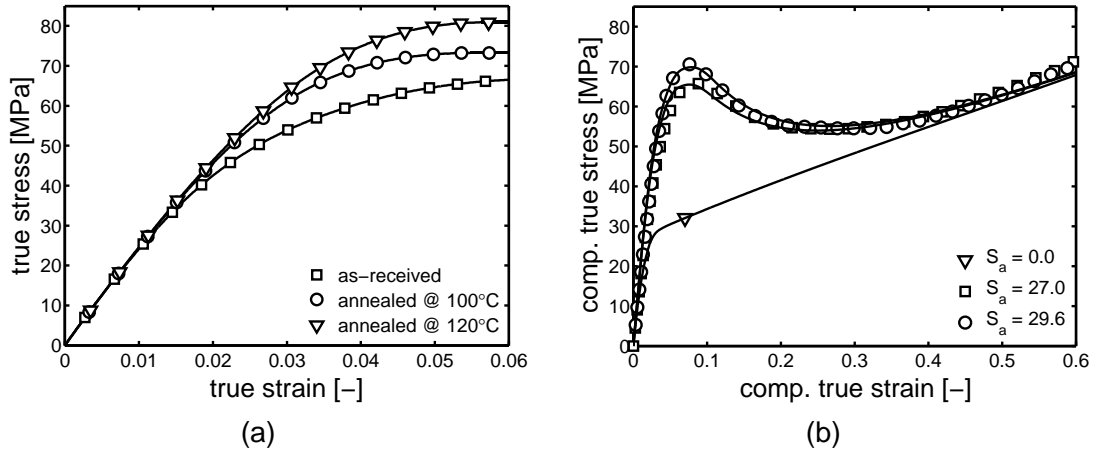


Figure 2.8: (a) Stress-strain response of polycarbonate tensile bars with different thermal histories obtained at strain rate of 10^{-3} s^{-1} ; (b) intrinsic stress-strain response of polycarbonate with different thermal histories at a strain rate of 10^{-3} s^{-1} [85]; the solid lines (–) are the model prediction using the same spectrum of relaxation times.

Chapters 4 and 5, respectively.

Stress relaxation

First the standard uniaxial tensile tests at various linear strain rates, as performed by Tervoort et al. [138], are used. Since the spectrum proves to be independent of strain rate applied and of initial age, the only unknown parameter in the model is the value of the state parameter S_a , which can be directly determined by matching the experimental yield stress at a single strain rate to the simulation. This results in an S_a of 33.7. Figure 2.9(a) shows an excellent agreement between experiments and simulations, achieved by simply shifting the reference spectrum to its current thermodynamic state. In addition, the non-linear stress relaxation experiments, also published in Tervoort et al. [138], are considered as well. Since the samples in both experiments are in equal thermodynamic state, the value of the state parameter S_a is identical. Since the stresses exceed the characteristic stress $\sigma_0 = 1.27 \text{ MPa}$, and are thus in the non-linear regime, it proves to be necessary to take the exact loading path into account, which is in accordance with the findings of Struik [130]. The results of the experimental data, and the corresponding simulations, are depicted in Figure 2.9(b), and are in good agreement.

Inhomogeneous tensile tests

Analogue to the procedure put forward above, the determination of the state parameter S_a only requires a fit procedure where the experimental yield stress has to correspond with the simulated yield stress. To demonstrate this, two simple tensile tests are performed at

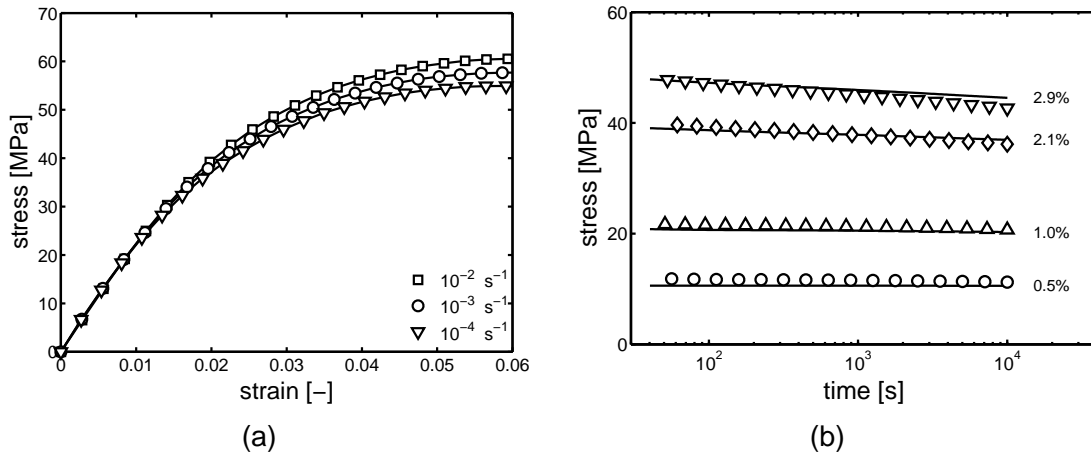


Figure 2.9: (a) Tensile tests at various linear strain rates (symbols) compared to model predictions (—); (b) stress relaxation at different linear strains (symbols) compared to model predictions (—).

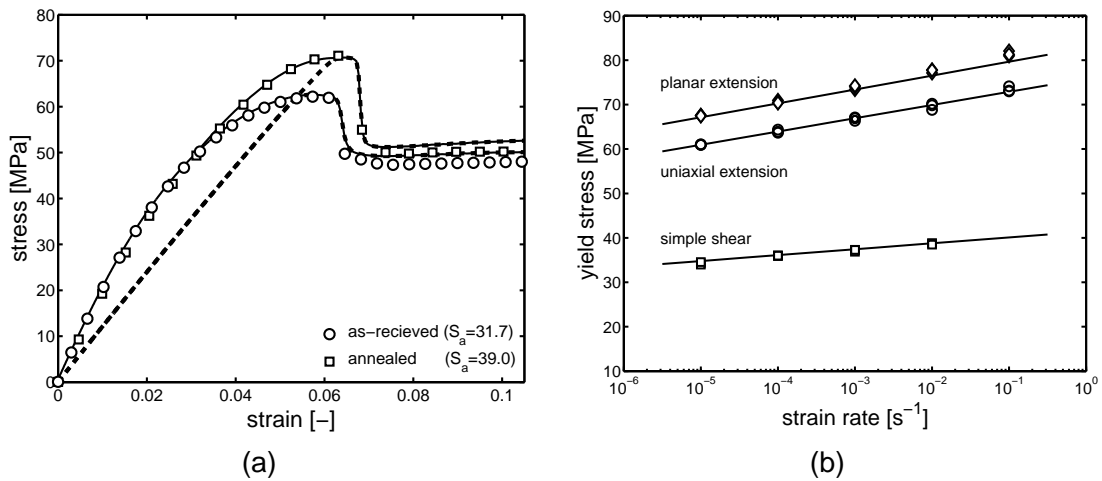


Figure 2.10: Experiments (open symbols) compared with the numerical simulation (multi-mode (—) and single-mode (---)) on PC: (a) tensile tests at a strain rate of 10^{-3} s^{-1} for two different thermal histories with for the as-received $S_a = 31.7$ (\circ) and for the annealed material $S_a = 39.0$ (\square); (b) predicted yield stress at different strain rates, $S_a = 31.7$, for planar extension (\diamond), uniaxial extension (\circ) and shear (\square).

a strain rate of 10^{-3} s^{-1} . One for the sample of the as-received sheet material and one for the annealed sheet material which, as a result of the thermal treatment, has a substantially higher yield stress [12, 58, 85]. The simulations as shown in Figure 2.10(a), yield an $S_a = 31.7$ for the as-received material and $S_a = 39.0$ for the annealed material, which is in accordance with van Breemen et al. [146]. The dashed lines show the result for the single-mode model, whereas the solid lines are the multi-mode predictions. With the multi-mode EGP-model, both the pre- and post-yield response are quantitatively calculated. To corroborate the strength of our model, the yield stress versus the strain rate applied for different loading geometries is calculated

Table 2.3: Maximum hydrostatic stress.

S_a	multi-mode		single-mode	
	$\sigma_{max}[MPa]$	$displ.[mm]$	$\sigma_{max}[MPa]$	$displ.[mm]$
50.0	116.2	2.1	94.2	4.0
30.0	82.3	1.7	72.3	3.1
10.0	54.7	1.4	51.3	2.5

for the as-received material, see Figure 2.10(b). The solid lines are the model predictions, using the parameter set presented in Tables 2.1 and 2.2 and the S_a -value of 31.7 which was determined in Figure 2.10(a). It is clear that also an accurate quantitative description of all these experiments is obtained.

Notched impact tests

Embrittlement in the presence of a notch is featured by the build-up of a strong positive hydrostatic pressure underneath the notch [52, 136]. When a critical hydrostatic pressure is exceeded, voiding occurs followed by crazing. Van Melick et al. [148] showed for polystyrene, applying the single-mode EGP-model, that the ductile-to-brittle transition can be predicted, using hydrostatic stress as a criterion. In recent work of Engels et al. [47], the new multi-mode EGP-model is employed to define such a criterion for polycarbonate. The rationale for using the multi-mode model instead of the much simpler single-mode description is that, for polystyrene, the single-mode model is adequate in describing the pre-yield region, because a close to linear relation of stress on strain is observed, whereas polycarbonate displays a highly non-linear dependence. To investigate if such a criterion can be defined for polycarbonate, tensile bars with a notch are used, this to localize the plastic deformation in the notched region, yielding positive hydrostatic stresses. In Figure 2.11(a) the difference between the single- and multi-mode model is depicted for the maximum hydrostatic stress at an S_a -value of 30, which corresponds to a yield stress of approximately 60 MPa, if measured at a strain rate of 10^{-3} s^{-1} . The drawn lines, dotted (\cdots) and dashed ($- -$), correspond to onset of plastic deformation of the single- and multi-mode simulations, respectively. In Figure 2.11(b) the plastic deformation (left) and the hydrostatic stress (right) for the multi-mode (top) and single-mode (bottom) models are shown; the displayed images correspond to the displacement at the dashed line ($- -$) in Figure 2.11(a). The single-mode approach displays a significantly lower maximum hydrostatic stress, even at the onset of plastic deformation. Likewise, the displacements at which the maximum hydrostatic stresses are reached, 1.7 mm and 3.1 mm, see Figure 2.11(a), differ substantially. The displacement where a critical maximum hydrostatic stress is reached correspond with the experimental observation on the onset of brittle failure, ± 1.7 mm displacement in this geometry, as presented in Engels et al. [47]. Calculated maxima by hydrostatic stress values underneath a notch also prove to be sensitive to the polymer's age as reflected in the S_a -value, see Table 2.3. Using the multi-mode model a molecular weight

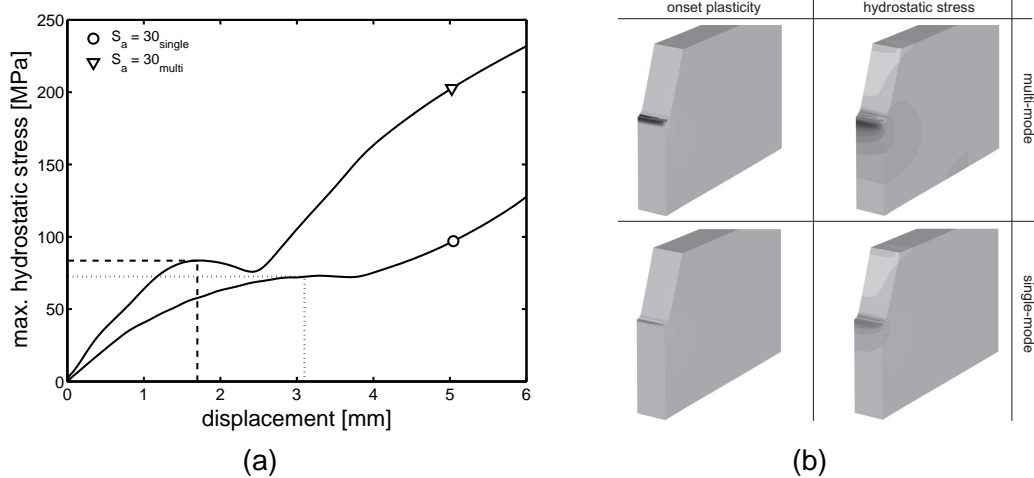


Figure 2.11: The effect of multi-mode modelling on notch impact; (a) the development of maximum hydrostatic pressure underneath the notch for multi-mode (∇) and single-mode (\circ), the dotted line (\cdots) and the dashed line ($- -$) correspond to the onset of plastic deformation for the single and the multi-mode simulation respectively. The images depicted in (b) correspond to the simulation data obtained at the dashed ($- -$) line (top left) development of plasticity for multi-mode (top right) development hydrostatic stress for multi-mode (bottom left) development of plasticity for single-mode (bottom right) development hydrostatic stress for single-mode.

dependent critical hydrostatic stress is found to be able to predict the initiation of ductile-to-brittle failure [47].

2.5 Conclusions

A phenomenological constitutive model is developed that identifies the different contributions of the various molecular interactions governing the complete intrinsic mechanical response of glassy polymers. The single-mode EGP-model [85], which only captures the intrinsic post-yield response accurately, has been extended into a multi-mode constitutive relation, based on the assumption that the pre-yield intrinsic mechanical response is determined by a spectrum of linear relaxation times, which shift to shorter time scales under the influence of stress. It was shown [138] that, for thermorheologically simple materials, the stress dependence is equivalent for all relaxation times. As a result, a straightforward method is developed to obtain a linear relaxation spectrum from a single uniaxial compression, or tensile, experiment performed at a single strain rate. The two typical time-dependencies of glassy polymers (their rate and thermal history dependence), are demonstrated not to influence the definition of the unique reference spectrum, which is characteristic for every grade. To obtain a quantitative description of the pre-yield regime, for polycarbonate seventeen Maxwell modes are required. The multi-mode model's quality manifests itself particularly in simulations where local non-

homogeneous deformations govern the macroscopic response, as demonstrated with notched impact tests to predict the ductile-to-brittle transition and will be demonstrated with the micro-indentation tests, see Chapter 4, and single-asperity sliding friction tests, see Chapter 5.

CHAPTER THREE

Constitutive modelling of polymer glasses: a multi-mode-multi-process approach¹

Abstract

Thermorheologically complex behaviour of glassy, and also of semi-crystalline, polymers is common rather than an exception. This study aims to develop a constitutive relation for the intrinsic deformation response of these complexly responding polymers and to establish a link with underlying molecular processes. Four glassy polymers are investigated: polycarbonate (PC), poly(methyl methacrylate) (PMMA), polystyrene (PS) and poly(L-lactic acid) (PLLA), that in uniaxial compression experiments all show a change in deformation kinetics from the yield to the post-yield region. A pronounced strain-rate dependence of the yield drop results. To cover these aspects the constitutive model for thermorheologically simple polymers is extended to include the combined contributions of more than one molecular process, resulting in a multi-mode-multi-process constitutive model. The influence of thermal history is accounted for by adjusting a single state parameter for each molecular process employed.

¹ reproduced from: L.C.A. van Breemen, T.A.P. Engels, L.E. Govaert and H.E.H. Meijer, Constitutive modelling of polymer glasses: a multi-mode-multi-process approach, *Journal of the Mechanics and Physics of Solids*, *submitted*

3.1 Introduction

Over the last decades considerable effort has been directed towards the development of constitutive models describing the large strain behaviour of solid polymeric systems [1, 4, 21, 32, 33, 35, 59, 69, 85, 139, 147, 157]. Application mainly focused on simulations of experimental observations such as necking, crazing and shear banding [59, 93, 101, 148, 158, 159]. Simulation unambiguously demonstrated that initiation of all these different phenomena is related to an accumulation of plastic deformation that triggers intrinsic strain softening, which ultimately results in strain localization and the onset of failure. An accurate description of the rate dependence proved to be crucial in time-to-failure predictions under static load [86].

In all these studies, the strain-rate dependence of the polymer's mechanical response was dominated by a single molecular process. As a result the mechanical response is thermorheologically simple, implying that time-stress and (Arrhenius-like) time-temperature superposition can be applied. Likewise, the yield stress is captured by a single Eyring flow process [49]. Unfortunately however, thermorheologically simple behaviour is an exception rather than a rule for all polymers, be it that it manifests itself sometimes only at high deformation rates or low testing temperatures.

Generally, a dynamic analysis of a solid thermoplastic displays, apart from the primary relaxation mechanism (α , T_g for glassy polymers), at least one secondary transition (β) [72, 102]. When tested over a broad range of temperatures and strain rates, most polymers therefore show a change in slope in yield stress versus the logarithm of strain rate applied, as for glassy polymers was experimentally observed already more than three decades ago by Roetling [121–123] and Bauwens and co-workers [10, 11, 13, 15]. The Ree-Eyring modification [120] of Eyring's flow theory [49] proved well able to describe this particular behaviour. The method is based on the assumption that two molecular processes (α and β), each represented by an Eyring flow-process, act in parallel, implying that their individual contributions to the stress are additive. Similar observations were made for semi-crystalline polymers [62, 94, 123, 153], and the utilization of the Ree-Eyring modified Eyring flow theory proved to be successful in capturing the yield data of this class of polymers as well.

All studies focused on yield kinetics, and the post-yield response (strain softening and strain hardening) was basically ignored. Only in the constitutive modelling of Klompen and Govaert [83], an emphasis is found on correctly capturing the pre-yield, yield as well as the creep response. They showed that incorporation of two processes acting in parallel in the multi-mode pre-yield model, as proposed by Tervoort et al. [138], is possible. More recently, Mulliken and Boyce [105] used an identical framework to capture the yield kinetics, focusing on high strain rate predictions.

The EGP-model, derived for thermorheologically simple polymer glasses [59, 85, 139, 147],

accurately captures the non-linear pre-yield regime as well as the post-yield response, i.e. strain softening and strain hardening. For uniaxial conditions a second parallel Maxwell element can be used to incorporate thermorheologically complex behaviour (see e.g. Klompen and Govaert [83]), but implementation of a second molecular process is not a straightforward addition of a second flow process when it comes to the post-yield response. A first difficulty is to characterize the individual softening responses; a second arises when the β -process flows at a lower strain than the α -process, since then its softening results in lowering stresses, making it impossible to capture the rate-dependence of the yield stress correctly.

In a previous study, we achieved the simultaneous flow of both processes by introducing a single mode description for the dual mode thermorheologically complex flow behaviour [145, 146]. This greatly simplifies the kinetics of the overall model, since no decomposition into multiple modes is required and the flow of the single mode triggers yield. In the present study we aim at a more refined solution, which encompasses a spectrum of relaxation times (see van Breemen et al. [147] and Chapter 2) for both (α and β) processes and couples the flow of the β -process to that of the α -process in the same way as suggested by [83], thus essentially creating a multi-mode-multi-process model. We check the performance of the model on four different glassy polymers over a wide range of strain rates and constant stress (creep) experiments.

3.2 Materials and Methods

Materials

Materials used are a stereo regular poly(L-lactic acid) homo polymer (PLLA), provided by PURAC Biochem (Gorinchem, The Netherlands); polycarbonate Lexan 101R (PC), provided by Sabic Innovative Plastics (Bergen op Zoom, The Netherlands); polystyrene Styron 637 (PS), provided by Dow Chemical; (Terneuzen, The Netherlands); poly(methyl methacrylate) Plexiglas 8H (PMMA), provided by Evonik Industries (Darmstadt, Germany).

For uniaxial compression tests, cylindrical samples with a diameter and height of 6mm are machined from compression moulded plaques ($200 \times 200 \times 10 \text{ mm}^3$). Dried granulates are heated in a flat mould for 15 minutes at 250 °C, 220 °C, 200 °C and 190 °C, for PC, PMMA, PLLA, and PS, respectively, and next compressed up to 300kN in 5 subsequent intervals of 5 minutes, while after each step degassing is allowed by releasing the force. Finally the mould is placed in a water-cooled cold press and quenched to room temperature (20 °C) under a moderate force of 100kN. For the DMTA samples a similar protocol is employed, but now plaques are moulded with a thickness of 2 mm for PC, PMMA, and PS, and 1 mm for PLLA.

Methods

Experiments

Dynamic Mechanical Thermal Analysis (DMTA) is performed on samples of PC, PMMA and PS, cut from the 2 mm thick compression moulded sheets, on a Rheometrics Scientific DMTA MK III in uniaxial extension at 1 Hz, with temperatures ranging for -150 °C to 200 °C. For PLLA, 1 mm thick samples are analysed on a TA Instruments Q800 in film tension mode at 1 Hz, with temperatures ranging from -100 °C to 200 °C.

Since amorphous PLLA, PS and PMMA behave brittle in extension and PC displays necking [66, 101], obstructing the investigation of their large strain response, uniaxial compression experiments are used, performed on a servo-hydraulic MTS Elastomer Testing System 810/831, equipped with a thermostatically controlled environmental chamber. The samples are compressed between two parallel flat steel plates. To prevent bulging of the sample due to friction, a thin film of skived PTFE tape (3M 5480) is attached to the sample ends and the plates are lubricated with a 1:1 mixture of detergent and water. The constant true strain rate experiments are performed at rates varying from 10^{-5} to 10^0 s⁻¹, in true strain control. Constant stress experiments are performed under true stress control at various stress levels; true stresses are calculated assuming incompressibility.

Numerical simulations

All simulations are performed using the finite element package MSC.Marc. The constitutive model is implemented by means of the user subroutine HYPELA2. The constant true strain rate as well as the constant true stress tests are simulated using one linear quad4 axisymmetric element.

3.3 Phenomenology

Figure 3.1(a) shows the DMTA results on PMMA, PC, PS, and PLLA illustrating that all these polymers display, apart from their primary (α) transition (T_g), a secondary (β) transition. Location and magnitude of the transitions evidently depend on molecular architecture. Generally the α -relaxation mechanism is attributed to full main-chain segmental mobility, whereas the β -relaxation is suggested to be related to motions on a smaller segmental length scale, be it the partial main-chain, e.g. PC, or side-group motions, e.g. PMMA, PS and PLLA. These relaxation mechanisms also contribute to deformation kinetics, as already observed by [10, 11, 13, 121]. For low strain rates a linear dependence of strain rate on yield kinetics is observed attributed to the α -process, whereas at high strain rates (or low temperatures) a

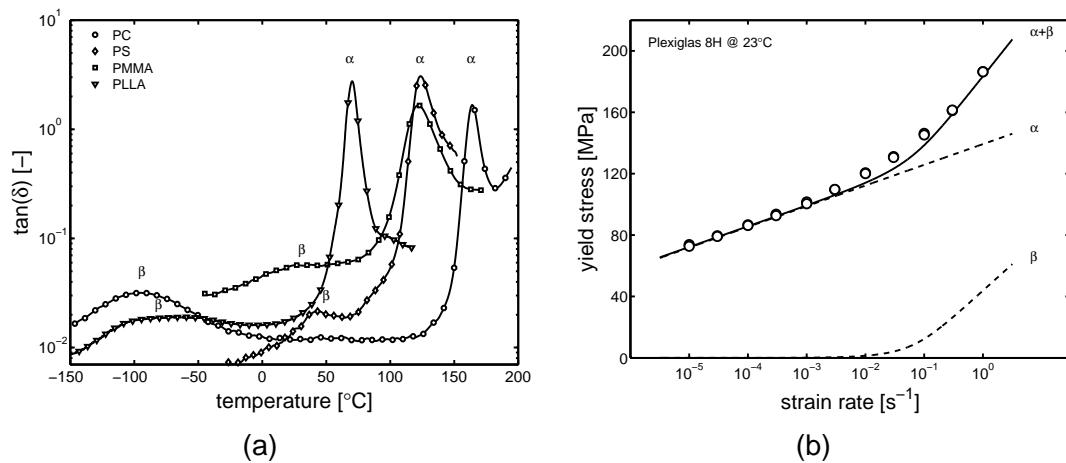


Figure 3.1: (a) DMTA data obtained from PC, PS, PMMA, and PLLA (b) yield stress data of PMMA versus strain rate applied.

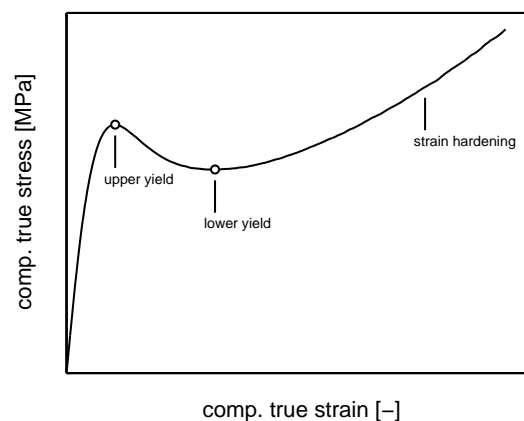


Figure 3.2: Characteristic points in an intrinsic stress-strain response

contribution of the β -process is observed, see Figure 3.1(b). This response can successfully be modelled assuming that the two molecular processes present act in parallel, and that thus an additive decomposition of the stress in an α - and β -contribution is possible, each with their own rate dependence; this decomposition is depicted by the dashed lines in Figure 3.1(b).

Figure 3.2 schematically shows the intrinsic response of glassy polymers where we recognize the (non)linear behaviour up to the upper-yield point followed by strain softening, the decrease in stress between upper- and lower-yield point, and strain hardening, the increase in stress after passing the lower-yield point. To illustrate thermorheologically complex behaviour, we compare two polymers that show over a comparable strain rate range a thermorheologically simple, PC, and a thermorheologically complex, PMMA, response, see Figure 3.3. First we notice that at high strain rates the strain hardening response of PMMA decreases markedly, leading to a drastic increase of strain softening. This effect has been reported earlier [5, 82, 105] and is attributed to viscous heating resulting in thermal softening. Consequently data in

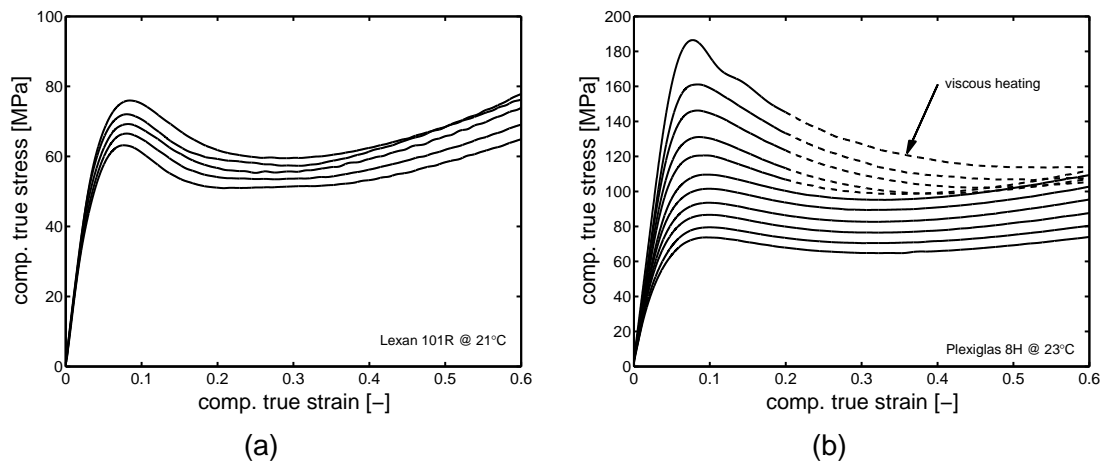


Figure 3.3: Intrinsic stress-strain response at different strain rates of (a) polycarbonate and (b) poly(methyl methacrylate).

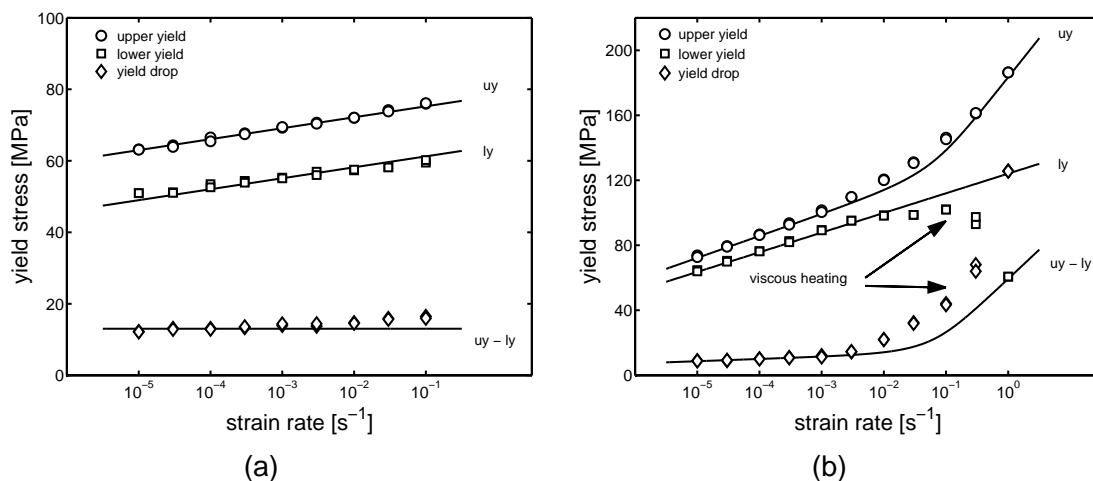


Figure 3.4: Strain-rate dependence of the upper- and lower-yield stress and corresponding yield drop of (a) polycarbonate and (b) poly(methyl methacrylate).

this strain rate regime are disregarded. Secondly, when we make a plot of yield stress versus strain rate applied, a linear dependence for PC results, see Figure 3.4(a), whereas PMMA displays a clear transition in the kinetics, see Figure 3.4(b).

Figure 3.4 includes upper yield, lower yield and the difference between these two, which is the yield drop. Remarkably the rate dependence of the lower-yield stress appears not to be affected by the β -process, the upper-yield stress clearly is; a change in strain softening is observed illustrated by an increase in yield drop. The yield drop is constant in the α -range, but in the $\alpha+\beta$ -range the difference in kinetics causes a strong rate dependence, even before softening induced by viscous heating sets in at strain rates above 10^{-1} s^{-1} .

The rationale is that strain softening occurs on application of plastic strain ($\bar{\gamma}_p$), resulting in

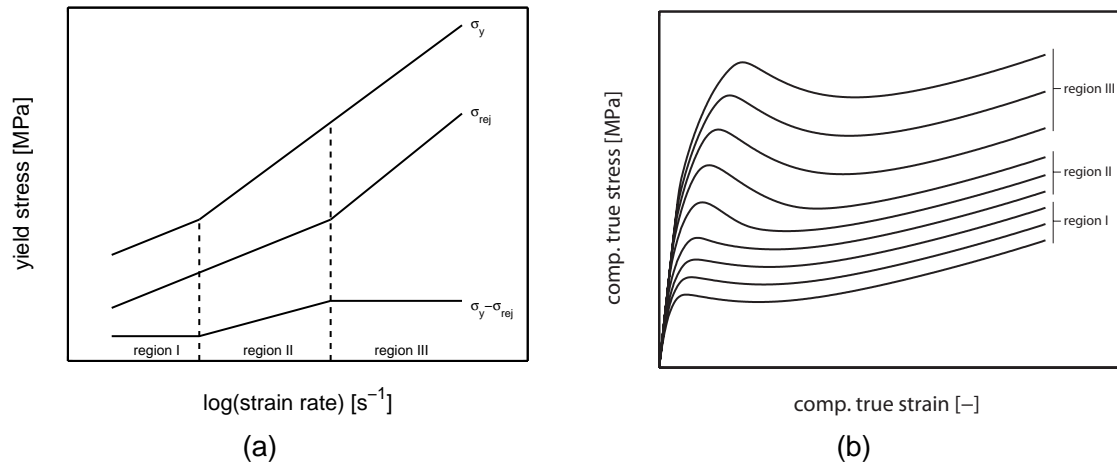


Figure 3.5: Schematic representation of the intrinsic deformation of thermorheologically simple and complex materials; (a) yield stresses versus strain rates applied and (b) true stress versus true strain.

mechanical rejuvenation of the material which causes the kinetics of plastic flow to effectively shift to higher strain rates [85] as illustrated by the lower-yield curve in Figure 3.4. The onset of the β -process not only results in a difference in dependence on strain rate of the yield stress, but also of the post-yield response, see Figure 3.4(b). In the α -range this results in a constant yield drop over the full range of rates applied, see Figure 3.4(a). When an additional molecular process is present, the transition in yield kinetics is also expected to shift upon strain softening, see Figure 3.4(b). As a consequence, within a range of strain rates a rate dependent yield drop is anticipated, and only in that range a strain-rate dependence of not only the yield stress, but also of the post-yield behaviour is caused by the onset of the β -process.

Assuming that the influence of the thermodynamic state of the β -relaxation process shifts in a similar manner as the α -process, three regions result as depicted in Figure 3.5(a). Regions I and III are those where a material behaves thermorheologically simple, the result being a constant yield drop, albeit with a difference in magnitude. This difference is explained with only one process (α) contributing in region I for both the lower- and upper-yield stress, whereas in region III two processes ($\alpha+\beta$) equally contribute to the yield drop. Region II is the transition zone where, due to the difference in kinetics of the lower- and upper-yield stress, an increase in yield drop with strain rate applied is observed. The corresponding intrinsic stress-strain responses are illustrated in Figure 3.5(b). To our knowledge no polymer glasses exist that, in the standard experimental window of strain rates and temperatures, display a response that shows all regions and therefore we use different polymers to confirm the existence of these regions. PC is in region I and only at high strain rates, and/or low temperatures, it can show a response in region II [82, 105]. PMMA is in region I, like PC, and for higher strain rates in region II. PS and PLLA are both located in region II.

This hypothesis is corroborated by compression experiments performed on PS and PLLA

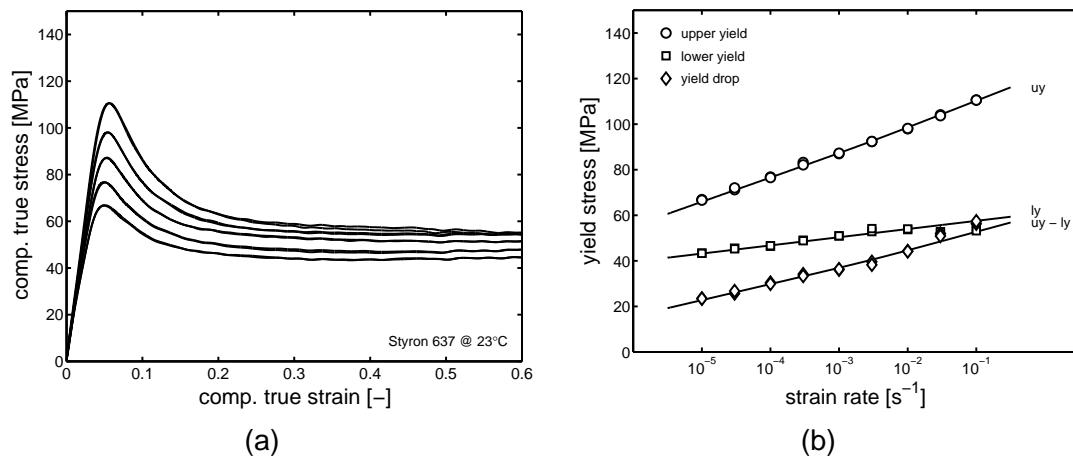


Figure 3.6: Intrinsic rate dependence of polystyrene; (a) true stress versus true strain and (b) yield stresses versus strain rate applied.

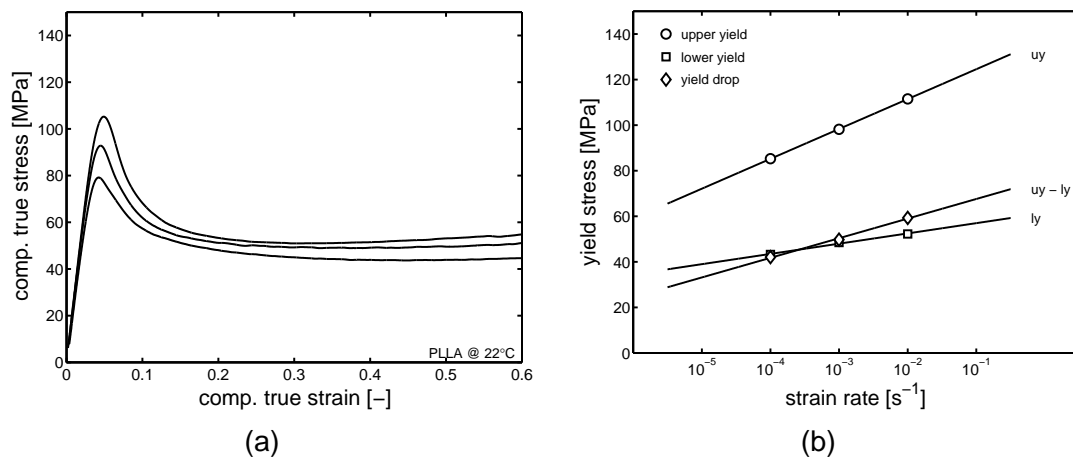


Figure 3.7: Intrinsic rate dependence of poly(L-lactic acid); (a) true stress versus true strain and (b) yield stresses versus strain rate applied.

as presented in Figures 3.6(a) and 3.7(a). For both materials the upper yield stress clearly displays a stronger rate dependence than the lower yield stress. Since these experiments are performed at moderate strain rates, viscous heating is not an issue, confirmed by the fact that no thermal softening is observed. The results clearly support our hypothesis that apparently both materials are probed in region II, where the upper-yield stress is governed by $\alpha+\beta$ and the lower yield solely by α , resulting in a rate dependent yield drop, see Figures 3.6(b) and 3.7(b). The subsequent sections concern the constitutive modelling of these observations and how to characterize the model parameters for the polymer glasses under investigation.

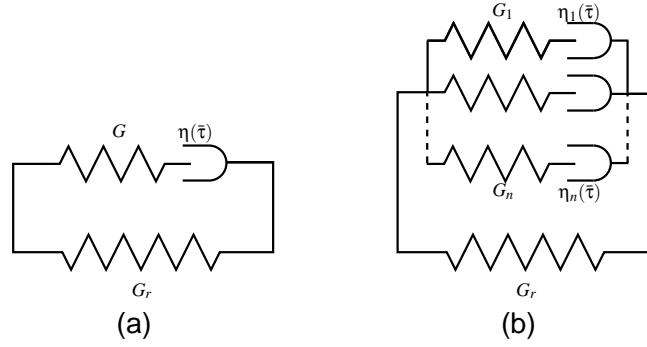


Figure 3.8: Mechanical analogue for (a) single-mode model (b) multi-mode model.

3.4 Constitutive modelling

The EGP-model for thermorheologically simple polymers

The multi-process model is an extension of the single-process EGP-model, derived for thermorheologically simple polymers as presented in its latest form in Chapter 2. In this model the total stress is split into a driving stress and a hardening stress:

$$\boldsymbol{\sigma} = \boldsymbol{\sigma}_s + \boldsymbol{\sigma}_r, \quad (3.1)$$

where $\boldsymbol{\sigma}_s$ is the driving stress representing the contribution of the intermolecular interactions, and $\boldsymbol{\sigma}_r$ is the hardening stress that is attributed to the orientation of the molecular network and modelled employing a neo-Hookean relation [59, 137]:

$$\boldsymbol{\sigma}_r = G_r \tilde{\mathbf{B}}^d. \quad (3.2)$$

Here G_r is the strain-hardening modulus and $\tilde{\mathbf{B}}^d$ is the deviatoric part of the isochoric left Cauchy-Green strain tensor. The driving stress itself is split into a hydrostatic and a deviatoric stress:

$$\boldsymbol{\sigma}_s = \boldsymbol{\sigma}_s^h + \boldsymbol{\sigma}_s^d \quad \text{where} \quad \boldsymbol{\sigma}_s^h = \kappa(J-1)\mathbf{I} \quad \text{and} \quad \boldsymbol{\sigma}_s^d = \sum_{i=1}^n G_i \tilde{\mathbf{B}}_{e,i}^d. \quad (3.3)$$

Where κ is the bulk modulus, J the volume change ratio ($J = \det(\mathbf{F}_e)$), \mathbf{I} the unity tensor, G_i the modal shear modulus and $\tilde{\mathbf{B}}_{e,i}^d$ the modal deviatoric part of the elastic isochoric left Cauchy-Green strain tensor. Superscript d and h denote, respectively, the deviatoric and hydrostatic part. The subscripts e and p refer to the elastic and plastic parts, respectively, whereas the subscript i refers to a specific mode, see van Breemen et al. [147]. For $n = 1$ the model reduces to the single mode EGP-model, see Figure 3.8. The time derivatives capturing the

evolution of J and $\tilde{\mathbf{B}}_{e,i}$ are given by:

$$\dot{J} = J \text{tr}(\mathbf{D}) \quad (3.4)$$

$$\dot{\tilde{\mathbf{B}}}_{e,i} = (\tilde{\mathbf{L}} - \mathbf{D}_{p,i}) \cdot \tilde{\mathbf{B}}_{e,i} + \tilde{\mathbf{B}}_{e,i}(\tilde{\mathbf{L}}^c - \mathbf{D}_{p,i}), \quad (3.5)$$

where $\tilde{\mathbf{L}}$ is the isochoric velocity gradient tensor. The plastic deformation rate tensor for every mode i $\mathbf{D}_{p,i}$ is related to the deviatoric stress $\sigma_{s,i}^d$ via a non-Newtonian flow rule with modified Eyring viscosity η_i [49, 59]:

$$\mathbf{D}_{p,i} = \frac{\sigma_{s,i}^d}{2\eta_i(T, \bar{\tau}, p, S)}. \quad (3.6)$$

The viscosities η_i depend on equivalent stress $\bar{\tau}$ and are described by an Eyring flow rule, with τ_0 as characteristic stress, and pressure dependence (μ) and strain softening (S) are taken into account [44, 45, 59, 119]:

$$\eta_i = \eta_{0,i,ref}(T) \frac{\bar{\tau}/\tau_0}{\sinh(\bar{\tau}/\tau_0)} \exp\left[\frac{\mu p}{\tau_0}\right] \exp[S(\bar{\gamma}_p)], \quad (3.7)$$

where the temperature dependent pre-exponential factor $\eta_{0,i,ref}(T)$ equals:

$$\eta_{0,i,ref}(T) = \eta_{0,i,ref} \exp\left[\frac{\Delta U}{RT}\right]. \quad (3.8)$$

Here ΔU is the activation energy, R the gas constant, T the absolute temperature and $\eta_{0,i,ref}$ the zero-shear viscosities, defined with respect to the reference (un-aged) state [85]. The characteristic stress, τ_0 , the total equivalent stress, $\bar{\tau}$, and the hydrostatic pressure, p , where the last two depend on the total stress, not on the modal stress, are defined according to:

$$\tau_0 = \frac{kT}{V^*} \quad ; \quad \bar{\tau} = \sqrt{\frac{1}{2} \sigma_s^d : \sigma_s^d} \quad ; \quad p = -\frac{1}{3} \text{tr}(\boldsymbol{\sigma}), \quad (3.9)$$

with k Boltzmann's constant and V^* the activation volume.

Intrinsic strain softening (S) is expressed in the state parameter (S_a), uniquely defining the current thermodynamic state of the material [85], and the softening function ($R(\bar{\gamma}_p)$),

$$S(\bar{\gamma}_p) = S_a \cdot R(\bar{\gamma}_p) \quad \text{where} \quad S \in [0, S_a]. \quad (3.10)$$

$R(\bar{\gamma}_p)$ non-linearly depends on the equivalent plastic strain $\bar{\gamma}_p$:

$$R(\bar{\gamma}_p) = \frac{(1 + (r_0 \cdot \exp(\bar{\gamma}_p))^{r_1})^{\frac{r_2-1}{r_1}}}{(1 + r_0^{r_1})^{\frac{r_2-1}{r_1}}} \quad \text{where} \quad R(\bar{\gamma}_p) \in \langle 0, 1 \rangle, \quad (3.11)$$

where r_0 , r_1 and r_2 are fitting parameters, while the equivalent plastic strain rate ($\dot{\bar{\gamma}}_p$), is coupled to the mode with the highest initial viscosity, referred to as mode 1, since that determines the development of plastic strain $\bar{\gamma}_p$:

$$\dot{\bar{\gamma}}_p = \frac{\bar{\tau}_1}{\eta_1} \quad \text{where} \quad \bar{\tau}_1 = \sqrt{\frac{1}{2} \boldsymbol{\sigma}_{s,1}^d : \boldsymbol{\sigma}_{s,1}^d}. \quad (3.12)$$

In essence, the initial thermodynamic state, and consequently the yield stress, is captured by the state parameter S_a , which increases with respect to the reference state of the material, whereas the momentary stress decreases with the onset of plastic deformation.

Extension to thermorheologically complex polymers

The experimental data as put forward in Subsection 3.3 clearly show the influence of a secondary transition on upper-yield kinetics, which manifests itself as a change in slope in the dependence of yield stress on logarithm of strain rate applied. Since the maximum relaxation time of the β -process is lower than that of the α -process, the β -process will flow before α -flow takes place. Two options are available to tackle this problem. The first is elaborately discussed in van Breemen et al. [145] and van Breemen et al. [146] and their main conclusions are discussed here briefly since the limitations in this approach influence the formulation of the multi-mode-multi-process EGP-model below.

Single mode complex viscosity

For simplicity we assume a single-mode description ($n = 1$) and isothermal conditions; Equations (3.6) and (3.7) then reduce to:

$$\mathbf{D}_p = \frac{\boldsymbol{\sigma}_s^d}{2\eta(\bar{\tau}, p, S)}, \quad \text{and} \quad (3.13)$$

$$\eta = \eta_{0,ref} \frac{\bar{\tau}/\tau_0}{\sinh(\bar{\tau}/\tau_0)} \exp\left[\frac{\mu p}{\tau_0}\right] \exp[S_a \cdot R(\bar{\gamma}_p)]. \quad (3.14)$$

To incorporate the deformation kinetics belonging to a combination of two processes, the viscosity definition of Equation (3.14) is modified to read:

$$\eta = \eta_{0,ref,\alpha} \left[\frac{\bar{\tau}/\tau_{0,\alpha}}{\sinh(\bar{\tau}/\tau_{0,\alpha})} + \frac{\eta_{0,\alpha+\beta}(S_a)}{\eta_{0,ref,\alpha} \exp[S_a]} \frac{\bar{\tau}/\tau_{0,\alpha+\beta}}{\sinh(\bar{\tau}/\tau_{0,\alpha+\beta})} \right] \exp\left[\frac{\mu p}{\tau_{0,\alpha}}\right] \exp[S_a \cdot R(\bar{\gamma}_p)] \quad (3.15)$$

where

$$\tau_{0,\alpha+\beta} = \tau_{0,\alpha} + \tau_{0,\beta}, \quad (3.16)$$

and where $\eta_{0,ref,\alpha}$ is the reference viscosity for the α -process, $\eta_{0,\alpha+\beta}$ is the viscosity for the $\alpha+\beta$ -process, $\tau_{0,\alpha}$ is the characteristic stress for the α -process and $\tau_{0,\beta}$ is the characteristic stress for the β -process. Examining Equation (3.15) in more detail shows that it is completely analogous to Equation (3.14), with the only difference that two viscosities are summed, implicitly stating that the α - and β -process are equally affected by thermal history and that the softening kinetics are the same for both processes. This is not necessarily a realistic constraint and therefore we derive a multi-process approach where all individual contributions can be modelled independently.

Multi-process approach

To capture both the primary and secondary transition in yield stress kinetics it has been shown that a modified Ree-Eyring equation, where the individual stress contributions are additive in nature, is an adequate tool. For large deformations these contributions can be interpreted as two Maxwell elements placed in parallel, each with its own stress activated non-linearities. For the multi-mode EGP-model discussed, this implies an additional driving stress; Equation (3.1) then reads:

$$\sigma = \sigma_{s,\alpha} + \sigma_{s,\beta} + \sigma_r, \quad (3.17)$$

where $\sigma_{s,\alpha}$ is the driving stress for the α -process (σ_s in Equation (3.1)), $\sigma_{s,\beta}$ the driving stress for the β -process and σ_r the hardening stress. Since the hardening stress is rate-independent, the Neo-Hookean expression of Equation (3.2) still holds. First a single Maxwell element is used for each individual process, see Figure 3.9(a), accordingly a multi-mode extension of each separate process will be derived, see Figure 3.9(b).

Similar to Equation (3.3) the driving stress for each process, $x = \alpha, \beta$, is additively decomposed in a hydrostatic and deviatoric part:

$$\sigma_{s,x} = \sigma_{s,x}^h + \sigma_{s,x}^d \quad \text{where} \quad \sigma_{s,x}^h = \kappa_x(J-1)\mathbf{I} \quad \text{and} \quad \sigma_{s,x}^d = G_x \tilde{\mathbf{B}}_{e,x}^d, \quad x = \alpha, \beta \quad (3.18)$$

where κ_x is the bulk modulus, G_x the shear modulus and $\tilde{\mathbf{B}}_{e,x}^d$ the deviatoric part of the elastic isochoric left Cauchy-Green strain tensor for process x , J the volume change ratio ($J = \det(\mathbf{F}_e)$) and \mathbf{I} the unity tensor. Superscript d and h denote, respectively, the deviatoric and hydrostatic part, whereas the subscripts e and p refer to the elastic and plastic part,

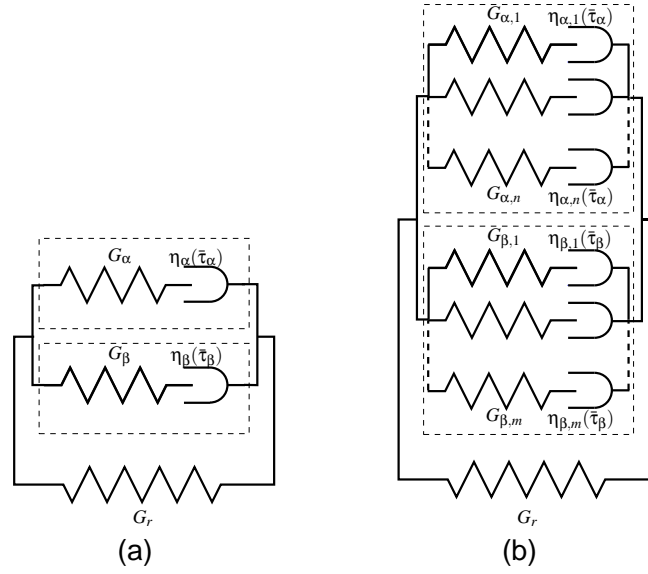


Figure 3.9: Mechanical analog for (a) multi-process model (b) multi-mode multi-process model.

respectively. The time derivatives capturing the evolution of J and $\tilde{\mathbf{B}}_{e,x}$ are given by:

$$\dot{J} = J \text{tr}(\mathbf{D}) \quad (3.19)$$

$$\dot{\tilde{\mathbf{B}}}_{e,x} = (\tilde{\mathbf{L}} - \mathbf{D}_{p,x}) \cdot \tilde{\mathbf{B}}_{e,x} + \tilde{\mathbf{B}}_{e,x} (\tilde{\mathbf{L}}^c - \mathbf{D}_{p,x}), \quad x = \alpha, \beta \quad (3.20)$$

where $\tilde{\mathbf{L}}$ is the isochoric velocity gradient tensor. In agreement with Equation (3.6), the plastic deformation rate tensor $\mathbf{D}_{p,x}$ of process x , is related to its deviatoric stress $\sigma_{s,x}^d$ via a non-Newtonian flow rule with a modified Eyring viscosity η_x :

$$\mathbf{D}_{p,x} = \frac{\sigma_{s,x}^d}{2\eta_x(T, \bar{\tau}_x, p_x, S_x)}. \quad (3.21)$$

The viscosity for each process x (η_x), individually depends on the equivalent stress $\bar{\tau}_x$, and is described by an Eyring flow rule, with $\tau_{0,x}$ being a characteristic stress. The viscosity is extended to take pressure (p_x), through pressure dependence (μ_x), and strain softening (S_x) into account:

$$\eta_x = \eta_{0,x,ref}(T) \frac{\bar{\tau}_x/\tau_{0,x}}{\sinh(\bar{\tau}_x/\tau_{0,x})} \exp\left[\frac{\mu p_x}{\tau_{0,x}}\right] \exp[S_{a,x} \cdot R(\bar{\gamma}_{p,x})], \quad (3.22)$$

where the temperature dependent pre-exponential factor $\eta_{0,x,ref}(T)$ equals:

$$\eta_{0,x,ref}(T) = \eta_{0,x,ref} \exp\left[\frac{\Delta U_x}{RT}\right]. \quad (3.23)$$

Here ΔU_x is the activation energy, $\eta_{0,x,ref}$ the zero-viscosity, defined with respect to the reference (un-aged) state [85], for process x , R the gas constant and T the absolute

temperature. The characteristic stress $\tau_{0,x}$, the equivalent stress, $\bar{\tau}_x$, and the hydrostatic pressure, p_x are defined as:

$$\tau_{0,x} = \frac{kT}{V_x^*} \quad ; \quad \bar{\tau}_x = \sqrt{\frac{1}{2} \boldsymbol{\sigma}_{s,x}^d : \boldsymbol{\sigma}_{s,x}^d} \quad ; \quad p_x = -\frac{1}{3} \text{tr}(\boldsymbol{\sigma}_x), \quad (3.24)$$

with k Boltzmann's constant and V_x^* the activation volume for process x .

The intrinsic strain softening is expressed by the state parameter ($S_{a,x}$), uniquely defining the current thermodynamic state of each process separately and the softening function $R(\bar{\gamma}_{p,x})$ capturing the softening kinetics defined as:

$$R(\bar{\gamma}_{p,x}) = \frac{(1 + (r_{0,x} \cdot \exp(\bar{\gamma}_{p,x}))^{r_{1,x}})^{\frac{r_{2,x}-1}{r_{1,x}}}}{(1 + r_{0,x}^{r_{1,x}})^{\frac{r_{2,x}-1}{r_{1,x}}}} \quad \text{where} \quad R(\bar{\gamma}_{p,x}) \in \langle 0, 1 \rangle, \quad (3.25)$$

where $r_{0,x}$, $r_{1,x}$ and $r_{2,x}$ are fitting parameters. The evolution of the equivalent plastic strain is governed by the equivalent plastic strain rate ($\dot{\bar{\gamma}}_{p,x}$):

$$\dot{\bar{\gamma}}_{p,x} = \frac{\bar{\tau}_x}{\eta_x}. \quad (3.26)$$

When, with this framework, an intrinsic stress-strain response is simulated, two yield stresses are observed, due to the maximum relaxation time of the β -process, which is lower than that of the α -process. Experiments, however, do not display this kind of response. To circumvent this numerical artefact, the equivalent plastic strain of only the α -process is employed for both the α - and β -softening kinetics; therefore Equations (3.22) and (3.25) should read:

$$\eta_x = \eta_{0,x,ref}(T) \frac{\bar{\tau}_x / \tau_{0,x}}{\sinh(\bar{\tau}_x / \tau_{0,x})} \exp\left[\frac{\mu p_x}{\tau_{0,x}}\right] \exp[S_{a,x} \cdot R(\bar{\gamma}_{p,\alpha})], \quad x = \alpha, \beta \quad (3.27)$$

with

$$R(\bar{\gamma}_{p,\alpha}) = \frac{(1 + (r_{0,x} \cdot \exp(\bar{\gamma}_{p,\alpha}))^{r_{1,x}})^{\frac{r_{2,x}-1}{r_{1,x}}}}{(1 + r_{0,x}^{r_{1,x}})^{\frac{r_{2,x}-1}{r_{1,x}}}} \quad \text{where} \quad R(\bar{\gamma}_{p,\alpha}) \in \langle 0, 1 \rangle, \quad x = \alpha, \beta \quad (3.28)$$

Multi-mode-multi-process approach

To extend the model to its full potential, see Figure 3.9(b), all relaxation times involved should be incorporated; when two processes (α and β) contribute to the deformation kinetics,

Equation (3.18) reads:

$$\boldsymbol{\sigma}_s = \boldsymbol{\sigma}_{s,\alpha}^h + \sum_{i=1}^n \boldsymbol{\sigma}_{s,\alpha,i}^d + \boldsymbol{\sigma}_{s,\beta}^h + \sum_{j=1}^m \boldsymbol{\sigma}_{s,\beta,j}^d \quad (3.29)$$

$$= \kappa_\alpha (J-1) \mathbf{I} + \sum_{i=1}^n G_{\alpha,i} \tilde{\mathbf{B}}_{e,\alpha,i}^d + \kappa_\beta (J-1) \mathbf{I} + \sum_{j=1}^m G_{\beta,j} \tilde{\mathbf{B}}_{e,\beta,j}^d. \quad (3.30)$$

For the x -process κ_x is the bulk modulus, $G_{x,i}$ the modal shear modulus and $\tilde{\mathbf{B}}_{e,x,i}^d$ the modal deviatoric part of the elastic isochoric left Cauchy-Green strain tensor, with $x = \alpha, \beta$. J and \mathbf{I} are the volume change ratio and the unity tensor, respectively. For $n = 1$ and $m = 1$ the model reduces to the multi-process model of Equation (3.18).

Equations (3.19) through (3.24) also need rewriting:

$$\dot{J} = J \text{tr}(\mathbf{D}) \quad (3.31)$$

$$\dot{\tilde{\mathbf{B}}}_{e,\alpha,i} = (\tilde{\mathbf{L}} - \mathbf{D}_{p,\alpha,i}) \cdot \tilde{\mathbf{B}}_{e,\alpha,i} + \tilde{\mathbf{B}}_{e,\alpha,i} (\tilde{\mathbf{L}}^c - \mathbf{D}_{p,\alpha,i}) \quad (3.32)$$

$$\dot{\tilde{\mathbf{B}}}_{e,\beta,j} = (\tilde{\mathbf{L}} - \mathbf{D}_{p,\beta,j}) \cdot \tilde{\mathbf{B}}_{e,\beta,j} + \tilde{\mathbf{B}}_{e,\beta,j} (\tilde{\mathbf{L}}^c - \mathbf{D}_{p,\beta,j}), \quad (3.33)$$

with:

$$\mathbf{D}_{p,\alpha,i} = \frac{\boldsymbol{\sigma}_{s,\alpha,i}^d}{2\eta_\alpha(T, \bar{\tau}_\alpha, p_\alpha, S_\alpha)} \quad \text{and} \quad \mathbf{D}_{p,\beta,j} = \frac{\boldsymbol{\sigma}_{s,\beta,j}^d}{2\eta_\beta(T, \bar{\tau}_\beta, p_\beta, S_\beta)}, \quad (3.34)$$

while:

$$\eta_\alpha = \eta_{0,\alpha,i,ref}(T) \frac{\bar{\tau}_\alpha/\tau_{0,\alpha}}{\sinh(\bar{\tau}_\alpha/\tau_{0,\alpha})} \exp\left[\frac{\mu p_\alpha}{\tau_{0,\alpha}}\right] \exp[S_{a,\alpha} \cdot R(\bar{\gamma}_{p,\alpha})] \quad (3.35)$$

$$\eta_\beta = \eta_{0,\beta,j,ref}(T) \frac{\bar{\tau}_\beta/\tau_{0,\beta}}{\sinh(\bar{\tau}_\beta/\tau_{0,\beta})} \exp\left[\frac{\mu p_\beta}{\tau_{0,\beta}}\right] \exp[S_{a,\beta} \cdot R(\bar{\gamma}_{p,\alpha})], \quad (3.36)$$

with pre-exponential factors equal to:

$$\eta_{0,\alpha,i,ref}(T) = \eta_{0,\alpha,i,ref} \exp\left[\frac{\Delta U_\alpha}{RT}\right] \quad \text{and} \quad \eta_{0,\beta,j,ref}(T) = \eta_{0,\beta,j,ref} \exp\left[\frac{\Delta U_\beta}{RT}\right]. \quad (3.37)$$

Since the characteristic stresses, equivalent stresses and pressures are global, and not modal, process quantities, the relations in Equation (3.24) are adopted accordingly. Equation (3.28), representing the softening kinetics, remains unaffected since α -flow still triggers β -softening, and softening of all modes is triggered by α -flow. However, the shape of the softening function can be manipulated for each process individually via the r -parameters, likewise can we adapt the value of the parameter ($S_{a,x}$) capturing the thermodynamic state of the material. Similar to the multi-mode model, the equivalent plastic strain rate is coupled to the mode with the highest

relaxation time, referred to as the α -mode where $i = 1$, according to:

$$\dot{\gamma}_{p,\alpha} = \frac{\bar{\tau}_{\alpha,1}}{\eta_{\alpha,1}} \quad \text{where} \quad \bar{\tau}_{\alpha,1} = \sqrt{\frac{1}{2} \boldsymbol{\sigma}_{s,\alpha,1}^d : \boldsymbol{\sigma}_{s,\alpha,1}^d}. \quad (3.38)$$

3.5 Results and discussion

Parameter characterization

The effect of thermorheologically complex modelling on the upper- and lower-yield kinetics, as well as softening kinetics, will be demonstrated using three different materials (PS, PLLA and PMMA) all displaying a thermorheologically complex response. Determination of the model parameters is performed on the intrinsic stress-strain curves. Characterization involves the following sequential steps:

1. the upper- and lower-yield kinetics:
 $\tau_{0,\alpha}$ (V_α^*) and $\tau_{0,\beta}$ (V_β^*) are estimated from the slope of yield stress versus logarithm of strain rate [85],
2. from a plot of true stress versus $\lambda^2 - \lambda^{-1}$ the slope at high strains identifies the strain hardening modulus G_r ,
3. the reference (un-aged) state ($S_{a,\alpha} = 0$) of the material is established:
 G_α and $\eta_{0,\alpha,ref}$, or when the multi-mode framework is employed $G_{\alpha,i}$ and $\eta_{0,\alpha,i,ref}$ [147],
4. if experiments are performed at different temperatures, the determination of ΔU_α follows,
5. the softening kinetics of the α -process are determined:
 $R(\bar{\gamma}_{p,\alpha})$, with fitting parameters $r_{0,\alpha}$, $r_{1,\alpha}$ and $r_{2,\alpha}$ and the thermodynamic state of the α -process reflected in the value of $S_{a,\alpha}$ [85],
6. for the β -process the steps 3 through 5 are repeated.

Since the experimental data of the polymers under investigation are positioned in a specific regime (PS and PLLA in region II) or in a combination of two regimes (PMMA in regions I and II), see Figure 3.5(a), the procedure to obtain the parameters may differ, the sequence however remains unaltered.

Application to PS and PLLA

In the pre-yield regime, both PS and PLLA, display almost a linear elastic response, see Figures 3.6 and 3.7. Application of the spectrum-determination routine, see Chapter 2, yields

two modes for both PS and PLLA. However, approximation of the pre-yield regime with a single mode for each individual process leads to similar results. Therefore a single-mode Maxwell representation for each separate process will suffice, see Figure 3.9(a).

PS

Step 1 involves the determination of the slopes when yield stress is plotted versus the logarithm of strain rate. For the α -process the lower-yield slope is used, where for the β -process we use the upper-yield slope. The slope of upper yield is related to $\tau_{0,\alpha+\beta}$, and employing Equation (3.16) the characteristic stress of the β -process is derived. The strain rate dependence is defined according to:

$$\tau_{0,y} = \frac{\sqrt{3} - \mu}{3} \cdot \frac{\sigma_{0,y}^*}{\ln(10)} \quad \text{with } y = \alpha, \alpha + \beta, \quad (3.39)$$

where $\sigma_{0,y}^*$ is the slope in the yield stress versus logarithm of strain rate plot. The characteristic stresses are $\tau_{0,\alpha} = 0.98$ MPa and $\tau_{0,\beta} = 1.54$ MPa. For the strain hardening modulus a value of $G_r = 8$ MPa is found, which is the tangent at large deformations when true stress is plotted versus $\lambda^2 - \lambda^{-1}$; its value corresponds well with data found in literature [150, 152]. Since no experimental data at different temperatures are available, step 4, where the activation energy is determined, becomes obsolete.

Next in the procedure of model parameter determination is the derivation of the parameters governing the α -softening kinetics, i.e. $r_{0,\alpha}$, $r_{1,\alpha}$, $r_{2,\alpha}$ and the state parameter $S_{a,\alpha}$, capturing the current thermodynamic state of the material. Since the deformation kinetics of PS are completely situated in region II, see Figures 3.5 and Figure 3.6, an exact determination of $S_{a,\alpha}$ is hindered, however a region of possible values can be defined. The principle is graphically explained in Figure 3.10(a), where the experimental upper- and lower-yield data, as displayed in Figure 3.6(b), are plotted over a larger strain rate range. Two circumstances, defining the limits, are available. The first being the situation where the upper-yield data are obtained in such an experimental strain rate window that, if experiments at lower rates are performed, a prompt transition in upper-yield data will be observed. As a consequence, when assuming an equal shift of the thermodynamic state in β -kinetics, the transition where a contribution of the β -process on lower-yield kinetics will be observed, shifts to higher strain rates, resulting in the definition of $S_{a,max}$. The other option being a similar assumption, but now for the transition in lower-yield kinetics. Performing experiments at higher strain rates will result in an immediate transition in lower-yield kinetics, which implies that, again assuming an equal shift, a transition in upper-yield kinetics at lower strain rates as compared to the first option will be observed, leading to the definition of $S_{a,min}$. For the PS data available, the S_a values applicable range from 12.2 to 14.6; here an intermediate value of 14.0 is used in the simulations. Likewise, due to the absence of a change in slope, in either the lower- or upper-yield kinetics, the

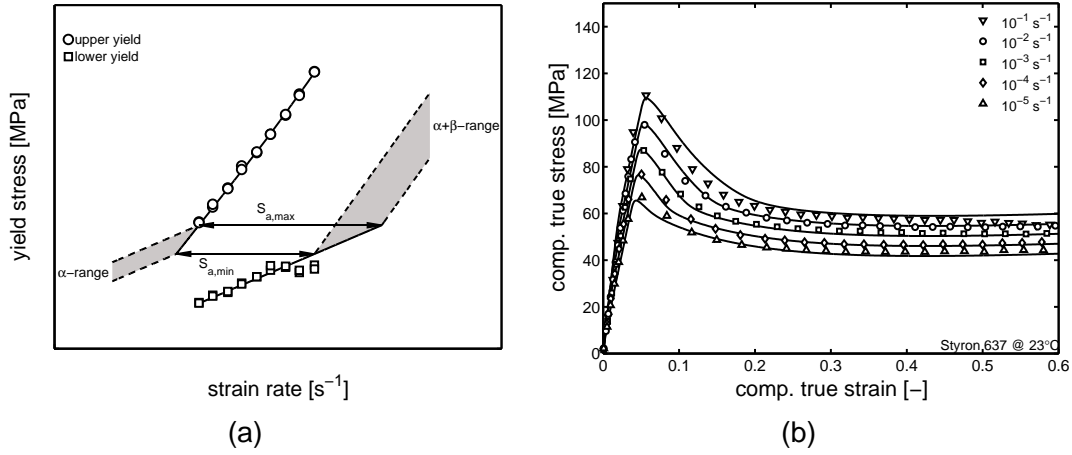


Figure 3.10: (a) Applicable ranges of the state parameter capturing the current thermodynamic state of the material (b) intrinsic stress/strain response of polystyrene, where the markers are the experiments and the solid lines are the simulations.

Table 3.1: input parameters for PS.

G_{α} [MPa]	$\eta_{0,\alpha,ref}$ [MPa · s]	V_{α}^* [nm^3]	$S_{a,\alpha}$ [-]	$r_{0,\alpha}$ [-]	$r_{1,\alpha}$ [-]	$r_{2,\alpha}$ [-]
550	$2.7 \cdot 10^{12}$	4.17	14.0	0.99	50.0	-3.0

G_{β} [MPa]	$\eta_{0,\beta,ref}$ [MPa · s]	V_{β}^* [nm^3]	$S_{a,\beta}$ [-]	$r_{0,\beta}$ [-]	$r_{1,\beta}$ [-]	$r_{2,\beta}$ [-]
550	$1.0 \cdot 10^{-1}$	2.65	14.0	0.99	50.0	-4.0

G_r [MPa]	κ [MPa]	μ_{α} [-]	μ_{β} [-]
8.0	$3.5 \cdot 10^3$	0.14	0.14

determination of the state parameter capturing the thermodynamic state of the β -process $S_{a,\beta}$ is obstructed, therefore a similar value of 14.0 is employed. The r -parameters influencing the shape of the softening functions are defined in an iterative best-fit routine, a detailed procedure is found in Klompen et al. [85]. The total parameter set identified from the experimental data of PS is tabulated in Table 3.1; using this set results in the solid lines as depicted in Figure 3.10(b), where measured and simulated data are in good agreement.

PLLA

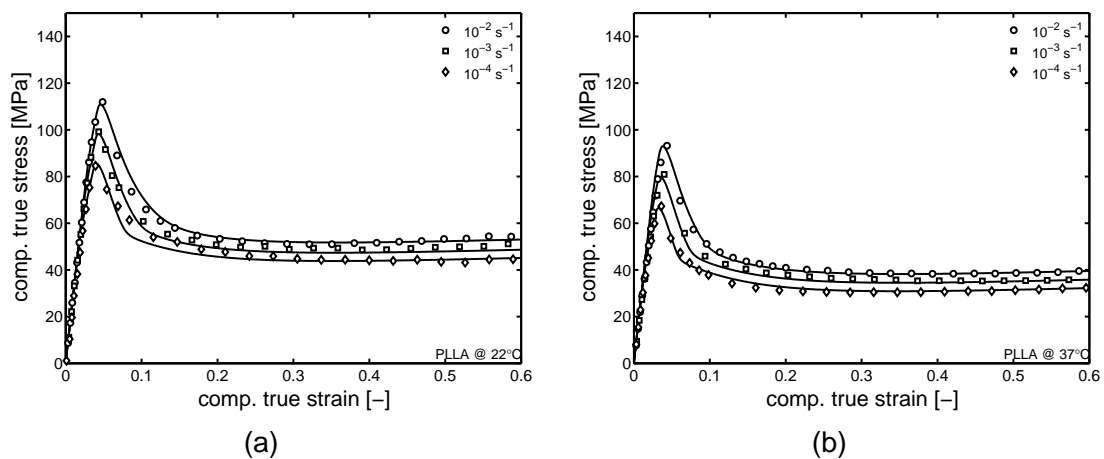
A procedure analogous to that of PS is followed in determining the parameter set for PLLA, with this difference, that for PLLA data at different temperatures are available. The temperature

Table 3.2: input parameters for PLLA.

G_α [MPa]	$\eta_{0,\alpha,ref}$ [MPa · s]	V_α^* [nm ³]	$S_{a,\alpha}$ [-]	$r_{0,\alpha}$ [-]	$r_{1,\alpha}$ [-]	$r_{2,\alpha}$ [-]
550	$1.0 \cdot 10^{15}$	4.75	12.25	0.99	20.0	-5.0

G_β [MPa]	$\eta_{0,\beta,ref}$ [MPa · s]	V_β^* [nm ³]	$S_{a,\beta}$ [-]	$r_{0,\beta}$ [-]	$r_{1,\beta}$ [-]	$r_{2,\beta}$ [-]
550	$3.5 \cdot 10^1$	1.75	12.25	0.99	100.0	-12.5

ΔU_α [kJ/mol]	ΔU_β [kJ/mol]	G_r [MPa]	κ [MPa]	μ_α [-]	μ_β [-]
480	100	3.45	$3.5 \cdot 10^3$	0.0	0.0

**Figure 3.11:** Intrinsic stress-strain response of poly(L-lactic acid) at (a) 22 °C and (b) 37 °C, where the markers are the experiments and the solid lines the model predictions.

dependence of the α - and β -processes, represented in the characteristic stresses, see Equation (3.24), and activation energies, see Equation (3.23), is determined from compression tests performed at 2 different temperatures, 22 °C and 37 °C, at strain rates varying from 10^{-4} s^{-1} to 10^{-2} s^{-1} , respectively. The parameter set obtained is tabulated in Table 3.2 and corresponding compression simulations are compared to the experimental data in Figure 3.11.

The upper- and lower-yield stress evolution for the simulations, solid lines, and experiments, markers, at the two different temperatures are plotted in Figure 3.12(a), and a quantitative prediction is obtained. As is known from literature the same kinetics that dictates the upper yield at constant strain rate, also determines the time-to-failure under static load [16, 86, 98, 106]. Subsequently, the time-dependent response is quantified, employing the same parameter set, on long-term static loading experiments, i.e. creep experiments. These tests are performed at the same temperatures as compared to the constant strain rate

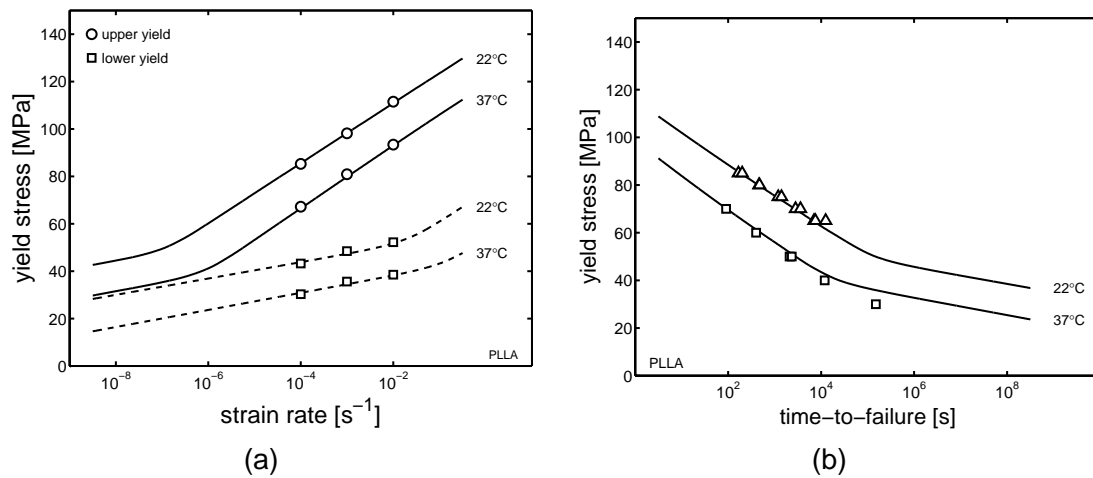


Figure 3.12: (a) Rate dependence of the lower- and upper yield stress of poly(L-lactic acid) at 2 different temperatures (b) life-time predictions of poly(L-lactic acid) at different temperatures and stresses applied.

experiments. The time-to-failure is defined as the moment when a sudden dramatic increase in strain versus time is observed. When plotting the failure times as determined from the experiments versus the simulated time-to-failure, an excellent agreement is achieved, see Figure 3.12(b).

Application to PMMA

Finally the material behaviour of PMMA is used to illustrate the capabilities of the new multi-mode-multi-process EGP-model. A multi-mode approach to model the pre-upper-yield regime is necessary due to its highly non-linear response. The PMMA data used are the same as depicted in Figures 3.3(b) and 3.4(b). Since the characteristic stresses are the same for each mode in a specific process, see Equation (3.36), the same procedure as described for PS and PLLA is employed to characterize them, yielding $\tau_{0,\alpha} = 3.03$ MPa and $\tau_{0,\beta} = 5.19$ MPa. The strain-hardening modulus is fitted on the large strain regime, returning a value of $G_r = 26$ MPa. Besides the bulk modulus κ , the pressure dependence parameters μ for both the α - and β -process, which are assumed equal, are adopted from literature [56, 82, 146]. Successively a discrete spectrum of relaxation modes, associated with the α -process is fitted on a measurement of true stress versus true strain at a strain rate of $10^{-5} s^{-1}$, which is well within the α -regime of the upper-yield data. The procedure to obtain a relaxation spectrum out of a single uniaxial compression experiment is elaborately discussed in Chapter 2. The routine proposed, results in a spectrum consisting of 8 modes, tabulated in Table 3.3. For a material behaving thermorheologically simple, all relaxation times are equally affected by the total stress ($\bar{\tau}$), pressure dependence (μ), and thermal history (S_a). The latter implies that a unique determination of the parameters governing the α -softening kinetics is possible, where the value of $S_{a,\alpha}$ is obtained by simply shifting the complete spectrum to its appropriate

Table 3.3: Reference spectrum for the α -process of PMMA 8H.

mode	$\eta_{0,\alpha,i,ref} [MPa \cdot s]$	$G_i [MPa]$	$\lambda_i [s]$
1	$2.26 \cdot 10^7$	$4.43 \cdot 10^2$	$5.10 \cdot 10^4$
2	$5.55 \cdot 10^5$	$7.65 \cdot 10^1$	$7.25 \cdot 10^3$
3	$1.06 \cdot 10^5$	$7.65 \cdot 10^1$	$1.39 \cdot 10^3$
4	$1.93 \cdot 10^4$	$5.04 \cdot 10^1$	$3.83 \cdot 10^2$
5	$4.34 \cdot 10^3$	$2.83 \cdot 10^1$	$1.83 \cdot 10^2$
6	$3.37 \cdot 10^3$	$2.65 \cdot 10^1$	$1.27 \cdot 10^2$
7	$1.22 \cdot 10^3$	$2.00 \cdot 10^1$	$6.10 \cdot 10^1$
8	$2.00 \cdot 10^3$	$9.88 \cdot 10^1$	$2.02 \cdot 10^1$

Table 3.4: input parameters for PMMA.

$G_{\alpha,tot} [MPa]$	$\eta_{0,\alpha,ref} [MPa \cdot s]$	$V_{\alpha}^* [nm^3]$	$S_{a,\alpha} [-]$	$r_{0,\alpha} [-]$	$r_{1,\alpha} [-]$	$r_{2,\alpha} [-]$
818	$2.3 \cdot 10^7$	1.35	6.7	0.96	5.0	-3.5

$G_{\beta,tot} [MPa]$	$\eta_{0,\beta,ref} [MPa \cdot s]$	$V_{\beta}^* [nm^3]$	$S_{a,\beta} [-]$	$r_{0,\beta} [-]$	$r_{1,\beta} [-]$	$r_{2,\beta} [-]$
800	$6.0 \cdot 10^{-2}$	0.79	6.7	0.96	30.0	-5.5

$G_r [MPa]$	$\kappa [MPa]$	$\mu_{\alpha} [-]$	$\mu_{\beta} [-]$
26.0	$3.0 \cdot 10^3$	0.13	0.13

thermodynamic state, resulting in a value of $S_{a,\alpha} = 6.7$. The parameters capturing the shape of the softening function are fitted as described in detail in Klompen et al. [86]. In contrast to the α -process, the β -process is modelled with only a single mode. The complete set of data is tabulated in Table 3.4, and used in the simulations in Figure 3.13. At high strain rates, the coupling of α -flow to β -softening affects the strain at yield which is slightly higher than the experimental data. Also thermal softening, present at high strain rates, is not taken into account, resulting in a less pronounced strain softening response.

3.6 Conclusions

The aim of this study was to create a framework for polymer glasses behaving thermorheologically complex. In principle the new model consists of two multi-mode EGP-models [147] acting in parallel. Our approach to capture thermorheologically complex yield phenomena, is based on the Ree-Eyring modification of Eyring's flow theory, as already

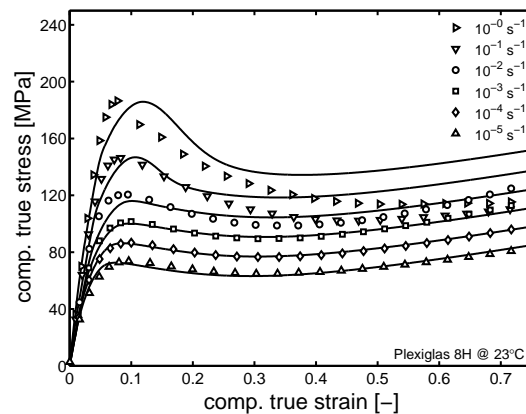


Figure 3.13: Intrinsic stress-strain response of poly(methyl methacrylate) employing the multi-mode-multi-process EGP-model.

employed by numerous researchers decades ago. Whether the post-yield response, i.e. strain softening, also displays thermorheologically complex behaviour remains unidentified. Some observations on the post yield intrinsic response of PMMA and PC suggest complex behaviour, Arruda et al. [5] and Mulliken and Boyce [105]. Both related the increased softening at high deformation rates solely to thermal effects. In our opinion thermal effects indeed partially explain the increased yield drop at deformation rates above 10^{-2} s^{-1} . In our experiments on PS and PLLA, at strain rates below 10^{-2} s^{-1} , which is well within the range where experiments can be considered isothermal, an increased yield drop is observed. This observation is well rationalized by a secondary process contributing to the post-yield softening response and implies that a rate dependent yield drop is of an intrinsic nature. From these observations it is evident that three regions can be formulated for the pre- and post-yield response. In the first regime, the deformation is controlled by a single (α) molecular process and, as a result, the yield-drop is independent of strain rate applied. The second regime is controlled by multiple relaxation processes, where due to the difference in strain rate dependence of lower- (only α) and upper-yield ($\alpha+\beta$), a rate dependent yield-drop is observed. In the last region both processes contribute in an equal manner to lower- as well as upper-yield data, again resulting in a rate independent yield-drop. With the extension of the EGP-model, we can predict strain-rate dependence over a wide range of strain rates and temperatures. Similar to the life-time predictions performed by Klompen et al. [86] on PC, we showed that a thermorheologically complex approach is required to predict both the intrinsic response and time-to-failure of PLLA, with a single parameter set.

Flat-tip micro-indentation of glassy polymers¹

Abstract

Abstract: Flat-tip micro-indentation tests are performed on quenched and annealed polymer glasses at various loading speeds. The results are analysed using an elasto-visco-plastic constitutive model that captures the intrinsic deformation characteristics of a polymer glass: a strain-rate dependent yield stress, strain softening and strain hardening. The advantage of this model is that changes in yield stress due to physical ageing are captured in a single parameter. The two materials studied (polycarbonate (PC) and poly(methyl methacrylate) (PMMA)), are both selected for the specific rate dependence of the yield stress that they display at room temperature. Within the range of strain rates experimentally covered, the yield stress of PC increases linearly with the logarithm of strain rate, whereas for PMMA a characteristic change in slope can be observed at higher strain rates. We demonstrate that, given the proper definition of the viscosity function, the flat-tip indentation response at different indentation speeds can be described accurately for both materials. Moreover, it is shown that the parameter set obtained for each material is also representative for the mechanical response on a macroscopic scale. This implies that the thermodynamic states of PC and PMMA can be determined by fitting a single parameter on a single indentation test.

¹partially reproduced from: L.C.A. van Breemen, T.A.P. Engels, C.G.N. Pelletier, L.E. Govaert and J.M.J. den Toonder, Numerical simulation of flat-tip micro-indentation of glassy polymers: influence of loading speed and thermodynamic state, *Philosophical Magazine*, 89(8) 677–696

4.1 Introduction

Instrumented indentation is a versatile technique to probe local mechanical properties of films and/or bulk materials [111, 151]. In principle, a well-defined body is pressed into the surface of a material while measuring both the applied load and the resulting penetration depth. The data obtained can subsequently be analysed to determine the mechanical properties of the indented material. Especially with respect to the elastic modulus quantitative analytical methods are available [74, 110]. With the aid of the elastic-visco-elastic correspondence principle these methods are also applicable to quantitatively assess the visco-elastic properties [37, 38, 42, 43, 88]. With respect to the large strain mechanical properties the analysis of indentation data is less straightforward. Even for the determination of the yield stress, a direct analytical method is not available and an estimate can only be obtained using empirical scaling laws. Although these have been proven to be quite useful, the scaling factor between hardness and yield strength is not universal for all materials [78, 96, 135].

The rise of FEM-based analysis methods opened up new possibilities. Supported by the development of appropriate finite-strain constitutive relations a detailed analysis of local deformation and stress fields became feasible. An excellent example is the work in Larsson's group on Vickers [55] and Berkovich [89] indentation of elasto-plastic materials. In the case of polymeric materials, the analysis of such a contact problem is complicated because of the complex large-strain behaviour, characterized by a pronounced strain-rate and pressure dependence of the yield stress and a post-yield response that is governed by a combination of strain softening and strain hardening. Especially in the case of amorphous polymer glasses considerable effort has been directed towards the development of 3D constitutive models that are capable to capture the experimentally observed intrinsic behaviour, e.g. in the group of Mary Boyce at MIT [4, 21, 70], the group of Paul Buckley in Oxford [32, 33, 156], and in our Eindhoven group [59, 85, 138]. These developments enabled a quantitative analysis of localization and failure in polymer glasses [22, 85, 148, 150, 158, 159], and revealed the crucial role of the intrinsic post-yield characteristics on macroscopic strain localization.

Van Melick et al. [148] were the first to apply such a constitutive model to spherical-tip indentation of polystyrene (PS), in order to analyse radial craze formation. They demonstrated that the load-penetration depth curves could be well reproduced for different indentation speeds by numerical simulations using the Eindhoven Glassy Polymer model (EGP-model) [85, 147]. In a subsequent study, Swaddiwudhipong et al. [133] showed that the same model was unable to describe the Berkovich indentation response of another glassy polymer; polycarbonate (PC). To reproduce the response at different indentation speeds correctly, they required an additional strain gradient effect. It should be noted, however, that they adopted the parameters for polycarbonate from Govaert et al. [59] without verifying that this set was appropriate for the thermodynamic state of their own polycarbonate samples. In a more recent study, Anand and Ames [2] presented an extension of the Boyce, Parks, Argon model, the

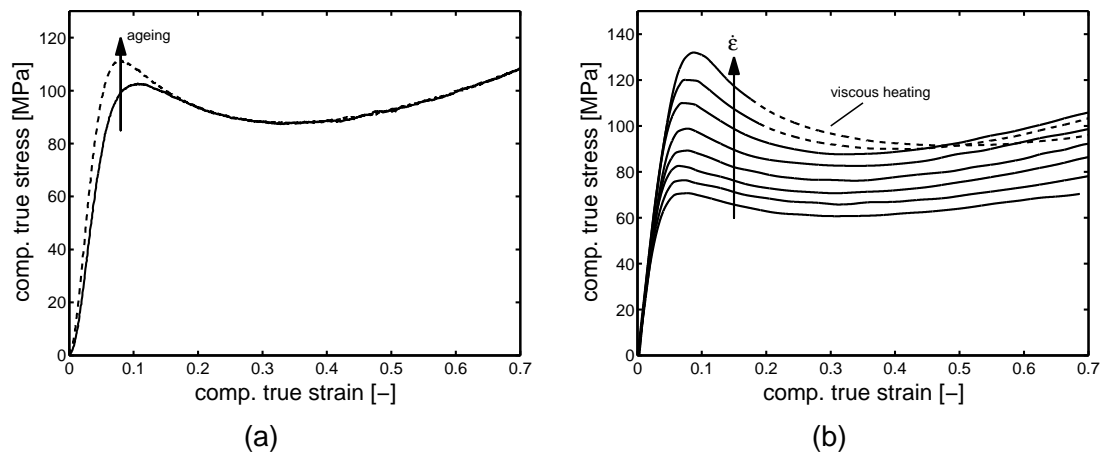


Figure 4.1: Stress-strain response of PMMA in uniaxial compression: (a) influence of thermal history; annealed sample (- -) and quenched sample (-); (b) influence of strain rate.

BPA-model [21], which proved successful in describing the conical-tip indentation of PMMA, albeit at a single indentation speed.

In this chapter, we demonstrate that the new extension of the EGP-model, as described in Chapters 2 and 3, is capable of quantitatively describing the indentation response of PC and PMMA over a range of indentation speeds. A flat-ended cone is chosen as indenter body, since this specific tip geometry results in a load-penetration depth curve in which elastic and plastic ranges are clearly distinguishable. At low indentation depths the response is governed by elastic deformation, whereas at large depths plastic deformation sets in, leading to a marked change in slope and resulting in a characteristic knee-shaped load-displacement curve [95, 96, 155]. Moreover, we will show that this is accomplished by using a parameter set which also quantitatively describes the material's mechanical response in macroscopic testing.

4.2 Phenomenology

To study the intrinsic stress-strain response of polymers, an experimental set-up is required in which the sample can deform homogeneously up to large plastic deformations. Examples of such techniques are uniaxial compression tests [4, 150] or video-controlled tensile tests [68]. An illustrative example of the intrinsic stress-strain response of a polymer glass is presented in Figure 4.1(a). Typical features are strain softening, the decrease in true stress that is observed after passing the yield point, and strain hardening at large deformations. Strain hardening is generally interpreted as the result of a stress contribution of the orienting molecular network [4, 71, 137, 150]. Strain softening is closely related to the fact that polymer glasses are not in a state of thermodynamic equilibrium. Over time the glass will strive towards equilibrium, a process usually referred to as physical ageing [75], and, as a result, its mechanical properties

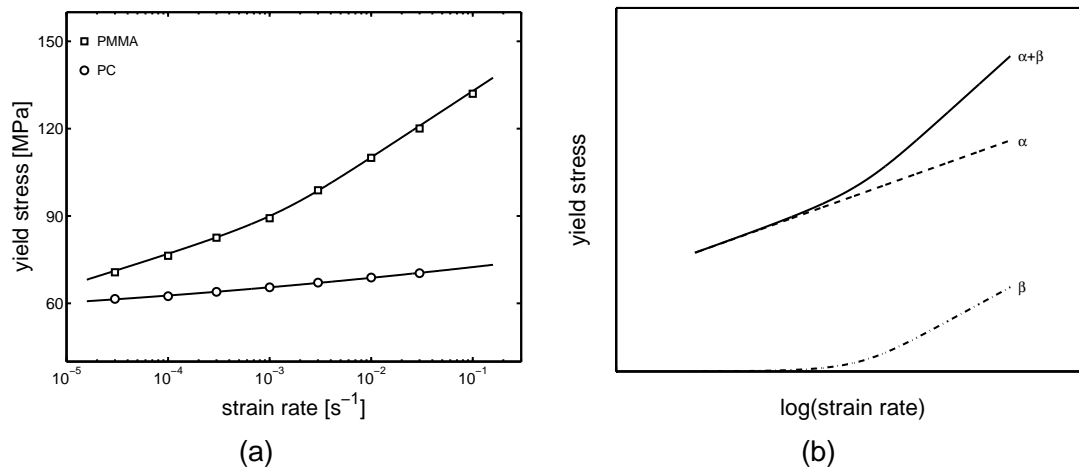


Figure 4.2: (a) Yield stress of PMMA and PC in uniaxial compression as a function of strain rate; (b) decomposition of the strain-rate dependence of the yield stress into two separate molecular contributions.

change. This is demonstrated in Figure 4.1(a) which compares the intrinsic response of two samples with different thermodynamic state. It is clear that physical ageing results in an increase of both modulus and yield stress, but upon plastic deformation the differences between the curves disappear and eventually they fully coincide at a strain of approximately 0.3. Apparently all influence of thermal history is erased at that strain and both samples are transformed to a similar, mechanically 'rejuvenated' state. From Figure 4.1(a) it is clear that an increase of yield stress, due to a thermal treatment, will directly imply an increase in strain softening. The influence of molecular weight on the intrinsic response is usually negligible [85, 159], which makes thermal history the key factor in influencing the intrinsic properties of a specific polymer glass. The thermal history is also reflected in the long-term failure behaviour of polymer glasses. This was demonstrated for PC, where an annealing treatment, leading to an increase in yield stress, improved the life time under constant stress by orders of magnitude [86].

The intrinsic stress-strain response of glassy polymers also displays a pronounced dependence on the time scale of the experiment. This is illustrated in Figure 4.1(b), where the strain-rate dependence of the compressive stress-strain response of poly(methyl methacrylate) (PMMA) is shown [82]. It is clear that with increasing strain rate the overall stress level in the yield and post-yield range increases. Also the amount of strain softening and strain hardening appears subject to change. At strain rates over $3 \cdot 10^{-2} s^{-1}$ the material heats up due to viscous dissipation, and, as a result, strain hardening disappears [5].

The strain-rate dependence of the yield stress for PMMA and PC is shown in Figure 4.2(a). For the latter the yield stress increases linearly with the logarithm of strain rate, which indicates that in this range of strain rates the deformation of PC is governed by a single molecular

relaxation process [14, 83], i.e. the amorphous α -transition (main-chain segmental motion). Although this chapter only focuses on the isothermal response, it is relevant to note that the stress contribution displays an Arrhenius type of temperature dependence which leads to a horizontal shift of the yield stress characteristic along the logarithmic strain rate axis: this type of behaviour is generally referred to as thermorheologically simple behaviour.

In the case of PMMA the strain-rate dependence of the yield stress displays a clear change in slope which was shown to be related to onset of a stress contribution of a second molecular process, the β -transition [121–123]; a secondary glass transition related to side-chain mobility. A successful description of such a yield response is obtained using a Ree-Eyring approximation, where, as schematically represented in Figure 4.2(b), it is assumed that each process can be described with an Eyring flow rule, whereas the stress contributions of both molecular mechanisms are additive [120], see also Chapter 3. In the case of PMMA, it should be noted that each process possesses its own characteristic activation energy, implying that curves measured at different temperatures will no longer coincide by horizontal shifting. A correct translation to other temperatures can only be achieved by application of rate-temperature superposition on each contribution separately: this is generally referred to as thermorheologically complex behaviour.

4.3 Experimental and numerical

Materials and sample preparation

Materials

The materials used in this study is polycarbonate, PC, (Makrolon, Bayer), obtained in the form of extruded sheet of 3 mm thickness, and poly(methyl methacrylate), PMMA (Perspex, ICI) obtained in the form of extruded rod of 6 mm diameter.

Sample preparation: PC

For the uniaxial tensile tests, samples according to ASTM D638 are milled from the extruded sheet. To avoid an influence of a processing-induced yield stress distribution over the thickness of the samples [61], the tensile bars are milled to a thickness of 1.7 mm, i.e. identical to that of the test section of the samples for planar extension and shear.

To enable a direct comparison between the indentation tests and the conventional macroscopic tests, indentation experiments are performed on a cross-section of a tensile sample. A small specimen is cut from the gauge-section of the sample and subsequently the cross-sectional

surface is cryogenically cut, using a microtome, to obtain a smooth surface. Flat-tip indentation tests are performed in the middle of the sample area. For other indentation tests, samples of a size of 10 mm × 10 mm are cut from the extruded PC sheet.

To change the thermodynamic state of the material, some of the samples are annealed at 120 °C for 48 hours in an air circulated oven and subsequently slowly air-cooled to room temperature.

Sample preparation: PMMA

Cylindrical samples of $\varnothing 6$ mm × 6 mm are cut from the extruded rod. The end-faces of the cylinders are machined to optical quality employing a precision turning process with a diamond cutting tool. Indentation and uniaxial compression tests are performed on the same samples. To vary their thermodynamic state, some samples are annealed at 120 °C for 5 days in an air circulated oven and subsequently slowly air-cooled to room temperature.

Techniques

Indentation experiments are performed using a nano-indenter XP (MTS Nano-Instruments, Oak Ridge, Tennessee) under displacement control. The geometry of the tip was a flat-ended cone, chosen for the fact that the elastic and the plastic regions in the load-displacement curve can be clearly distinguished. Unfortunately this flat-tip geometry has the drawback that the force-displacement response is very sensitive to tip-sample misalignment. This problem is solved by sample re-alignment using a specially designed alignment tool. Details on the alignment procedure can be found elsewhere [112]. The geometry of the tip is characterized using SEM and AFM and the tip proves to have a diameter of 10 μm (Figure 4.3(a)), a top angle of 72 °, and an edge radius of 1 μm (Figure 4.3(b)).

Uniaxial compression tests are performed on a servo-hydraulic MTS Elastomer Testing System 810. The specimens are cylindrically shaped and compressed under true strain control, at constant true strain rates of 10^{-4} to 10^{-2} s $^{-1}$ between two parallel, flat steel plates. Friction between samples and plates is reduced by an empirically optimized method. Onto the sample ends a thin film of PTFE tape (3M 5480, PTFE skived film tape) is applied, and the contact area between steel and tape is lubricated using a 1:1 mixture of liquid soap and water. During the test no bulging of the sample is observed, indicating that friction is sufficiently reduced.

Uniaxial tests are performed on a Zwick Z010 tensile tester, at constant linear strain rates of 10^{-5} to 10^{-1} s $^{-1}$. Stress-strain curves are recorded and, where appropriate, true stresses are calculated assuming incompressible deformation.

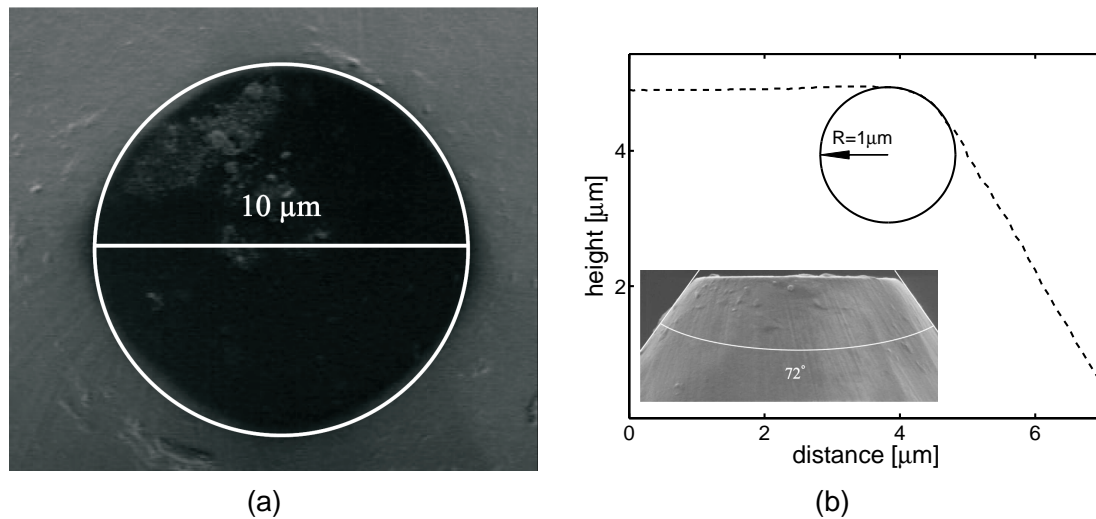


Figure 4.3: Characterization of the tip: (a) top view SEM picture; (b) side view SEM picture with tip profile obtained by AFM .

Numerical simulations

All axi-symmetric simulations are performed using MSC.Marc. The constitutive model as depicted in Chapters 2 and 3, is implemented in this package by means of the user-subroutine HYPELA2. The axi-symmetric mesh consists of 3303 linear quad4 elements, using full integration. The size of the mesh, which is 0.05 mm by 0.05 mm, is chosen such, that the edges do not influence the stress distribution. The indenter, a flat-ended cone with the geometrical specifications as determined by SEM and AFM (see Figure 4.3), is modelled as an impenetrable body where no friction between indenter and sample is taken into account.

The finite element mesh used for the simulation is presented in Figure 4.4. To exclude any mesh-dependence a stepwise element refinement is performed until the solution converged to a steady, mesh independent, result. In order to prevent excessive computation times the mesh refinement is restricted to areas of interest (see Figure 4.4).

4.4 Results and discussion

4.4.1 Thermorheologically simple behaviour: PC

Material characterization

In the case of PC, only a single molecular process contributes to the yield stress which implies that the viscosity function defined in Equation (2.8) can be applied. Besides the parameters in this expression, the model requires the determination of the strain-hardening modulus G_r , the

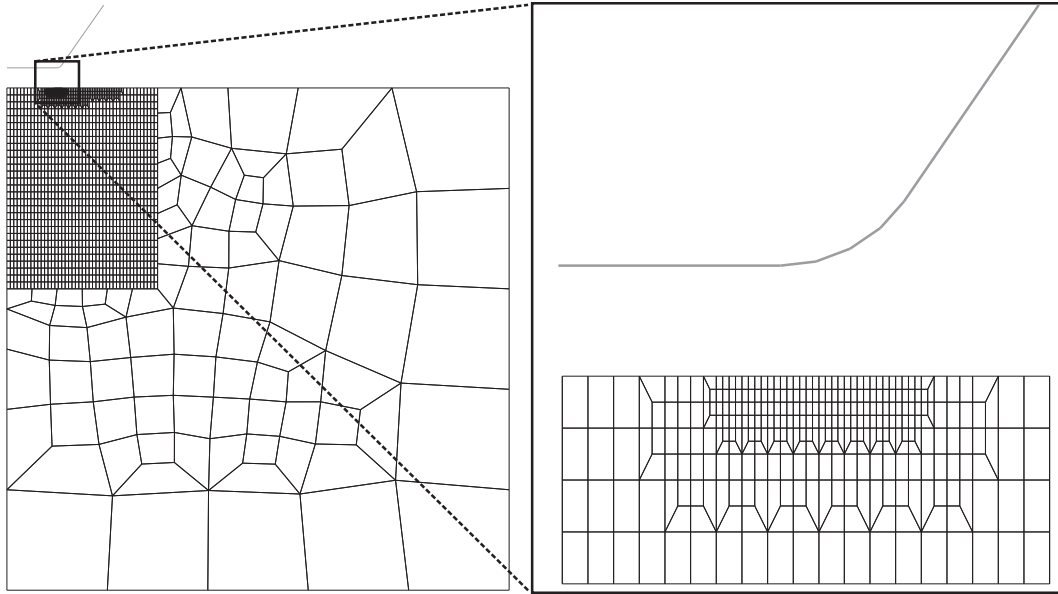


Figure 4.4: Mesh used to simulate indentation tests.

elastic shear moduli G_i and the bulk modulus κ . Most of these parameters can be determined by fitting the results of uniaxial compression tests at different strain rates. A proven strategy is to start by fitting the response of a rejuvenated material ($S_a = 0.0$) in the strain-hardening regime of the experimental curves, which yields the values for $\tau_0, \eta_{0,i,ref}$ and G_r . Next the softening can be added and r_0, r_1, r_2 and S_a can be determined.

To enable these model simulations, we first need the values of the elastic bulk modulus κ , the shear moduli G_i , and the pressure dependence μ . The value of κ is calculated from the values of the elastic modulus E and the Poisson ratio ν . The latter are determined in a uniaxial tensile test, yielding values of $E = 2250$ MPa for the elastic modulus and a value of $\nu = 0.4$ for the Poisson ratio [140]. Using the interrelation

$$\kappa = \frac{E}{3(1-2\nu)}, \quad (4.1)$$

a value of $\kappa = 3750$ MPa is found for the bulk modulus. In the multi-mode approach, the elastic shear moduli G_i and corresponding relaxation times are determined according to the procedure described in Section 2.4; the relaxation spectrum as tabulated in Table 2.2 is employed in all PC simulations.

An excellent method to obtain the pressure dependence is by performing experiments under superimposed hydrostatic pressure [39, 125, 129]. Therefore, μ is determined by numerically predicting the yield data obtained from compression tests at different true strain rates and, finally, from the tensile tests under superimposed hydrostatic pressure as reported by Christiansen et al. [39].

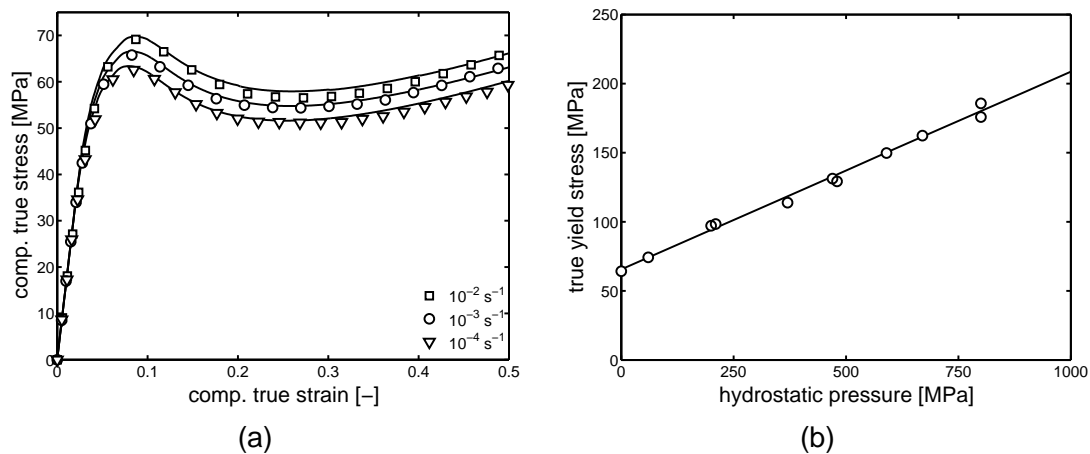


Figure 4.5: Multi-mode EGP-model; (a) simulated compression tests at different strain rates ($S_a = 27.0$); (b) yield stress versus superimposed hydrostatic pressure; model predictions (—) compared to experimental results; (○) results by Christiansen et al. [39] at a strain rate of $1.7 \cdot 10^{-4} \text{ s}^{-1}$ ($S_a = 34.0$).

Since both rejuvenation and ageing kinetics proved to be independent of the molecular weight of PC [85], the material parameters for PC tabulated in Tables 2.1 and 2.2 are employed accordingly. The only parameter which always needs to be determined, for every sample that experienced a different thermal history, is the parameter capturing the current thermodynamic state of the material, S_a . Its value is found by matching the experimental yield stress measured at one strain rate to that of a FEM-simulation; for the compression samples $S_a = 27.0$ and for the samples subjected to superimposed hydrostatic pressure, $S_a = 34.0$. Figure 4.5 shows that an excellent description is obtained.

Macro-scale simulations

Employing the same procedure but now matching the yield stresses for the as-received and annealed (48 hours at $120 \text{ }^\circ\text{C}$) sheet material by performing tensile tests on the milled tensile bars at a strain rate of 10^{-3} s^{-1} , results in $S_a = 31.7$ for the as-received material and $S_a = 39.0$ for the annealed material, see Figure 4.6. It is clear that an accurate, quantitative description is obtained. In the next section we will investigate the predictive capabilities of the model in micro-indentation.

Micro-scale simulations

In Figures 4.7(a) and 4.8 the experimental data of performing a flat-tip indentation test on the as-received material ($S_a = 31.7$) are compared with numerical simulations. The single-mode model [85] results are represented by the dashed line in Figure 4.7(a). A clear underestimation of the force response is observed, related to the too low modulus in the pre-yield regime of

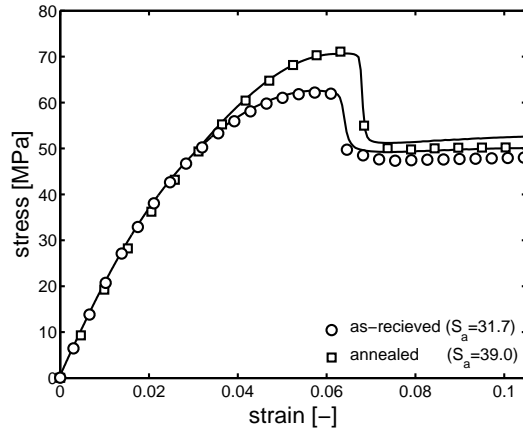


Figure 4.6: Experiments (open symbols) compared with the numerical simulation (—) on PC: tensile tests at a strain rate of 10^{-3} s^{-1} for two different thermal histories with for the as-received $S_a = 31.7$ (○) and for the annealed material $S_a = 39.0$ (□).

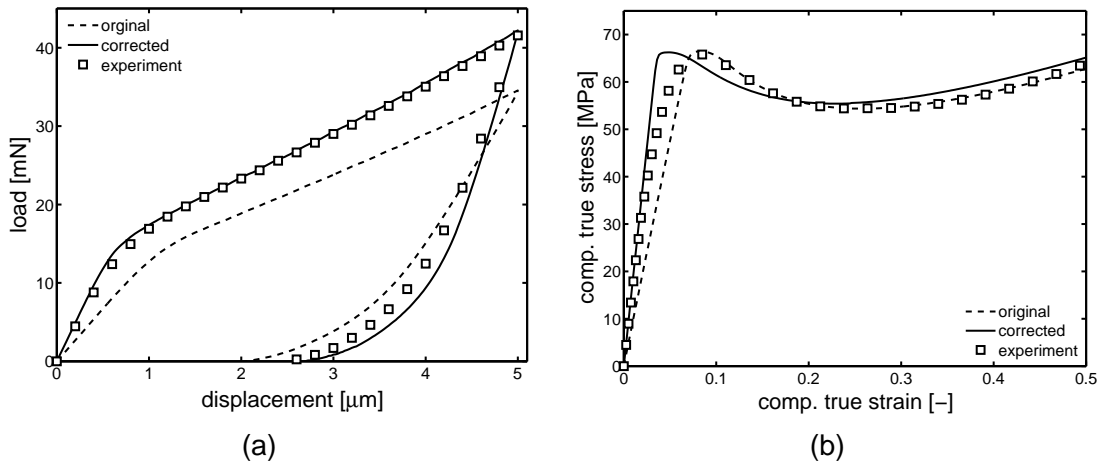


Figure 4.7: Flat-tip indentation modelled using the single-mode EGP-model (with $S_a = 31.7$) and showing the effect of the modulus correction; original ($G = 321 \text{ MPa}$) (---) and corrected ($G = 784 \text{ MPa}$) (—); (a) the two different moduli for the indentation tests (□); (b) simulated compression tests for two different values of the elastic modulus as compared to the experiments (□).

the intrinsic response, see Figure 4.7(b). Incorporation of a modulus correction, as suggested by van Breemen et al. [146], results in a good description of the loading path, the upper left part of the solid line in Figure 4.7(a), but creates an inconsistency in the parameter set since the prediction of the intrinsic stress-strain response requires a different parameter set, see Figure 4.7(b). In both figures the thermodynamic state of the material is the same, $S_a = 31.7$. Although the modulus correction proposed solves the loading path calculation, the unloading path is still not well predicted, see the lower right part of the solid line in Figure 4.7(a). For clarity in Figure 4.7, only a single strain rate (10^{-3} s^{-1}) and a single indentation speed of $50 \text{ nm}\cdot\text{s}^{-1}$ are depicted, but the situation only worsens when different rates are applied.

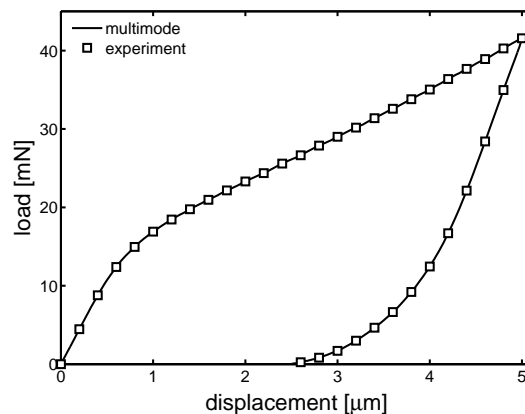


Figure 4.8: Flat-tip indentation experiment, where the solid line (–) is the multi-mode EGP-model prediction $S_a = 31.7$.

The simulation result with the multi-mode model, employing the same value for S_a is given in Figure 4.8, that now clearly shows a quantitative prediction of the complete (loading and unloading) flat-tip indentation experiment.

In Figure 4.9(d) a characteristic loading curve of an indentation measurement is shown, and three points are marked: a, b and c. Figures 4.9(a) - 4.9(c) show the development of the plastic deformation under the tip in these three points. The plastic deformation starts at the edge of the indenter, as can be seen in Figure 4.9(a), and grows in the form of a hemisphere towards the symmetry axis. This is a result of the fact that stress localizes at the edge of the indenter. Around point b, see Figure 4.9(b), the plastic deformation zone concludes the formation of the hemisphere. From point b on, see Figure 4.9(c), this hemisphere then expands in thickness. These results correspond well to experimental observations made by others [96]. Figure 4.10(a) shows the results of indentation tests for two different thermodynamic states, $S_a = 31.7$ for the as-received material and $S_a = 39.0$ for the annealed sample, compare Figure 4.6, while Figure 4.10(b) shows the influence of the indentation speed using a sheet of polycarbonate which was annealed at 120 °C for only a few hours ($S_a = 34.0$), rather than the 48 hours of the samples in Figure 4.10(a) ($S_a = 39.0$). Experimental data at three different indentation rates ($5 \text{ nm}\cdot\text{s}^{-1}$, $50 \text{ nm}\cdot\text{s}^{-1}$ and $200 \text{ nm}\cdot\text{s}^{-1}$) are captured accurately and, moreover, we can conclude that a correct determination of the thermodynamic state of the material, out of a single indentation test, is not affected by the indentation speed applied. The Figures 4.5(a), 4.8, and 4.10 distinctly show that the multi-mode EGP-model is able to predict the intrinsic stress-strain response and the indentation results at varying indentation speeds and thermodynamic states. The same parameter set, as presented in the Tables 2.1 and 2.2, is used, where the reference spectrum from Table 2.2 is shifted to the specific thermodynamic state of the material.

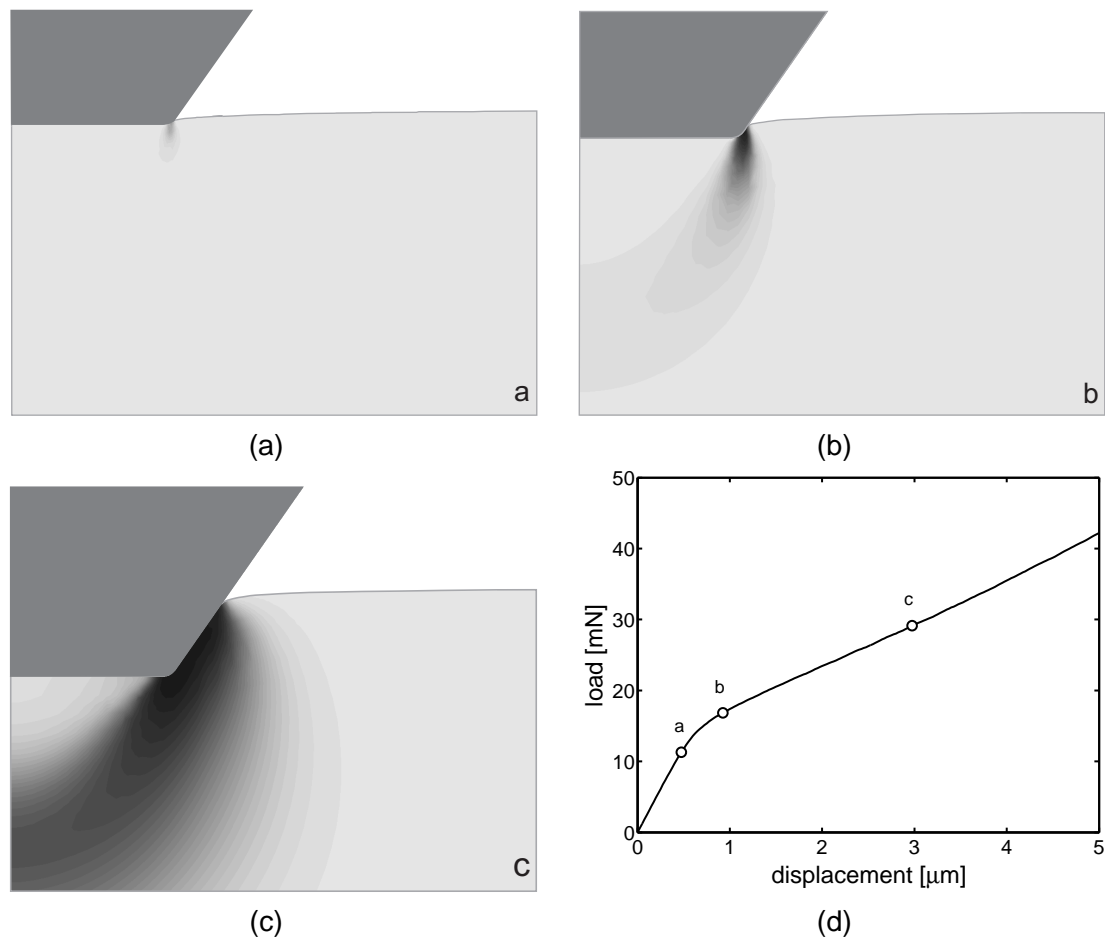


Figure 4.9: Simulation of the development of plastic deformation at different indentation depths for PC: (a) at 460 nm ; (b) 965 nm; (c) 3 μm ; (d) here the points a, b and c indicate the load-displacement response for the different stages of plastic deformation.

4.4.2 Thermorheologically complex behaviour: PMMA

Material characterization

In the case of PMMA, there are two molecular processes that contribute to the yield stress which implies that the viscosity functions defined in Equation (3.36) must be applied. This means that, besides the parameters already discussed in the previous section, we also have to determine the values of $\tau_{0,\beta}$ and $\eta_{0,\beta,j,ref}$. For the characterization we make use of the fact that the β -contribution is only present at high strain rates and, therefore, that the stress-strain response in the low strain-rate range is determined by the α -process only. As a consequence, we can use the same characterization strategy at low strain rates as employed in Chapter 2 for PC. For the elastic properties of PMMA we use a bulk modulus κ of 3 GPa [56]. Since tacticity greatly influences the intrinsic response of PMMA, the spectrum determined in Chapter 3 for Plexiglas 8H (Table 3.3) cannot be employed. Instead the appropriate values of the shear moduli for the α -process are determined again, now for this grade, according to the procedure

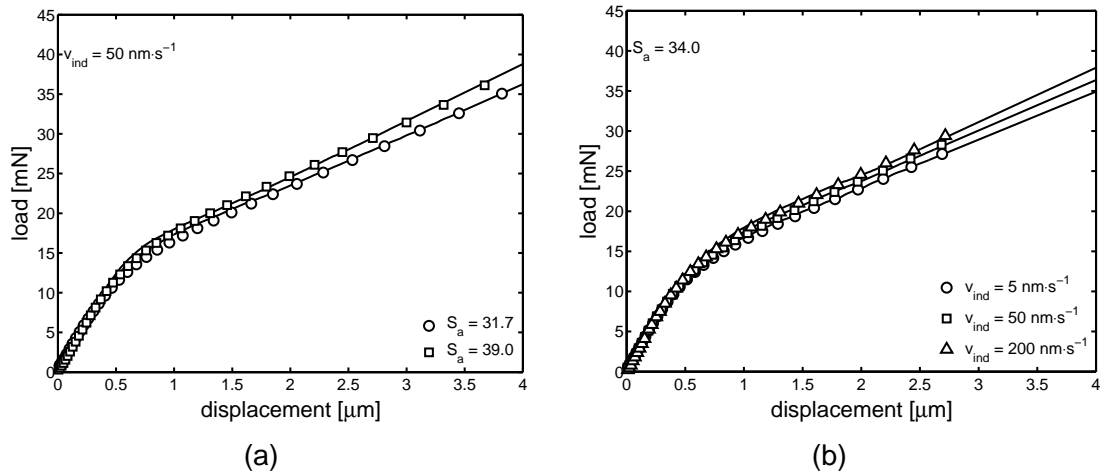


Figure 4.10: Flat-tip indentation experiments (open symbols) compared with the numerical prediction (–): (a) as-received ($S_a = 31.7$) (\circ) and for annealed ($S_a = 39.0$) (\square) PC at an indentation speed of $50 \text{ nm}\cdot\text{s}^{-1}$ and (b) for speeds of $5 \text{ nm}\cdot\text{s}^{-1}$ (\circ), $50 \text{ nm}\cdot\text{s}^{-1}$ (\square) and $200 \text{ nm}\cdot\text{s}^{-1}$ (\triangle) on annealed PC sheet ($S_a = 34.0$).

described in detail in Chapter 3. The values as tabulated in Table 4.1 result. The complete

Table 4.1: Reference spectrum for the α -process of Plexiglas ICI.

mode	$\eta_{0,\alpha,i,ref} [\text{MPa}\cdot\text{s}]$	$G_i [\text{MPa}]$	$\lambda_i [\text{s}]$
1	$1.72\cdot 10^6$	$1.25\cdot 10^2$	$1.38\cdot 10^4$
2	$4.87\cdot 10^6$	$4.32\cdot 10^2$	$1.13\cdot 10^4$
3	$1.09\cdot 10^5$	$8.47\cdot 10^1$	$1.29\cdot 10^3$
4	$2.01\cdot 10^4$	$6.22\cdot 10^1$	$3.23\cdot 10^2$
5	$3.01\cdot 10^3$	$5.49\cdot 10^1$	$5.49\cdot 10^1$

data set, used for the predictions in Figure 4.11, is tabulated in Table 4.2. The corresponding S_a -value is determined to be 7.4.

To obtain the value of the pressure-dependence parameter μ , we use a method inspired by the work of Bardia and Narasimhan [7], who employed a spherical indentation test to characterize the pressure sensitivity index of the Drucker-Prager constitutive model. Here we follow a similar route. Since the compression tests and the indentation tests are performed on the same sample, the S_a value is identical in both cases. The only unknown parameter is therefore the pressure dependence μ . Similar to the approach for polycarbonate we generate different parameter sets by fitting the compression data for different values of μ . Each set describes the compressive stress-strain curves equally well (Figure 4.11(a)), that are, therefore, not pressure dependent. Using the same data sets we subsequently predict the load-deformation curve for an indentation rate of $5 \text{ nm}\cdot\text{s}^{-1}$ (see Figure 4.11(b)) to find that a value of $\mu = 0.13$ gives the best agreement with the experiment.

Table 4.2: input parameters for PMMA.

$G_{\alpha,tot}$ [MPa]	$\eta_{0,\alpha,ref}$ [MPa·s]	V_{α}^* [nm ³]	$S_{a,\alpha}$ [-]	$r_{0,\alpha}$ [-]	$r_{1,\alpha}$ [-]	$r_{2,\alpha}$ [-]
759	$2.3 \cdot 10^7$	1.44	7.4	0.965	5.0	-3.5

$G_{\beta,tot}$ [MPa]	$\eta_{0,\beta,ref}$ [MPa·s]	V_{β}^* [nm ³]	$S_{a,\beta}$ [-]	$r_{0,\beta}$ [-]	$r_{1,\beta}$ [-]	$r_{2,\beta}$ [-]
800	$3.0 \cdot 10^{-1}$	1.97	7.4	0.965	30.0	-4.5

G_r [MPa]	κ [MPa]	μ_{α} [-]	μ_{β} [-]
26.0	$3.0 \cdot 10^3$	0.13	0.13

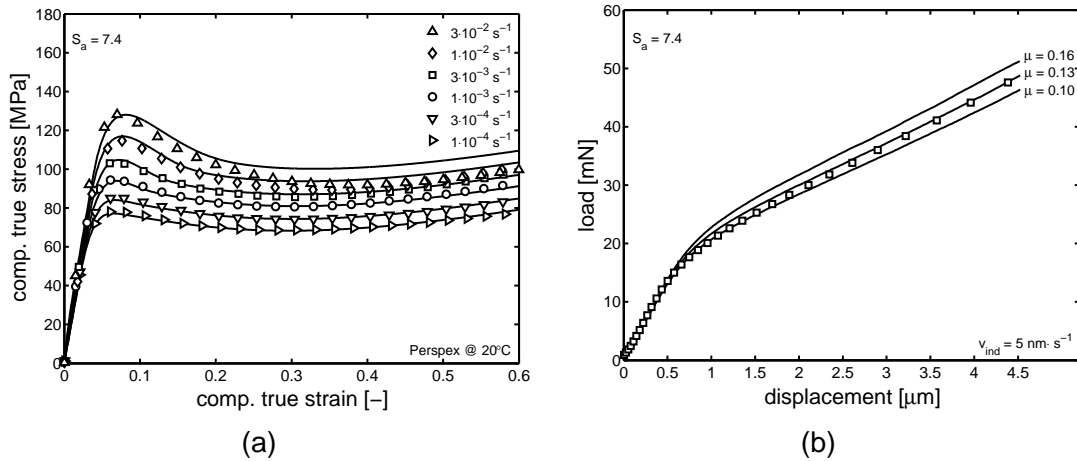


Figure 4.11: Experiments (open symbols) compared to numerical simulations (–) for: (a) compression tests (\circ) performed on PMMA at different strain rates and; (b) flat-tip indentation performed at $5 \text{ nm}\cdot\text{s}^{-1}$ with different values for μ ; a best fit is obtained at $\mu = 0.13$ (\square).

Finally, indentation tests are performed at indentation rates of $5 \text{ nm}\cdot\text{s}^{-1}$, $10 \text{ nm}\cdot\text{s}^{-1}$, $20 \text{ nm}\cdot\text{s}^{-1}$ and $40 \text{ nm}\cdot\text{s}^{-1}$. The results are compared to numerical predictions in Figure 4.12(a), and predictions are in excellent agreement with the pronounced rate-dependence observed in the experimental force-displacement curves. To demonstrate the presence of a β -contribution in the indentation response, we performed simulations of indentation tests at rates of $0.1 \text{ nm}\cdot\text{s}^{-1}$ and $40 \text{ nm}\cdot\text{s}^{-1}$ with, as well as without a β -contribution. Thus employing the multi-mode EGP model (see Chapter 2; dashed lines in Figure 4.12(b)) and the multi-mode-multi-process EGP-model (see Chapter 3; solid lines in Figure 4.12(b)). Clearly at a low indentation rate ($0.1 \text{ nm}\cdot\text{s}^{-1}$) the β -contribution is negligible, whereas at higher rates a significant contribution is noticeable.

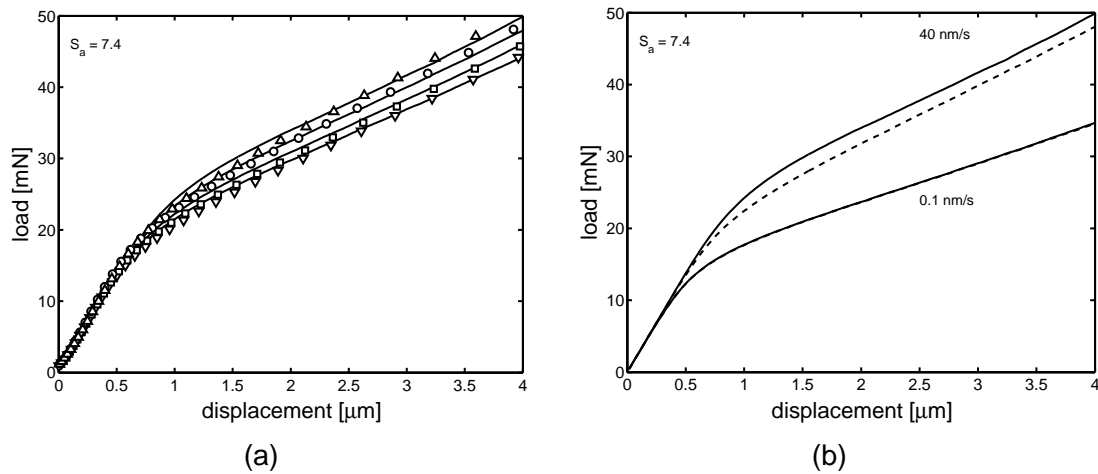


Figure 4.12: (a) Flat-tip indentation performed on PMMA at a speed of $5 \text{ nm}\cdot\text{s}^{-1}$ (∇), $10 \text{ nm}\cdot\text{s}^{-1}$ (\square), $20 \text{ nm}\cdot\text{s}^{-1}$ (\circ), $40 \text{ nm}\cdot\text{s}^{-1}$ (\triangle) compared with the numerical simulations (–) and (b) numerical simulation performed using the model which takes into account the α -contribution (–) only and the α - and β -contributions (–) at two different speeds $0.1 \text{ nm}\cdot\text{s}^{-1}$ and $40 \text{ nm}\cdot\text{s}^{-1}$.

4.5 Conclusion

In the plastic regime, glassy polymers possess a rather complex intrinsic behaviour, with a pronounced pressure- and rate-dependence of the yield stress as well as a post yield region displaying both strain softening and strain hardening. We employ a state-of-the-art constitutive model, previously developed in our group, which describes this intrinsic behaviour, to numerically predict the indentation response. In the model, a single parameter, the state parameter S_a , is used to uniquely determine the initial yield stress of the material, and capture all variations in its thermal history. We demonstrate that this model can capture the rate, and history dependence of PC and PMMA on both the macroscopic and microscopic scale. The excellent accuracy of the description also creates the possibility to accurately extract the state parameter S_a directly from micro-indentation experiments. This offers interesting possibilities with respect to quality control of load-bearing polymer products. Moreover, it is found that the pressure dependence of the yield stress can also be obtained by combining indentation tests and compression tests on the same samples.

Single-asperity sliding friction¹

Abstract

Generally it is understood that the friction force is an additive composition of an adhesion- and a deformation-related component, suggesting that components operate and contribute independently. In an experimental set-up a decomposition of these components is impossible. However by combining experiments with numerical (FEM) simulations, a decoupled analysis is made possible. Simulations with no adhesive interaction between tip and polymer show almost no influence of sliding velocity on friction force, whereas experiments show a significant influence. In case of an additive decomposition, this would imply a time-dependency of the adhesive component. By inclusion of the Amontons-Coulomb friction law (1781), which creates an interaction between tip and polymer, it is demonstrated that an increase of the adhesive component strongly influences the contribution of the deformation related component, by the formation of a bow wave in front of the sliding tip. This implies that the suggested additive decomposition is not applicable and the large macroscopic deformation response proves to be the result of small changes in local processes. As a result, relations between intrinsic mechanical properties and frictional properties are established.

¹reproduced from: L.C.A. van Breemen, L.E. Govaert and H.E.H. Meijer, Friction in a single-asperity contact: relation to intrinsic mechanical properties of glassy polymers, Tribology International, *submitted*

5.1 Introduction

Polymers display an excellent strength-to-weight ratio and are, therefore, to a great extent applied also in structural applications. In combination with their excellent tribological properties [161] they are moreover favoured above their metal counterparts in applications where friction and wear are important, like e.g. the cups in hip-joints and artificial knees, in bearings, and in gears. The correlation between intrinsic polymer properties and frictional behaviour is blurred by measurements with too many variables. The complexity is underlined by the large scatter of data on the response of polymers to single-asperity scratching, e.g. the dependence on scratch load, temperature, tip geometry, and speed [8, 18, 23, 24, 27–29, 154, 160], and the amount and type of fillers or additives [40, 41, 53, 57, 87].

The earliest model trying to capture frictional responses dates back to the pioneering work of Bowden and Tabor [19, 135]. In their approach it is presumed that the friction force can be additively decomposed into an adhesion- and a deformation-related component. Confirmation of this hypothesis was demonstrated by experiments on rubbers with specific boundary conditions, e.g. lubrication of the interface [34, 63] or application of rolling friction [97, 134]. With lubrication of two contacting surfaces the adhesion component can be neglected and, as a result, the deformation related component can be studied individually. To prevent the contribution of the lubricant in the shear layer, rolling friction was studied, i.e. rolling of a hard asperity over the rubber surface. Grosch [67], Ludema and Tabor [97] and Bueche and Flom [34] demonstrated that the frictional behaviour of a rubber, sliding at various velocities and temperature on a given surface, can entirely be described by a single master curve, constructed by application of the WLF transform. Similar observations were also reported by McLaren and Tabor [100] for polymers below their glass transition temperature. This suggests that there is a pronounced influence of the visco-elastic properties of the polymer on the frictional response. In the case of lubricated or rolling friction the comparison is most successful [26]. These observations indicate that capturing visco-elastic properties is of utmost importance.

To study mechanical properties on a small scale, usually an indentation test is performed, where a single-asperity contact (a well-defined indenter) is pressed into a substrate. In particular for the elastic modulus, quantitative analytical methods are available [74, 110], and with the aid of the elastic-visco-elastic correspondence principle these methods are also applicable to the visco-elastic properties [37, 38, 42, 43, 88]. Less straightforward is the analysis of the large strain mechanical properties, and e.g. for something trivial as the yield strength only empirical scaling laws are available [78, 79, 96, 135].

For non-linear contact problems, the rise of the Finite Element Method (FEM) opened up new possibilities. With appropriate finite-strain constitutive relations a detailed analysis of local deformation and stress fields became feasible. An example is the work in Larsson's

group on Vickers [55] and Berkovich [89] indentation of elasto-plastic materials. In the case of polymeric materials, the analysis of such a contact problem is complicated. Crucial in the analyses proved the application of a quantitative constitutive model capturing the intrinsic polymer properties [2, 146, 148], see also Chapter 4.

The next challenge is the evaluation of the single-asperity sliding friction test, commonly referred to as scratch test. This test is extensively used for a wide range of surface mechanical properties, such as relative hardness of materials and modelling of wear [48, 77, 131, 132]. The friction (and wear) behaviour of polycarbonate has been the subject of study [23, 28, 29, 131], however mostly experimental. Similar to indentation, the FEM technique was employed to analyse the complex material response as observed in scratch experiments [30, 31, 50, 92]. The group of Schirrer [114–118] recently tried to quantify experimental data on PMMA. The experimental set-up developed allows the in-situ determination of the real contact area [54]. The problem was analysed quasi-statically, which implies that there is no time-dependence and thus no dependence on strain rate or sliding velocity; this is a strong assumption. The constitutive relation employed does not capture the large strain mechanics, and neither correctly captures the visco-elastic pre-yield behaviour, as experimentally observed in polymer glasses. However, with this simple approach a qualitative relation between contact area and simulated friction coefficient could be established. An analogous approach by Bucaille et al. [31], employing the same constitutive relation, showed that a correlation between strain hardening and observed frictional hardness could be achieved. Still, as also pointed out by Briscoe and Sinha [25], at present, there are no analytical or computational models available to quantitatively couple intrinsic material properties to the observed response. Therefore there is a need for an appropriate finite-strain constitutive relation that accurately captures these intrinsic deformation characteristics.

In the present study FEM analyses are employed to investigate the interaction between indenter and polymer using the quantitative constitutive model derived in Chapters 2 and 3. The choice for glassy polymers as a model system is only because they represent a well-characterized class of polymers that allow quantitative predictions, also in contact mechanics, and therefore clearly not motivated by their relevance in low friction applications. The interaction between tip and polymer is separately studied by the incorporation of existing friction models. The challenge in the experiments proved to be in the development of reproducible sliding friction tests, characterized by minimization of the amount of variables. Experiments are compared with FEM simulations.

The previous Chapters 2 and 3 revealed some drawbacks of the existing EGP-model which had to be removed. The pre-yield regime itself is non-linear visco-elastic and thus correct modelling thereof is important in all simulations where non-homogeneous deformation is applied, like e.g. in indentation or sliding friction tests. The pre-yield region was in the original EGP-model described with one mode, thus as a compressible linear elastic solid. As a

result, details of indentation, and of unloading, were not described quantitatively. The rather straightforward solution was to extend the existing model to include a spectrum of relaxation times in the pre-yield regime, via use of the multi-mode approach worked out in Chapter 2. The improved model indeed quantitatively predicts the indentation response in polycarbonate, see Chapter 4, using the flat-punch indenter geometry [147]. The only adjustable parameter in the model is the parameter representing the thermodynamic state of the material, but as demonstrated in [46, 61] once the details of the formation history of the polymer product are known, this state can directly be computed.

The ability to quantitatively capture indentation phenomena with the constitutive framework presented, allows the assessment of the more complex single-asperity sliding friction experiments. Although decomposition in independent contributions, that is adhesion and deformation, is impossible to verify in an experimental set-up, it can be conveniently studied by employing a numerical (FEM-based) approach. The hybrid numerical/experimental approach applied in this thesis proves to be successful in isolating the individual influences and coupling the polymer's intrinsic mechanical properties to the experimentally determined friction forces.

5.2 Experimental

Sample preparation

The material used in this study is a commercial grade of polycarbonate, Lexan 101R, Sabic Innovative Plastics (Bergen op Zoom, the Netherlands).

The scratch samples are prepared from compression moulded plaques ($100 \times 50 \times 10 \text{ mm}^3$). During compression moulding the dried granulate is heated in a mould for 15 minutes at $250 \text{ }^\circ\text{C}$ and next compressed up to 300 kN in 5 subsequent intervals of 5 minutes, while after each step degassing is allowed by releasing the force. Finally the mould is placed in a water-cooled cold press and quenched to room temperature ($20 \text{ }^\circ\text{C}$) under a moderate force of 100 kN. The mean surface roughness (R_m) of the plaques is in the order of $10 \text{ }\mu\text{m}$, which is of the same order as the tip-radius in the scratch set-up. To consider the surface of the polymer sample flat, as compared to the indenter tip, we at least need samples with a roughness, R_m , in the order of 10 nm. Therefore a procedure is developed by compressing the samples against an optically flat steel plate ($R_m \approx 5 \text{ nm}$).

The plaques are cut into smaller pieces ($50 \times 50 \times 10 \text{ mm}^3$), subsequently a single piece is placed on the preheated ($190 \text{ }^\circ\text{C}$) optically flat steel plate and placed in an oven for 30 minutes at $190 \text{ }^\circ\text{C}$, which is approximately $40 \text{ }^\circ\text{C}$ above the T_g of PC. The now rubbery PC-sample is, again, placed in the hot-press, set at a temperature of $200 \text{ }^\circ\text{C}$, and compressed with

a force of 300 kN, kept constant for 15 minutes before placing the sample in the cold press. To obtain samples with uniform thickness of 3 mm, spacers are placed alongside the steel plate during these compression steps. The compression procedure introduces stresses in the surface layer, where the single-asperity scratch tests are performed. Because experiments are compared to simulations, where uniform material properties and a stress-free initial condition are assumed, removing them is essential. The procedure followed is to place the samples once more in the oven, again at 190 °C for 30 minutes, and air-cooling them thereafter to room temperature. The surface roughness is checked with a profilometer (Sensofar®) and proved to be $R_m \approx 20$ nm, see Figure 5.1.

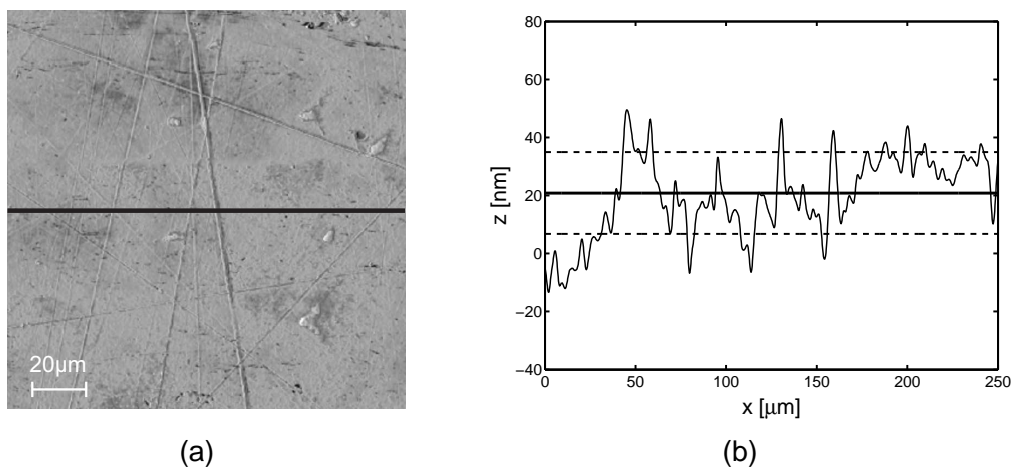


Figure 5.1: (a) Surface profile obtained from the Sensofar profilometer; the solid line (–) is the location where the mean surface roughness is determined; (b) surface roughness of the Lexan 101R sample, where the horizontal solid line (–) is the mean surface $R_m \approx 20$ nm and the dashed lines (– –) are the corresponding standard deviations.

Techniques

Single-asperity scratch experiments are performed using a standard nano-indenter XP (MTS Nano-Instruments, Oak Ridge, Tennessee) extended with the lateral force option. The normal load applied is force controlled, whereas the sliding velocity is under displacement control. The two tip geometries used, which are characterized by the Sensofar and SEM, are round tips (see Figure 5.2) both have a top angle (α) of 90°, but different top-radii (r_{tip}), 10 μm and 50 μm respectively. To accomplish a perfect perpendicular position of the tip versus the sample surface and arrive at a parallel sliding path, a specially designed alignment tool is employed, see also Chapter 1. Details on the alignment tool can be found elsewhere [112].

Choice of tip geometry

The nano-indenter can be equipped with different indenter tips, ranging from the commonly used Berkovich tip to the round tip, see Figure 5.2. The Berkovich tip has sharp edges,

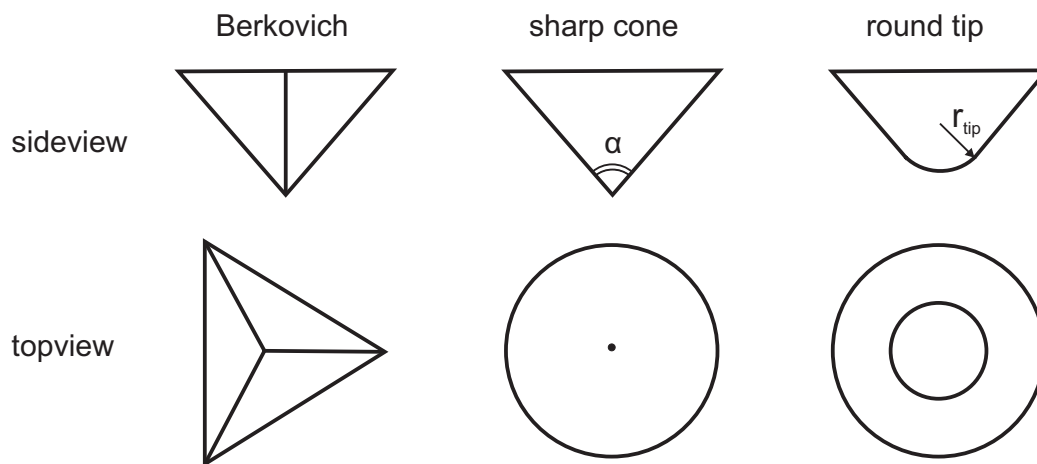


Figure 5.2: Different indenter tips frequently used in a single-asperity scratch set-up, where α is the top angle and r_{tip} is the tip-radius.

resulting in complex deformation fields underneath the indenter tip; therefore this tip is not the obvious choice. Also in FEM-simulations convergence problems as well as the need of excessive mesh-refinements are expected due to the large gradients in the proximity of the indenter edges. The most simple geometry is that of the cone-shaped indenter, with only one parameter, the top angle (α). However, from a FEM point of view also this tip is not the evident choice since convergence problems are anticipated around the sharp indenter tip, leading to singularities. The only other tip option available is the round tip. The shape of this type of tip can be manipulated by changing the top angle α or the top radius r_{tip} . The advantage of this tip in a FEM-simulation is that there are no singularities expected around the top of the tip since the mesh can 'flow' underneath the tip. Moreover there are no sharp edges present, which results in less pronounced mesh refinements needed and far better convergence due to the local smaller gradients. Hence the round tip is employed.

Effect of sample tilt

Misalignment is defined as the situation where the sample surface is not perpendicular to the symmetry axis of the indenter tip. Two types of misalignment exist, the first is the misalignment of the sample relatively to the tip, the other misalignment in mounting of the indenter tip, which results in an off-axis loading. Presuming that the tip is well-mounted in the machine, only the first misalignment option is considered. Figure 5.3 illustrates the exaggerated effect of

sample-tip misalignment in a scratch experiment, resulting in completely different deformation responses. To prevent this, a special alignment tool [112] is utilized. Apart from aiming

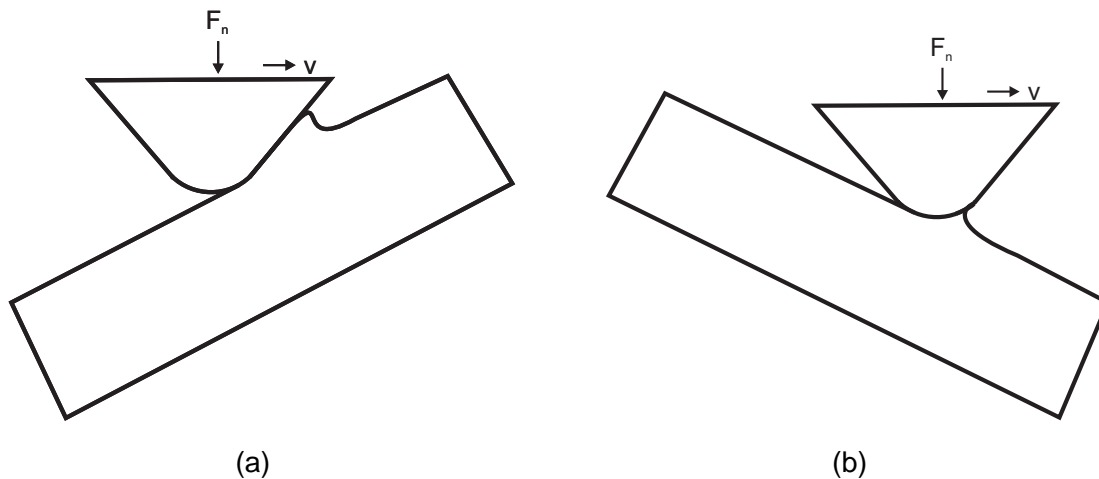


Figure 5.3: Exaggerated effect of sample-tip misalignment, resulting in different deformation responses.

at reproducibility in the experiments, alignment is also required to arrive at a quantitative comparison between simulation and experiment.

The nano-indenter is extended with the lateral force option, so in-plane movement is possible. Therefore a different, and much simpler and less time-consuming, alignment procedure can be followed as compared to the procedure described by Pelletier et al. [112] for flat-tip indentation. They had to search for maximum contact stiffness, since the contact stiffness is the largest when the tip and sample are correctly aligned. The sample-tilt stage allows rotation along two perpendicular axes, which are in plane with the sample surface. Each axis is allowed to rotate to a total angle of 1.4° via rotation of the attached screw-micrometers. The procedure followed is the same for both rotation axes. First the sample is mounted in the alignment tool and the neutral position of the tool is set. Subsequently a scratch parallel to one of the rotation axis, with a length of 1 mm, a normal load of $50 \mu\text{N}$, and sliding velocity of $10 \mu\text{m} \cdot \text{s}^{-1}$, is made. The sample tilt is determined from the raw displacement into the surface signal; the sample rotation required is calculated via elementary goniometric relations and applied accordingly. Completion of this procedure of both rotation axis leaves a perfectly aligned sample-tip combination.

Dependence on sliding velocity

A typical scratch set-up has a number of characteristic parameters, the type of indenter tip mounted, and the normal load (F_n), and sliding velocity (v) applied. The last two operational

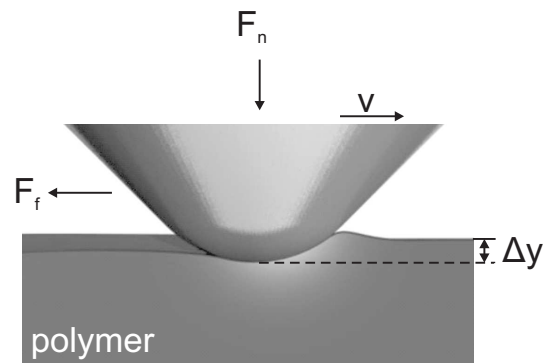


Figure 5.4: The single-asperity scratch set-up with characteristic in- and output parameters.

parameters can be chosen constant or increasing or decreasing in magnitude, which results in a difference in deformation of the material volume. The penetration into the surface (Δy) and the lateral force (F_f) are measured, see Figure 5.4. To reduce the influence of indenter-substrate effects, which are not related to intrinsic polymer properties, an inert diamond $50\ \mu\text{m}$ round tip is selected; the other tip, with a top radius of $10\ \mu\text{m}$, will be considered later.

Since polymers show a distinct dependence on strain rate and temperature (see Chapters 2 and 3), we start by choosing sliding velocity and temperature constant in each experiment. To eliminate the influence of any transients, and acquire a steady state, the normal force applied is also taken constant. The load is applied in 10 seconds, thus without sliding, which is in principle a normal indentation as discussed elaborately in Chapter 4.

Figure 5.5 illustrates the typical response observed when the described loading protocol is executed. All lines representing measurements are the average of 5 consecutive measurements with identical input parameters. Figure 5.5(a) displays the penetration into the surface; three points of interest are present and marked with the numbers I, II, and III, corresponding to the graphical representation of the observed macroscopic response in Figure 5.5(c). The indentation (I) results in an indentation depth marked by the dashed line. Since this is a force controlled experiment, the contact surface generated during indentation is reduced with the onset of sliding (I to II), resulting in sink-in of the tip into the polymer (II). During sliding from point I to III, a steady state is achieved and a bow wave is observed in front of the tip and, as a result, a contact area is generated which remains constant for the rest of the sliding procedure. The corresponding lateral force is displayed in Figure 5.5(b). Only steady state data are used in the analyses.

Results of experiments under identical conditions, but now for 4 different sliding velocities, ranging from $0.1\ \mu\text{m}\cdot\text{s}^{-1}$ to $100\ \mu\text{m}\cdot\text{s}^{-1}$, are shown in Figure 5.6. Both the penetration depth into the surface and the lateral force display a dependency on sliding velocity. The rationale is given by the fact that polymers intrinsically display a pronounced strain-rate dependence, and

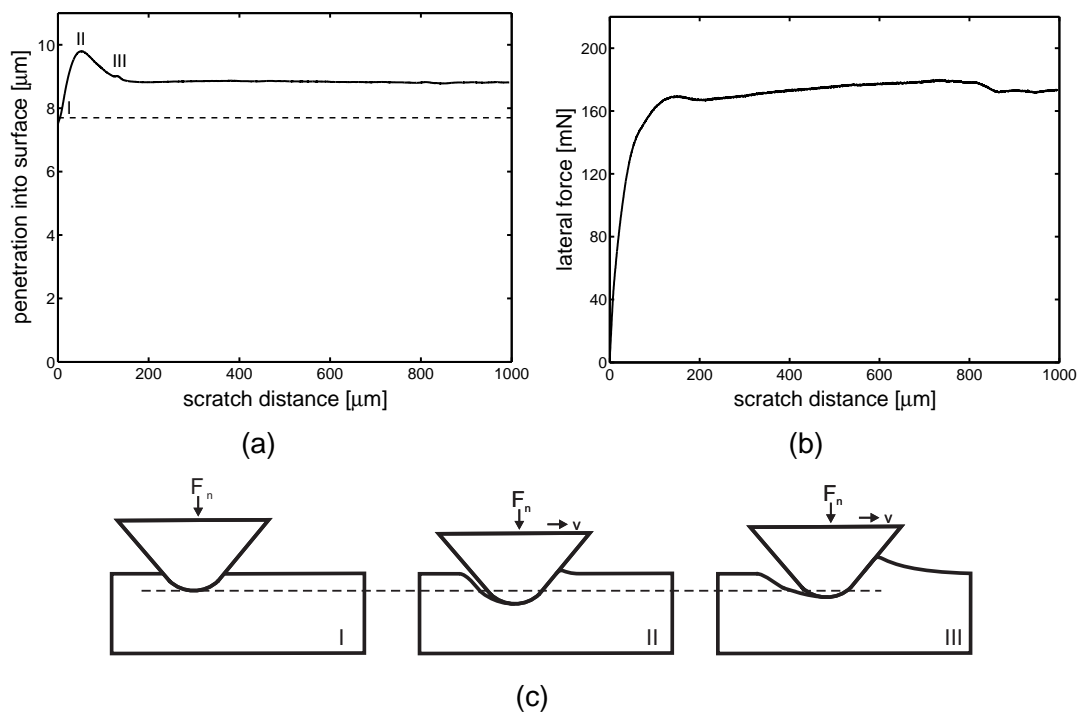


Figure 5.5: Measured response of a single-asperity scratch experiment with a constant normal load of 300 mN and a sliding velocity of $0.1 \mu\text{m}\cdot\text{s}^{-1}$; (a) penetration into the surface versus sliding distance, (b) the lateral friction force versus sliding distance and (c) graphical representation of the observed macroscopic response; the numbers I, II, and III, correspond to the same numbers as in (a), where the dashed line (- -) is the depth after the initial indentation step.

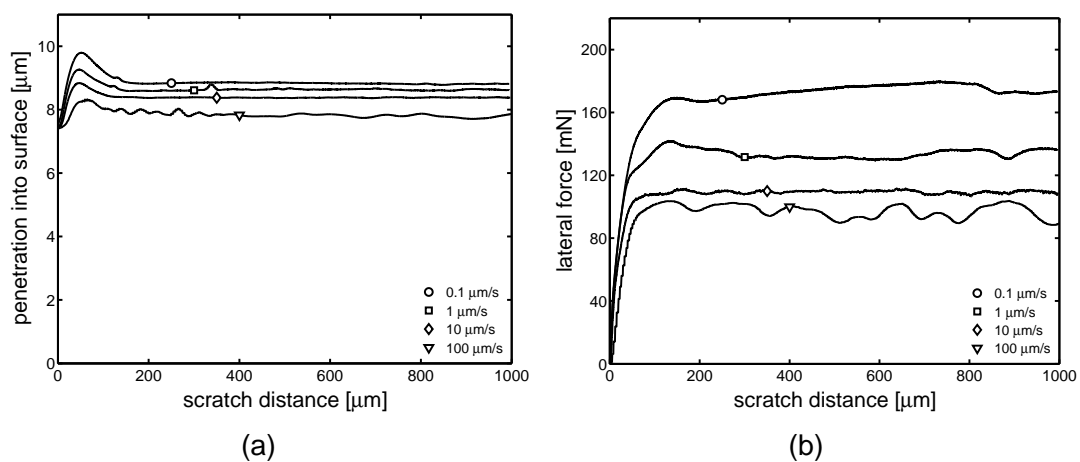


Figure 5.6: Response of Lexan 101R at 4 different sliding velocities with a $50 \mu\text{m}$ tip; (a) penetration into the surface versus sliding distance and (b) friction force versus sliding distance.

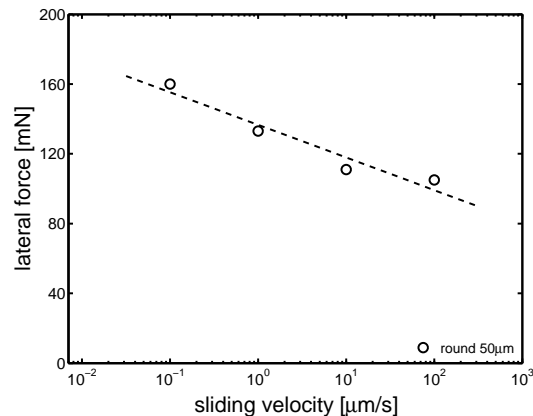


Figure 5.7: Response of Lexan 101R at 4 different sliding velocities; friction force versus logarithm of sliding velocity, the dashed line (- -) is a first order fit of the experimental data and plotted as a guide to the eye.

thus a dependence on sliding velocity. With increasing sliding velocity the material displays more resistance to deformation and, as a consequence, the tip penetrates less into the surface. A decrease in contact area between tip and polymer results. The lateral force, which is directly related to this contact area, therefore also decreases.

Since the yield stress of PC shows a linear dependence on the logarithm of the strain rate applied (see Chapter 2), the measured lateral force is plotted versus the logarithm of sliding velocity applied, see Figure 5.7. Remarkably we find that the lateral force also displays a linear relation with the logarithm of the sliding velocity.

5.3 Modelling

Constitutive model

The constitutive model employed is the EGP-model (see Chapters 2 and 3, and Klompen et al. [85]). It is based on an additive decomposition of the total stress into a driving and a hardening stress. The hardening stress is modelled with a neo-Hookean spring and accounts for the stress contribution of the orienting molecular network. The driving stress is additively decomposed into a hydrostatic and deviatoric part and is related to the intermolecular interactions. The deviatoric part (σ_s^d) is coupled to the plastic deformation rate tensor (\mathbf{D}_p) via a non-Newtonian flow rule. The viscosity depends strongly on equivalent stress ($\bar{\tau}$), temperature (T), hydrostatic pressure (p) and thermodynamic state (S_a) of the material,

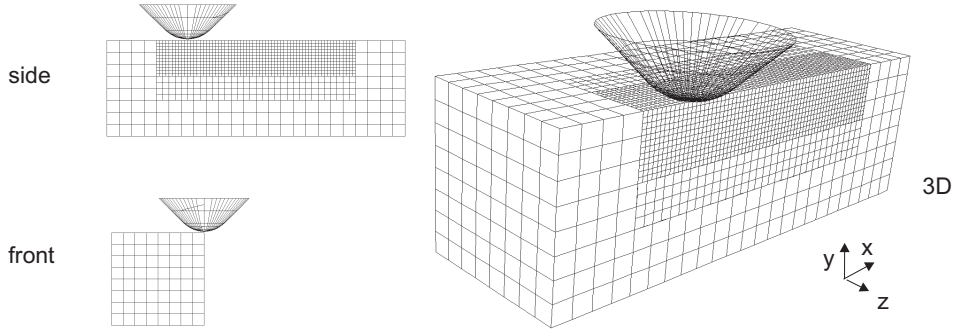


Figure 5.8: Mesh for the 50 μm tip.

according to:

$$\mathbf{D}_{p,i} = \frac{\sigma_s^d}{2\eta_i(\bar{\tau}, T, p, S_a)} \quad , \text{where} \quad \eta_i = \eta_{0,i,ref}(T) \frac{\bar{\tau}/\tau_0}{\sinh(\bar{\tau}/\tau_0)} \exp\left(\frac{\mu p}{\tau_0}\right) \exp\left(S_a \cdot R(\bar{\gamma}_p)\right). \quad (5.1)$$

The model is implemented in the FEM package MSC.Marc.

In the previous chapters it has been shown that the only unknown parameter in the model is the parameter capturing the thermodynamic state of the material (S_a). It has also been shown that its value can directly be determined from an indentation test, by matching the load-displacement response to the simulation [146]. Since every sliding friction experiment starts with an initial indentation its value can easily be determined.

Finite element mesh

Since the problem analysed is symmetric in sliding direction, only half the scratch surface is meshed. The mesh for the 50 μm tip consists of 33904 linear brick elements (hex 8, element number 7, full integration), see Figure 5.8 and is dimensioned $0.16 \times 0.16 \times 0.48 \text{ mm}^3$. The mesh is dimensioned such that the edges have no influence on the stress-field. Usually, when large deformations are expected, quadratic elements are preferred (no locking), however, in a contact analysis linear elements are recommended [103]. The tip geometry is an exact copy of the surface profile generated by the Sensofar, and is modelled as a rigid impenetrable surface. The contact between indenter and polymer is initially assumed to be frictionless, because only the deformation related component is studied. Subsequently, Coulomb friction is added to the simulations to study its effect.

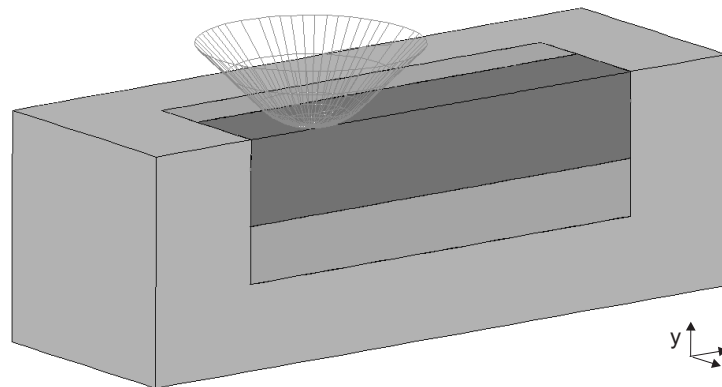


Figure 5.9: The different grey-values indicate the different contact bodies defined.

Boundary conditions

The front, back, side, and bottom are restrained in all directions. The symmetry plane is fixed only in z-direction. The behaviour of the indenter is prescribed by a reference node on the surface. Throughout the simulation, the displacement of the reference node in z-direction is fixed and the chosen sliding velocity in x-direction is applied. Since only half the scratch surface is meshed, the normal load F_n applied is also divided by two, resulting in 150 mN. The simulation is divided into two sections, first the indentation with 150 mN in 10 seconds, thereafter sliding with constant velocity and normal load.

Mesh refinement

The use of hexagonal elements has the disadvantage that, to keep complete connectivity between all neighbouring elements, mesh refinement results in a total mesh which has to be refined, thus reducing the size by a factor of two in all directions, the number of elements increases by a factor of eight. As a rule of thumb, the calculation times in 3D scale at least linearly with the number of elements, and at most with the number of elements squared, resulting in an increase by a factor of 8 to maximum 64. To reduce the calculation times, only the mesh in the regions of interest is refined, see Figure 5.8. To attach discontinuous element-edges the glue option is used. This option results in an extra contact constraint in the contact table. In Figure 5.9 the different contact bodies are depicted with different grey-values. Glueing of elements has the advantage that only the regions where large deformations are expected can be refined, resulting in a less pronounced increase in calculation times; with the mesh shown in Figures 5.8 and 5.9, simulations take, on 16 parallel CPU's (1.8GHz AMD Opteron with 32GB RAM), approximately one week.

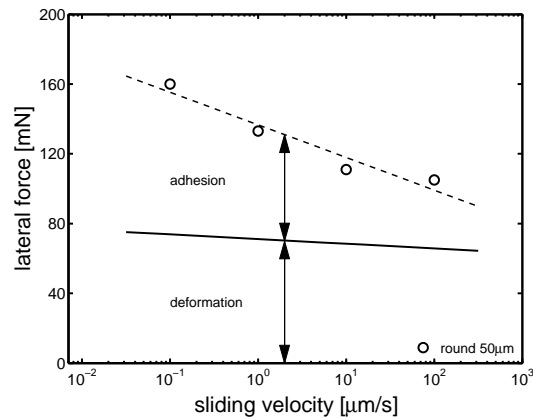


Figure 5.10: Simulations of sliding friction experiments result in the solid line (–), where the fitted experimental data are depicted with the dashed line (– –); the difference results in the additive decomposition of the measured friction force into a deformation and an adhesion component.

Influence of sliding velocity without friction

All the EGP-model parameters, except the value for the parameter representing the thermodynamic state of the material (S_a), are known for PC, see Chapter 2. As shown in Chapter 4 the value of S_a is determined by fitting the load-displacement signal of one indentation experiment on a simulation. In a previous study [146] we found that indentation can be considered completely frictionless, thus when a friction model is applied, the value of S_a will not change and is therefore uniquely defined, resulting in $S_a = 25.1$. With the complete set of model parameters, simulations without friction (no adhesion and thus purely deformation) of the sliding part of the scratch test are performed. The simulation results are depicted in Figure 5.10 with the solid line. Application of the theory of Bowden and Tabor [20], where the friction force is an additive composition of a deformation and an adhesion related component, results in the difference between the solid and the dashed line. From this figure we can conclude that if this theory holds, the adhesion component must be rate (velocity) dependent.

Influence of sliding velocity with friction

Friction is a complex physical phenomenon involving surface roughness, temperature, contact stresses and relative velocities. In the FEM package MSC.Marc, several friction models are available varying from the most simple, and thus most popular, friction model, which is Coulomb friction, to the more complex bilinear models. With increasing complexity also the number of friction-model input parameters increases drastically and, as a consequence, data interpretation becomes blurred by the amount of variables used. Our choice for the Coulomb model is obvious, concerning the prior mentioned arguments. Please note that the Coulomb

friction model is velocity (rate) independent. The model is characterized by:

$$\|\vec{f}_t\| = \mu_f f_n \quad (\text{stick}) \quad \text{and} \quad \vec{f}_t = -\mu_f f_n \cdot \vec{t} \quad (\text{slip}). \quad (5.2)$$

Where \vec{f}_t is the tangential (friction) force, f_n is the normal force, μ_f is the local friction coefficient and \vec{t} the tangential vector in the direction of the relative velocity, defined according to:

$$\vec{t} = \frac{\vec{v}_r}{\|\vec{v}_r\|}, \quad (5.3)$$

in which \vec{v}_r is the relative sliding velocity. For a given normal force, f_n , the friction force has a step function behaviour, based upon the value of the relative sliding velocity \vec{v}_r . Since this discontinuity in friction value causes numerical difficulties, different approximations of this step function are available. The most basic approximation is via an arctangent model. The other approximations again introduce more model parameters, and therefore these are discarded. The arctangent model reads:

$$\vec{f}_t = -\mu_f f_n \frac{2}{\pi} \arctan \left[\frac{\|\vec{v}_r\|}{\delta} \right] \cdot \vec{t}. \quad (5.4)$$

Physically, the value of δ is interpreted as the value of the relative velocity below which sticking occurs. Typically, a value of 1% to 5% of the applied sliding velocity gives realistic simulation data [104]. The effect of friction, for a sliding velocity of $0.1 \mu\text{m}\cdot\text{s}^{-1}$, on the simulated penetration into the surface, and the corresponding lateral force, is depicted in Figure 5.11. The tremendous increase in lateral force is evident. This increase does not result from sink-in of the tip, see Figure 5.11(a), but from the formation of a bow wave in front of the sliding tip, see Figure 5.11(c). These simulations also confirm the findings in our previous study [146], where the indentation response is independent on friction force, since all simulation results start at an identical penetration into the surface. To obtain a representative value for the local friction coefficient (μ_f) and comparing simulations with the experiments of Figures 5.5 and 5.7, a best fit routine is employed. The final result is depicted in Figure 5.12 and results in a value of $\mu_f = 0.2$.

From these simulations we can conclude that a quantitative comparison between simulation and experiment is possible. However, confirmation on the quantitiveness of our approach requires a validation experiment with corresponding simulations.

Influence of tip geometry

The ultimate validation is by performing experiments on the same material, thus an identical thermodynamic state, but with a different indenter tip, that is the sharp tip with a top radius of

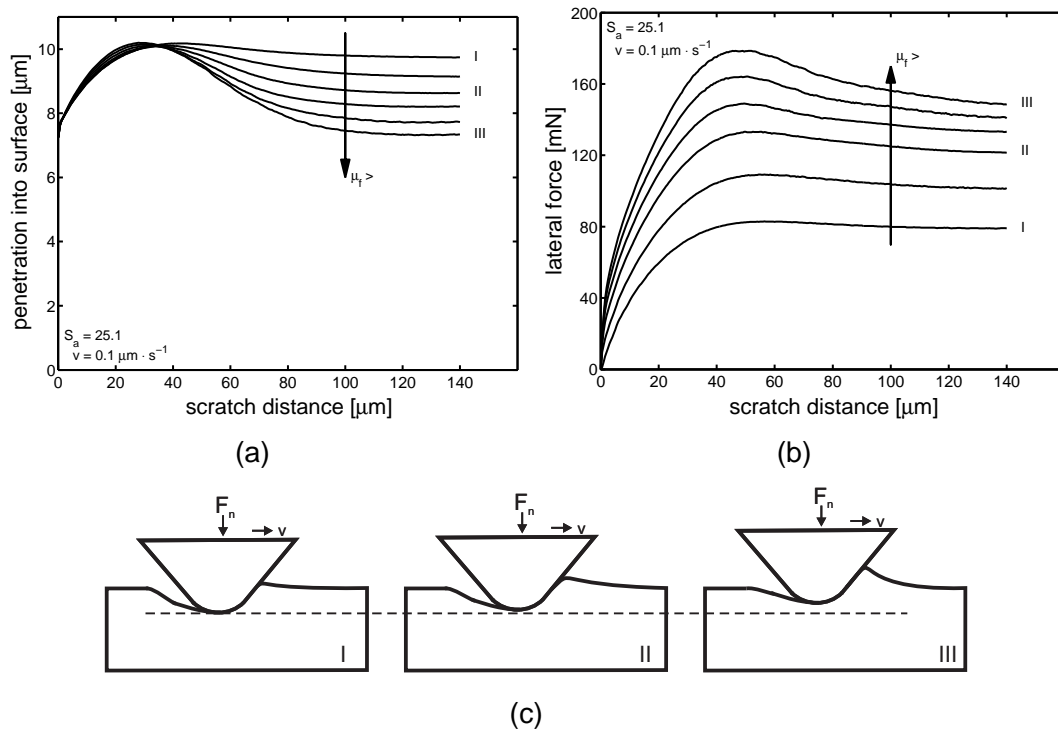


Figure 5.11: Simulated response of a single-asperity scratch experiment with a constant normal load of 300 mN and a sliding velocity of $0.1 \mu\text{m} \cdot \text{s}^{-1}$, with μ_f ranging from 0.0 to 0.2; (a) penetration into the surface versus sliding distance, (b) the lateral force friction versus sliding distance and (c) graphical representation of the observed macroscopic response; the numbers I, II, and III, correspond to the same numbers as in (a) and (b), where the dashed line (- -) is the depth when sliding with $\mu_f = 0.0$.

$10 \mu\text{m}$. Hence in the simulations with the $10 \mu\text{m}$ tip, the S_a -value used is exactly the same as in the $50 \mu\text{m}$ tip simulations. Since the $10 \mu\text{m}$ tip is sharper, the normal load applied is reduced from 300 mN (150 mN in the simulations) to 150 mN (75 mN in the simulations) to obtain comparable penetrations into the surface. The experimental data are shown in Figure 5.13. Because the data, when plotted over the total scratch distance of 1 mm, almost coincide to one curve, the data are only shown up to a scratch distance of 0.4 mm. The effect of sliding velocity is less pronounced when compared to the experiments performed with the $50 \mu\text{m}$ tip, see Figure 5.6. From these data we can even conclude that there is almost no influence of sliding velocity for this tip geometry.

The mesh used in the simulations is shown in Figure 5.14 and consists of 38736 elements. Identical boundary conditions as for the $50 \mu\text{m}$ tip mesh are applied, with this difference that the normal load is 75 mN instead of 150 mN. More important is that the local friction coefficient, $\mu_f = 0.2$, and thermodynamic state of the material, $S_a = 25.1$, are identical to the $50 \mu\text{m}$ tip simulations where a quantitative comparison was achieved. The comparison between experimental data measured with ball-tips of 10 and $50 \mu\text{m}$ and the simulations is

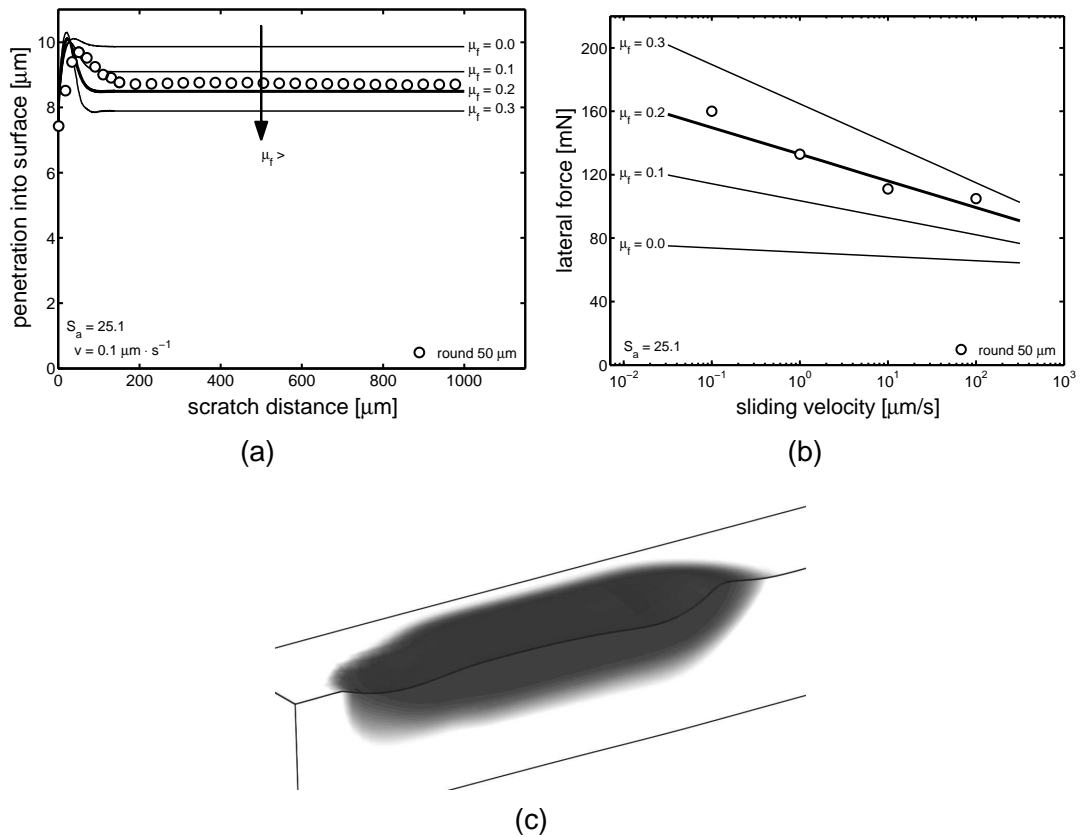


Figure 5.12: (a) Simulated penetration into the surface for different values of μ_f at a sliding velocity of $0.1 \mu\text{m} \cdot \text{s}^{-1}$ compared to experimental data; (b) friction force versus the logarithm of sliding velocity compared to simulations with different values for μ_f ; (c) simulation of the plastic deformation zone, where black is visco-plastic deformation and white is un-deformed or visco-elastic deformation.

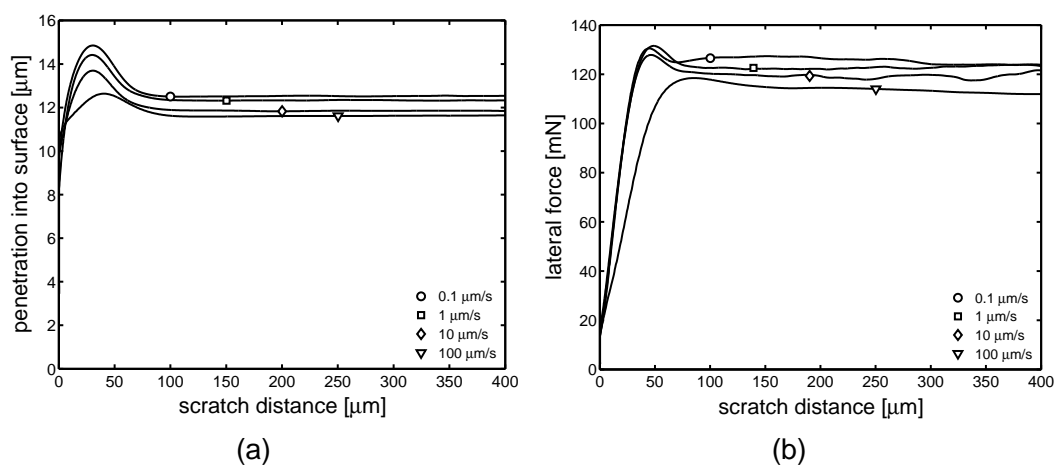


Figure 5.13: Response of Lexan 101R at 4 different sliding velocities with a $10 \mu\text{m}$ tip; (a) penetration into the surface versus sliding distance and (b) friction force versus sliding distance.

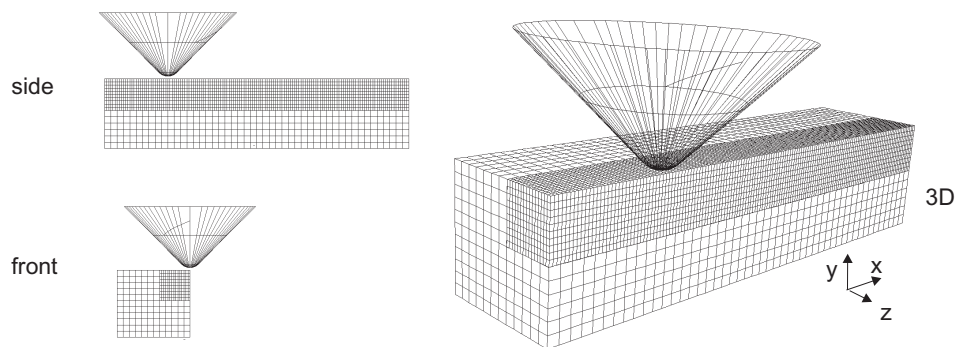


Figure 5.14: Mesh for the 10 μm tip.

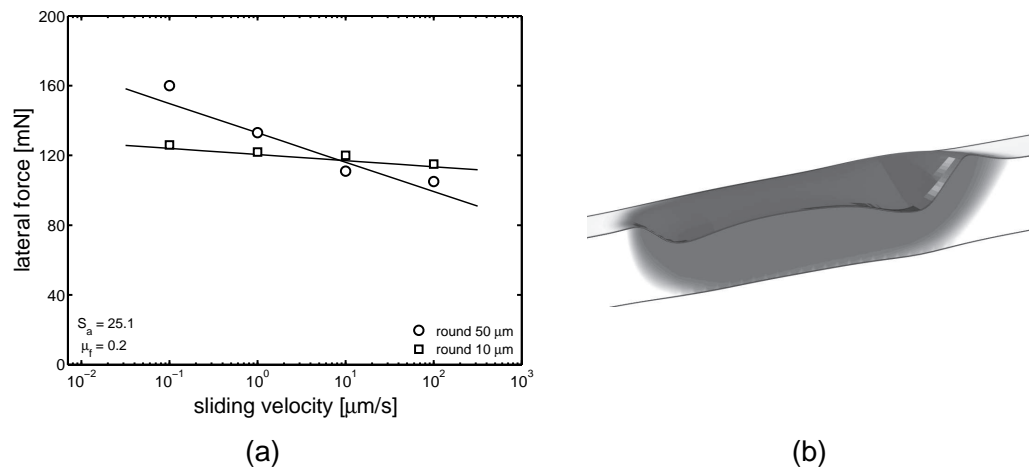


Figure 5.15: (a) Friction force versus the logarithm of sliding velocity, where the experimental data of the sharp 10 μm tip (\square) and the blunt 50 μm tip (\circ) are compared to simulations with identical thermodynamic state of the material ($S_a = 25.1$) and a similar local friction coefficient ($\mu_t = 0.2$); (b) simulation of the plastic deformation zone, where black is visco-plastic deformation and white is un-deformed or visco-elastic deformation.

displayed in Figure 5.15(a). The difference in macroscopic response becomes clear when comparing the simulated response of the 50 μm tip, Figure 5.15(b), with the 10 μm tip, Figure 5.12(c). This observation strongly supports the quantitiveness of our approach.

5.4 Conclusions

Comparing numerical simulations with experimental results shows that quantitative predictions for the single-asperity sliding friction tests indeed are possible. The best value for the friction coefficient between indenter and polymer is $\mu_t = 0.2$, but a much more important conclusion is that friction between diamond indenter and polymer only indirectly contributes to the lateral

(friction) force, via an increase of the plastic deformation zone. Simulations with no adhesive interaction between tip and polymer show almost no influence of the sliding velocity on lateral (friction) force, the solid line for $\mu_f = 0.0$ in Figure 5.10, whereas experiments show a significant influence. In case of an additive decomposition, this would imply a rate/velocity-dependency of the adhesive component. By inclusion of the velocity (rate) independent Amontons-Coulomb friction law, which creates an interaction between tip and polymer, the suggested additive decomposition is proved not to be applicable and the large macroscopic deformation response proves to be the result of small changes in local processes. When indenter-polymer interaction is taken into account, a bow wave is formed in front of the sliding tip, which leads to an increase in contact area between tip and polymer and results in an increase in friction force. As a consequence the experimentally observed time-dependent behaviour of the friction force can solely be attributed to the polymer's intrinsic deformation response. The same holds for the dependence of friction force on sliding velocity. Also that can be solely attributed to the influence of strain rate on the intrinsic properties of the polymer investigated. The quantitative capability of the framework is confirmed by performing simulations on the same material, thus identical thermodynamic state (S_a) and local friction coefficient (μ_f), but with a different tip geometry and normal load applied, resulting in an accurate prediction of the friction force measured. Remarkable is that in both the simulations and the experiments the so-called velocity-weakening, the decrease in friction force with increasing sliding velocity, is strongly indenter geometry dependent; since its geometry directly sets the plastic deformation zone.

Conclusions, recommendations and challenges

6.1 Conclusions

In this thesis the phenomenological constitutive framework as e.g. presented in [85] (the EGP-model) is extended to take non-linear visco-elasticity and thermorheologically complex deformation behaviour into account. The single-mode EGP-model which only captures the intrinsic post-yield response accurately, has been extended into a multi-mode-multi-process constitutive relation, based on the assumption that the pre-yield intrinsic mechanical response is determined by a spectrum of linear relaxation times, which shift to shorter time scales under the influence of stress. The determination of a relaxation time spectrum out of a simple tensile, or compression, test is established. The two typical time-dependencies of glassy polymers, their rate and thermal history dependence, are demonstrated not to influence the definition of the unique reference spectrum. The multi-mode model is the result. The basis of capturing also thermorheologically complex yield phenomena is instituted on the Ree-Eyring modification of Eyring's flow theory, as already employed by a number of researchers. Whether the post-yield response, particularly the material's strain softening, also displays thermorheologically complex behaviour remains, however, unidentified. Some observations on the post yield intrinsic response of PMMA and PC suggest complex behaviour while others, like e.g. Arruda et al. [5] and Mulliken and Boyce [105], relate the increased softening at high deformation rates solely to thermal effects. Thermal effects only partially explain the increased yield drop and are especially manifested at deformation rates above 10^{-2} s^{-1} . In our experiments on PS and PLLA, also at strain rates below 10^{-2} s^{-1} , which is well within the range where experiments can be considered isothermal, an increased yield drop is observed. This observation can only be rationalized by introducing a secondary process contributing to

the post-yield softening response and implies that a rate dependent yield drop is of an intrinsic nature. A multi-process description accurately captures this behaviour.

With these extensions of the EGP-model, we can predict the strain-rate dependence of different amorphous polymers for different loading conditions over a wide range of strain rates and different temperatures. Similar to the life-time predictions performed by Klompen et al. [86] on PC, we showed that a thermorheologically complex approach is required to predict both the intrinsic response and time-to-failure of PLLA, with a single parameter set.

We employed the state-of-the-art constitutive model to numerically predict the indentation response. In the model, a single parameter, the state parameter S_a , is used to uniquely determine the initial state of the material, reflected in the value of its yield stress as it results from the polymer's thermal history. We demonstrated that this model can capture the rate-, and history-dependence of PC and PMMA on both the macroscopic and microscopic scale. The excellent accuracy of the description also creates the possibility to extract the state parameter S_a directly from one micro-indentation experiment.

Finally, we assess the single-asperity sliding friction experiment. Comparing numerical simulations with the experimental results shows that quantitative predictions indeed are possible. Simulations with no adhesive interaction between tip and polymer show almost no influence of the sliding velocity on lateral (friction) force, whereas experiments show a significant influence. In case of an additive decomposition, this would imply a time-dependency of the adhesive component, this seems unrealistic since kinetic friction is independent on sliding velocity. The important conclusion is that friction between the (diamond) indenter and the polymer only indirectly contributes to the lateral (friction) force, via an increase in the plastic deformation zone. By inclusion of the Amontons-Coulomb friction law, which creates an interaction between tip and polymer, the suggested additive decomposition is proved not to be applicable and the large macroscopic deformation response proves to be the result of small changes in local processes. When indenter-polymer interaction is taken into account, a bow wave is formed in front of the sliding tip, which leads to an increase in contact area between tip and polymer and results in an increase in friction force. As a consequence, the experimentally observed time-dependent and sliding-velocity dependent friction force can be solely attributed to the influence of strain rate on the intrinsic properties of the polymer investigated. As a result, velocity-weakening can be explained as the result of a decreased scratch depth under the same normal load, caused by the increased yield stress at higher deformation rates. The quantitative capability of the framework is confirmed by performing simulations on the same material, thus identical thermodynamic state (S_a) and local friction coefficient (μ_f), but with a sharper tip geometry and with a lower normal load applied, in order to keep the penetration into the surface approximately the same. An accurate prediction results for the friction force measured, which shows in this case only a mild velocity weakening in both experiment and simulation.

6.2 Recommendations

The combination of the FEM-tool and the extended constitutive relation now provides us with a powerful tool that enables direct, numerical, evaluation of the single-asperity sliding friction performance and its coupling to the intrinsic mechanical properties of polymer glasses. In Figure 6.1 an overview is presented of the change in intrinsic properties that may be anticipated.

Intrinsic response

The first two are of course the two typical time-dependencies [85] that are displayed by polymer glasses. The first is the dependence of the intrinsic behaviour on strain rate, and for polycarbonate is (PC) presented in Figure 6.1(a). With increase of strain rate the yield stress increases, as well as the post-yield response; all the curves shift upward. The second time-dependency is the influence of the age on the material. Since polymer glasses are not in thermodynamic equilibrium after processing, the material physically ages over time [130], as displayed for PC in Figure 6.1(b). A well known method to accelerate this process is an annealing treatment of the material. Physical ageing results in an increase in yield stress. The post-yield response, however, is not affected above a strain of 0.4; here the curves fully coincide. An increase in yield stress therefore also results in an increase in strain softening; both a higher resistance against creep loading and embrittlement are the result. Finally it has been shown that the influence of the molecular weight of PC on this intrinsic response is negligible [85].

Strain hardening, which manifests itself at high strains and influences the macroscopic response, can also be manipulated. In the miscible system polystyrene (PS) - poly(2,6-dimethyl-1,4-phenylene oxide) (PPO), different compositions give different strain-hardening moduli, see Figure 6.1(c) [149]. The influence of molecular architecture of polymer glasses on the intrinsic response measured, in a compression test at a strain rate of $1 \cdot 10^{-3} \text{ s}^{-1}$ is shown for 5 different glassy polymers, PEI, PMMA, PC, PS, and PLDLLA in Figure 6.1(d). We can conclude that all polymers considered can be captured within the constitutive framework as presented in Chapters 2 and 3.

In the previous chapter (Chapter 5) the influence of strain rate, reflected in the sliding velocity, on the friction force is studied. For two different indenter geometries, a blunt indenter with a top radius of $50 \mu\text{m}$ and a sharp indenter with a radius of $10 \mu\text{m}$, an accurate description of the intrinsic behaviour of PC results in a quantitative description of both the penetration into the surface, and the lateral (friction) force. The thermodynamic state, the second intrinsic time-dependency, is not considered.

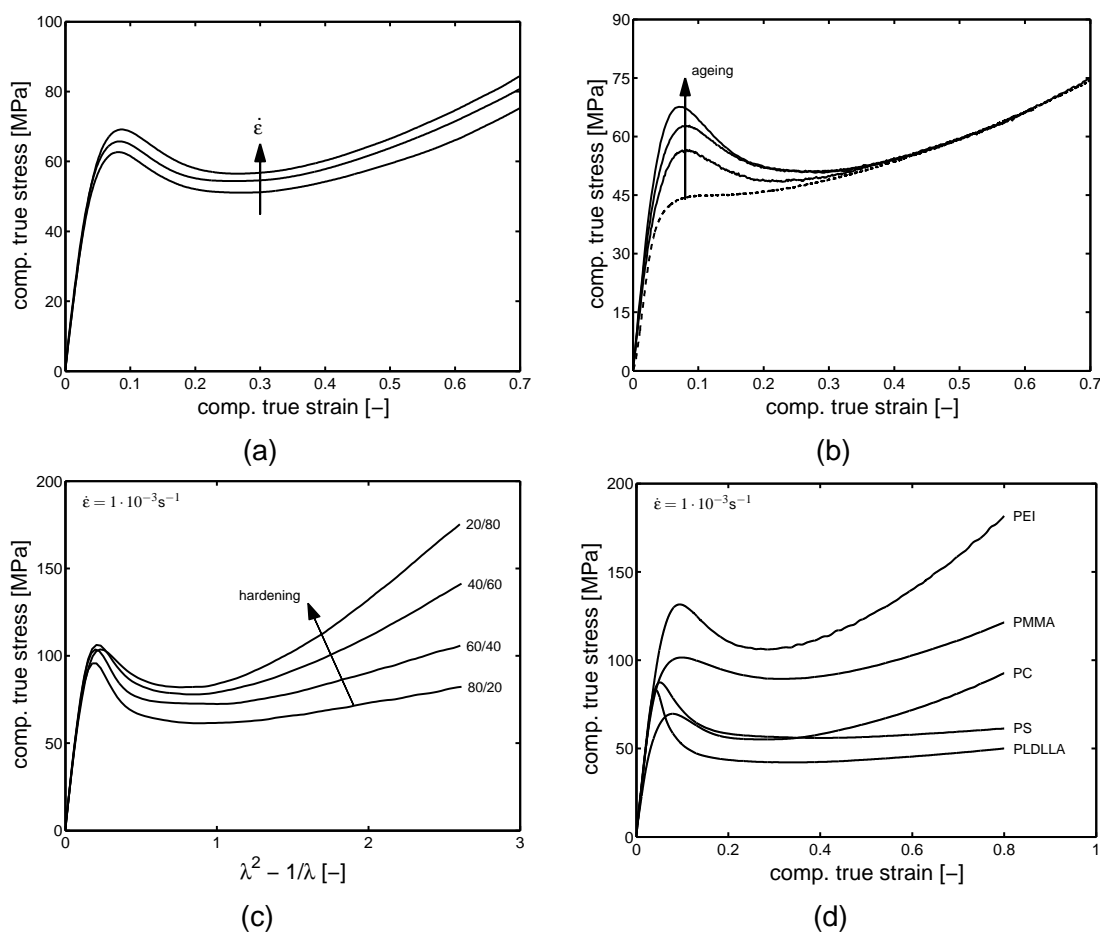


Figure 6.1: Intrinsic stress-strain response: (a) dependence on strain rate; (b) dependence on thermodynamic state (c) dependence on PS/PPO composition resulting in a difference in strain-hardening modulus [149]; (d) dependence on molecular architecture.

Single-asperity sliding friction experiments

A continuation of this study is therefore the assessment of the frictional response of PC at different thermodynamic states and different molecular weights. Since molecular weight does not influence the intrinsic response, no influence on the friction force is anticipated. The first experiments on two grades of PC, OQ1020 (CD-grade, low molecular weight) and 101R (the highest molecular weight commercially available), and are depicted in Figures 6.2(a) and 6.2(b). In Figure 6.2(a) the residual deformation profile, characterized by the height H , generated with the Sensofar, is displayed. The quenched materials are subjected to an identical thermal treatment, resulting in an equal thermodynamic state. With annealing treatments, similar for both grades, the thermodynamic state, and as a result the yield stress, is changed. With an increase in yield stress also the resistance to deformation increases. As a consequence, a higher normal load has to be applied to achieve an identical displacement into the surface. Since this load is not altered, and kept at 300 mN, the response as displayed

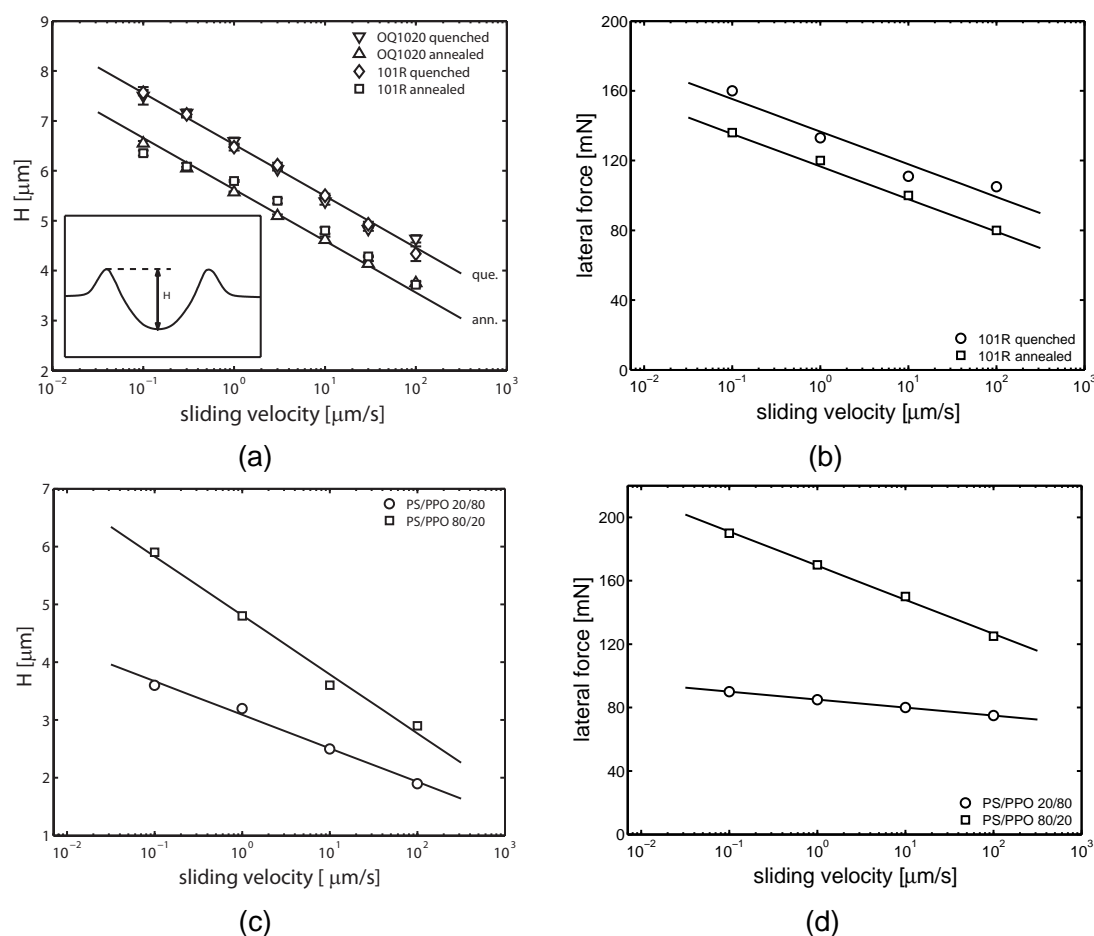


Figure 6.2: Influence of ageing for polycarbonate at different sliding velocities, the solid (–) drawn lines are guides to the eye, where (a) displays the residual deformation and (b) the lateral (friction) force. Influence of strain hardening for different PS/PPO compositions at different sliding velocities, where (c) displays the residual deformation and (d) the lateral (friction) force.

in Figure 6.2(a) follows: due to the increase in yield stress, a decrease in penetration depth is observed, and thus also a decrease in residual deformation. A similar increase in yield stress, now with increasing deformation rate, results in the decrease in penetration depth, and thus friction force, with increasing sliding velocity. The molecular weight clearly does not influence the residual deformation. Figure 6.2(b) shows the influence of annealing of the high molecular weight 101R sample. The results display the lateral (friction) force versus sliding velocity and an identical dependence on sliding velocity is observed. This is an indication that simply changing the thermodynamic state (the value of S_d) in the simulation will result in at least a qualitative, and maybe even a quantitative, description of both the penetration into the surface and the friction force.

The second dependence on intrinsic polymer properties considered, is the influence of strain hardening. Two blends of PS/PPO, that is a 20/80 and a 80/20 composition, are studied, both

with identical thermodynamic history. The dependence of residual deformation and friction force on sliding velocity are displayed in Figures 6.2(c) and 6.2(d). In Figure 6.2(c) the residual deformation for both blends displays a linear dependence, albeit with a difference in slope, on the logarithm of sliding velocity. The difference in strain hardening (see Figure 6.1(c)) results in a less pronounced penetration into the surface for the blend with the highest strain-hardening modulus, i.e. PS/PPO 20/80. The difference in slope is explained by intrinsic material properties, since the PS/PPO 80/20 blend displays a higher strain-rate dependence as compared to the PS/PPO 20/80 blend. Similar observations are found in Figure 6.2(d) for the friction force measured, an analogous explanation as for the penetration into the surface can be given. Since the friction force is directly related to the contact area generated during sliding, which is less when a higher strain hardening is present, as a result a lower friction force is measured.

Preliminary numerical simulations

The hybrid numerical/experimental approach, presented in Chapter 5, is adopted for the experimental observations as displayed in the previous subsection. Here we present simulations for the frictionless case ($\mu_f = 0.0$). On the left-hand side of Figure 6.3 the results are displayed for the case where the thermodynamic state is varied, with S_a -values ranging from 0.0 to 35.0. On the right-hand side the results are displayed for a material with a fixed thermal history, thus treating S_a as a constant ($S_a = 35.0$), but with a difference in strain-hardening modulus, ranging from 5 MPa to 40 MPa.

From the simulations performed with a difference in thermodynamic state we can conclude that the behaviour is exactly as expected. With increasing age, resulting in an increase in yield stress, the penetration into the surface becomes less and thus the contact area generated during sliding is smaller and, as a consequence, the friction force decreases. The response observed with an increase in strain-hardening modulus is not clear-cut and is not as expected. An explanation is sought in the change in the plastic deformation zone. This zone is more localized for a lower strain-hardening modulus, resulting in a smaller bow wave in front of the tip, leading to a smaller contact area which is directly related to the friction force. This effect is not observed in experiments and therefore further study is required. Implementing the interaction between tip and polymer, via the simple friction model, may give better results in accordance with the experimentally observed behaviour, by an increase in the size of the bow wave. Time restrictions in preparing this thesis prevent this straightforward check.

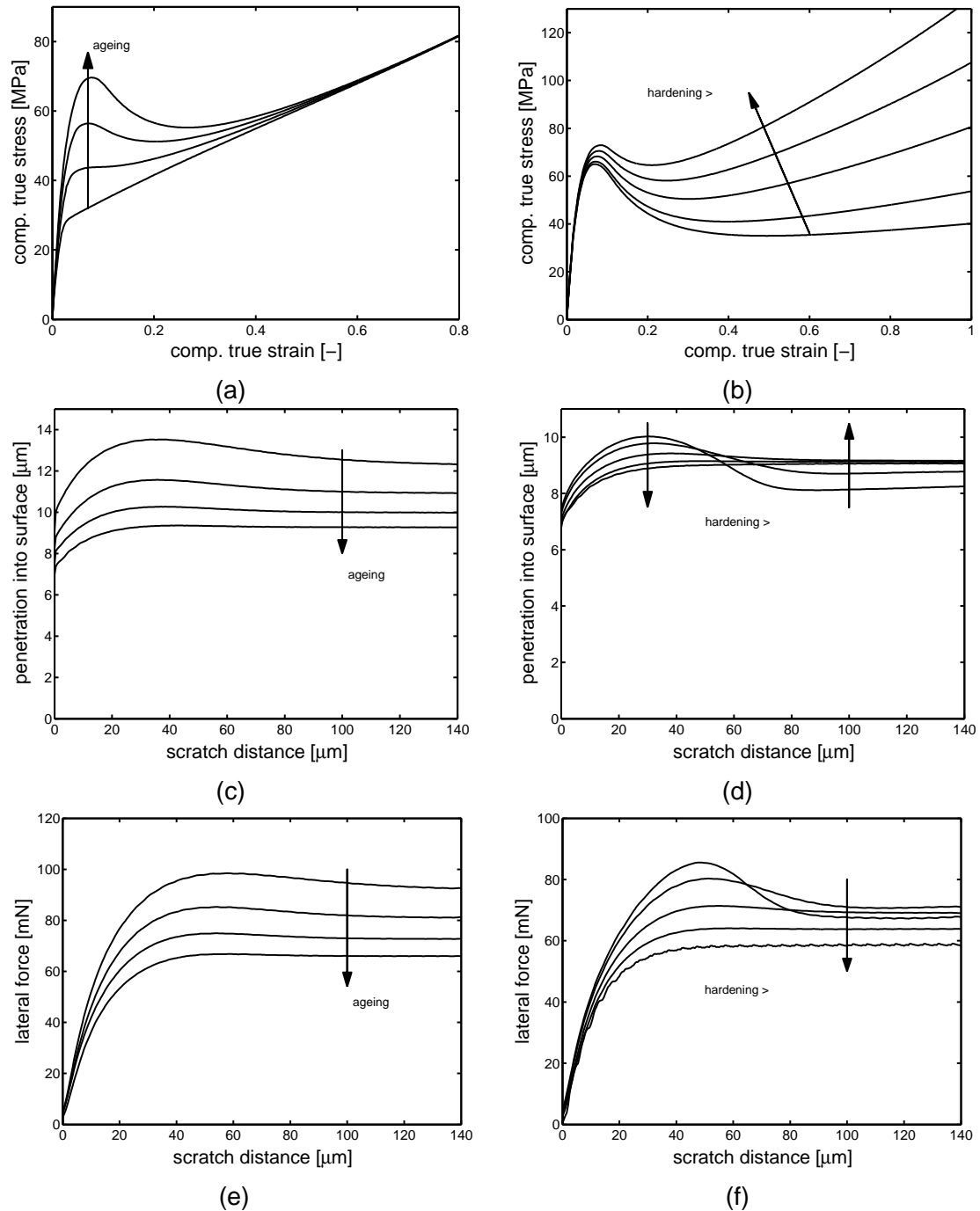


Figure 6.3: Results of numerical simulations with no adhesive component ($\mu_t = 0.0$), with on the left-hand side ((a),(c), and (e)) the change in response as a result of intrinsic ageing and on the right-hand side ((b),(d), and (f)) the results for the response with an increase in intrinsic strain hardening.

6.3 Challenges

A burning issue not concerned in this thesis, and which is of great interest in tribology is the explanation when, and how, wear sets in. In Figure 6.4 sliding experiments on PS are displayed, with a constant sliding velocity ($10 \mu\text{m}\cdot\text{s}^{-1}$) and different normal loads applied (300 mN and 400 mN). The surface profiles shown in Figure 6.4(a) display an obvious difference. The sample subjected to a normal load of 300 mN does not display small cracks in the sliding path, whereas the sample loaded with a normal load of 400 mN clearly does. It is known for PS [107, 148], and also for PC [76, 80, 108], that when a critical positive hydrostatic stress is reached, brittle failure of the material results. An increase in normal load leads to an increase in hydrostatic stress. To corroborate this hypothesis, a simulation on PS (again without friction) is performed, the result for the positive hydrostatic stress is displayed in Figure 6.4(b). The simulation displays a maximum positive hydrostatic stress just behind the sliding tip in the centre of the sliding track. Comparing the simulation data with experiments confirms the development of cracks behind the indenter; the cracks are opened during sliding, resulting in a crescent-shaped deformation pattern. Another confirmation is the repetitiveness of the cracks observed, this suggests a continuous build-up of hydrostatic stresses, which are released when a crack is formed.

Temperature effects are currently not included in the computations. The option to perform a thermo-mechanically coupled simulation is available in the current implementation of the MSC.Marc package. This option also allows the examination of viscous heat dissipation which will occur at higher sliding velocities. Interestingly, the resulting softening could lead to deeper tip penetration at the same normal load applied, and thus an increased contact area and increased friction force. This might explain the occurrence of velocity hardening at (very) high sliding rates. To quantify the influence of temperature an extension of the experimental set-up is required, since all experiments are performed under ambient conditions. A possible machine extension would be to include an environmental chamber, this also allows the analysis of the influence of humidity on observed friction and wear behaviour. Another limitation of the current set-up is the limited range of applicable sliding velocities (4 decades), which are applied via a standard x-y table as provided with the machine. This limitation can be removed by including a separate sliding stage, using for instance the piezo stage (6 decades of sliding velocity) developed for the Lateral Force Apparatus (LFA) [73].

An important issue in contact mechanics is the prediction of the *real* contact area. In a previous study, Pelletier et al. [113] demonstrated that not only the force-displacement response of spherical tip indentation, but also the development of *real* contact area could be quantitatively predicted using the EGP-model as a numerical tool. The contact area was experimentally quantified using a novel in-situ technique developed by Sakai et al. [124]. Since similar set-ups have also been developed for in-situ observations of contact area development of polymer glasses in a single-asperity sliding friction experiment [54], it seems worthwhile to validate our

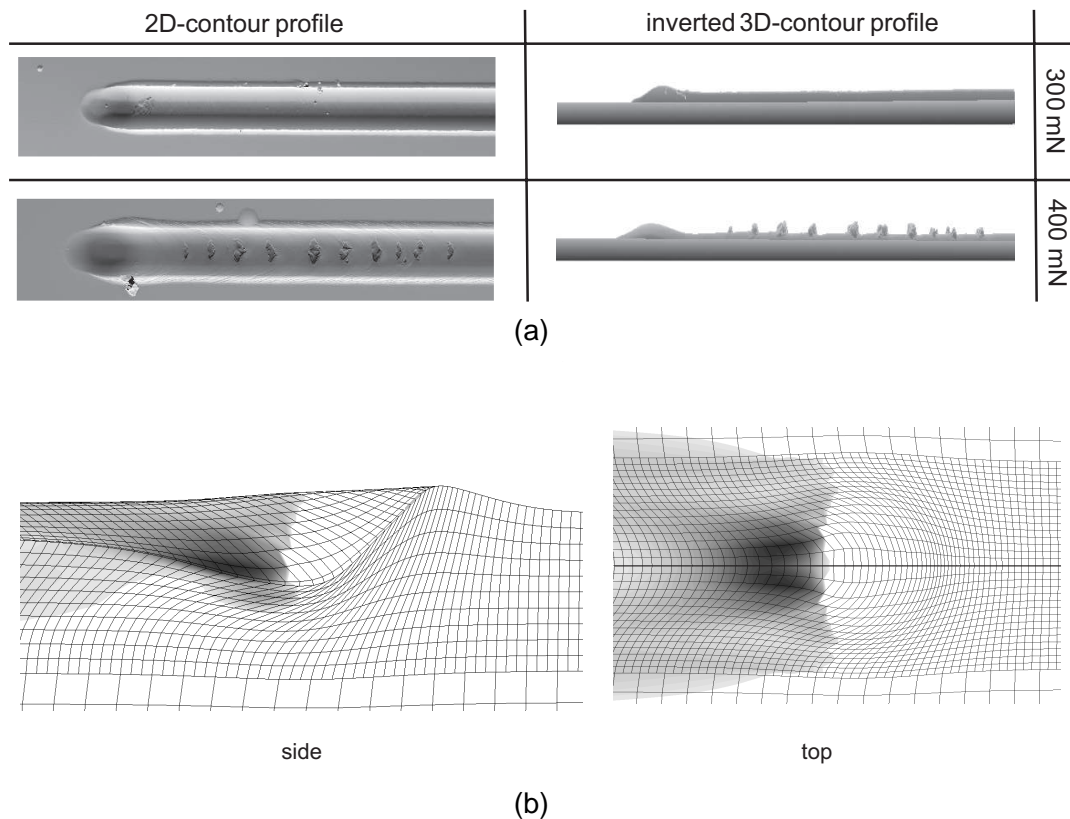


Figure 6.4: Effect of scratch load for polystyrene at a sliding velocity of $10 \mu\text{m}\cdot\text{s}^{-1}$; (a) scratch profile generated with the Sensofar, the top indicates the response for a normal load of 300 mN and the bottom displays the response for a normal load of 400 mN. From this profile the onset of wear is clearly visible, which manifests itself as small cracks in the surface profile; (b) the positive hydrostatic pressure as observed in a simulation, where black indicates the maximum hydrostatic pressure, which corresponds with the locations in (a) where cracks are observed.

tool on this point.

The hybrid numerical/experimental approach provides a powerful tool in unravelling single-asperity friction and wear phenomena. The work presented in this thesis is a useful start. To fully couple the physical friction and wear phenomena to intrinsic polymer properties for different polymer glasses, and in a later stage even semi-crystalline polymers, is indeed a challenging task. The now empirical local friction coefficient, μ_f , which determines the interaction between diamond tip and polymer, is not related to any physical quantity. A means to study the influence of polymer-tip interaction is by performing experiments with the same polymer, but different tip material, e.g. sapphire, glass or metal. It can be argued that even simulations on a molecular level are required to couple intrinsic mechanical properties to physical adhesion quantities.

References

- [1] D.B. Adolf, R.S. Chambers, J. Flemming, J. Budzien, and J. McCoy. Potential energy clock model: Justification and challenging predictions. *J. Rheol.*, 51(3):517–540, 2007.
- [2] L. Anand and N.M. Ames. On modeling the micro-indentation response of an amorphous polymer. *Int. J. Plast.*, 22(6):1123–1170, 2006.
- [3] J.F. Archard. Elastic deformation and the laws of friction. *Proc. R. Soc. London, Ser.-A*, 243:190–205, 1957.
- [4] E.M. Arruda and M.C. Boyce. Evolution of plastic anisotropy in amorphous polymers during finite straining. *Int. J. Plast.*, 9(6):697–720, 1993.
- [5] E.M. Arruda, M.C. Boyce, and R. Jayachandran. Effects of strain rate, temperature and thermomechanical coupling on the finite strain deformation of glassy polymers. *Mech. Mat*, 19(2-3):193–212, 1995.
- [6] F.P.T. Baaijens. Calculation of residual stresses in injection molded products. *Rheol. Acta*, 30(3):284–299, 1991.
- [7] P. Bardia and R. Narasimhan. Characterisation of pressure-sensitive yielding in polymers. *Strain*, 42(3):187–196, 2006.
- [8] T. Baumberger, P. Berthoud, and C. Caroli. Physical analysis of the state- and rate-dependent friction law. ii. dynamic friction. *Phys. Rev. B - Condensed Matter and Materials Physics*, 60(6):3928–3939, 1999.
- [9] J.C. Bauwens. Differences between the effects of annealing and physical aging on the mechanical behaviour of polycarbonate. *Plast. Rub. Proc. Appl.*, 7(3):143–147, 1987.
- [10] J.C. Bauwens, C. Bauwens-Crowet, and G. Homès. Tensile yield-stress behavior of poly(vinyl chloride) and polycarbonate in the glass transition region. *J. Polym. Sci. A2*, 7(10):1745–1754, 1969.

- [11] C. Bauwens-Crowet. The compression yield behaviour of polymethyl methacrylate over a wide range of temperatures and strain-rates. *J. Mater. Sci.*, 8(7):968–979, 1973.
- [12] C. Bauwens-Crowet and J.C. Bauwens. Annealing of polycarbonate below the glass transition: quantitative interpretation of the effect on yield stress and differential scanning calorimetry measurements. *Polymer*, 23(11):1599–1604, 1982.
- [13] C. Bauwens-Crowet and J.C. Bauwens. Effect of thermal history on the tensile yield stress of polycarbonate in the β transition range. *Polymer*, 24(7):921–924, 1983.
- [14] C. Bauwens-Crowet, J.C. Bauwens, and G. Homès. Tensile yield-stress behavior of glassy polymers. *J. Polym. Sci. A2*, 7(4):735–742, 1969.
- [15] C. Bauwens-Crowet, J.C. Bauwens, and G. Homès. The temperature dependence of yield of polycarbonate in uniaxial compression and tensile tests. *J. Mater. Sci.*, 7(2): 176–183, 1972.
- [16] C. Bauwens-Crowet, J.M. Ots, and J.C. Bauwens. The strain-rate and temperature dependence of yield of polycarbonate in tension, tensile creep and impact tests. *J. Mater. Sci.*, 9(7):1197–1201, 1974.
- [17] B. Bernstein and A. Shokooh. The stress clock function in viscoelasticity. *J. Rheol.*, 24 (2):189–211, 1980.
- [18] P. Berthoud, T. Baumberger, C. G'Sell, and J.-M. Hiver. Physical analysis of the state- and rate-dependent friction law: Static friction. *Phys. Rev. B - Condensed Matter and Materials Physics*, 59(22):14313–14327, 1999.
- [19] F.P. Bowden and D. Tabor. *The Friction and Lubrication of Solids*. Oxford University Press, 2001.
- [20] F.P. Bowden, A.J.W. Moore, and D. Tabor. The ploughing and adhesion of sliding metals. *J. Appl. Phys.*, 14(2):80–91, 1943.
- [21] M.C. Boyce, D.M. Parks, and A.S. Argon. Large inelastic deformation of glassy polymers. part I: rate dependent constitutive model. *Mech. Mat*, 7(1):15–33, 1988.
- [22] M.C. Boyce, E.M. Arruda, and R. Jayachandran. Large strain compression, tension, and simple shear of polycarbonate. *Polym. Eng. Sci.*, 34:716–725, 1994.
- [23] B.J. Briscoe. Isolated contact stress deformations of polymers: The basis for interpreting polymer tribology. *Tribol. Int.*, 31(1-3):121–126, 1998.
- [24] B.J. Briscoe and K.S. Sebastian. The elastoplastic response of poly(methyl methacrylate) to indentation. *Proc. Royal Soc. London A.*, 452:439–457, 1996.

- [25] B.J. Briscoe and S.K. Sinha. Scratch resistance and localised damage characteristics of polymer surfaces - a review. *Mater.wis. Werkstofftech.*, 34(10-11):989–1002, 2003.
- [26] B.J. Briscoe and D. Tabor. Friction and wear of polymers: The role of mechanical properties. *Br Polym J*, 10(1):74–78, 1978.
- [27] B.J. Briscoe, P.D. Evans, S.K. Biswas, and S.K. Sinha. The hardnesses of poly(methylmethacrylate). *Tribol. Int.*, 29(2):93–104, 1996.
- [28] B.J. Briscoe, P.D. Evans, E. Pelillo, and S.K. Sinha. Scratching maps for polymers. *Wear*, 200(1-2):137–147, 1996.
- [29] B.J. Briscoe, E. Pelillo, and S.K. Sinha. Scratch hardness and deformation maps for polycarbonate and polyethylene. *Polym. Eng. Sci.*, 36(24):2996–3005, 1996.
- [30] J.L. Bucaille, E. Felder, and G. Hochstetter. Mechanical analysis of the scratch test on elastic perfectly plastic materials with the three-dimensional finite element modeling. *Wear*, 249(5-6):422–432, 2001.
- [31] J.L. Bucaille, E. Felder, and G. Hochstetter. Experimental and three-dimensional finite element study of scratch test of polymers at large deformations. *J. Tribol.*, 126(2):372–379, 2004.
- [32] C.P. Buckley and D.C. Jones. Glass-rubber constitutive model for amorphous polymers near the glass transition. *Polymer*, 36(17):3301–3312, 1995.
- [33] C.P. Buckley, P.J. Dooling, J. Harding, and C. Ruiz. Deformation of thermosetting resins at impact rates of strain. part 2: Constitutive model with rejuvenation. *J. Mech. Phys. Solids*, 52(10):2355–2377, 2004.
- [34] A.M. Bueche and D.G. Flom. Surface friction and dynamic mechanical properties of polymers. *Wear*, 2(3):168–182, 1959.
- [35] J.M. Caruthers, D.B. Adolf, R.S. Chambers, and P. Shrikhande. A thermodynamically consistent, nonlinear viscoelastic approach for modeling glassy polymers. *Polymer*, 45(13):4577–4597, 2004.
- [36] M.L. Cerrada and G.B. McKenna. Physical aging of amorphous pen: Isothermal, isochronal and isostructural results. *Macromolecules*, 33(8):3065–3076, 2000.
- [37] L. Cheng, X. Xia, W. Yu, L. E. Scriven, and W. W. Gerberich. Flat punch indentation of viscoelastic material. *J. Polym. Sci. Part B*, 38(1):10–22, 2000.
- [38] L. Cheng, X. Xia, L. E. Scriven, and W. W. Gerberich. Spherical-tip indentation of viscoelastic material. *Mech. of Mat.*, 37:213–226, 2005.

- [39] A.W. Christiansen, E. Baer, and S.V. Radcliff. Mechanical behaviour of polymers under high pressure. *Philos. Mag.*, 24(188):451–8, 1971.
- [40] J. Chu, L. Rumao, and B. Coleman. Scratch and mar resistance of filled polypropylene materials. *Polym. Eng. Sci.*, 38(11):1906–1914, 1998.
- [41] J. Chu, C. Xiang, H.-J. Sue, and R.D. Hollis. Scratch resistance of mineral-filled polypropylene materials. *Polym. Eng. Sci.*, 40(4):944–955, 2000.
- [42] J.M.J. den Toonder, Y. Ramone, A.R. van Dijken, J.G.J. Beijer, and G.Q. Zhang. Viscoelastic characterization of low-dielectric-constant silk films using nano-indentation. *Proceedings of the 3rd International Conference on Benefiting from Thermal and Mechanical Simulation in (Micro)-Electronics*, pages 270–280, 2002.
- [43] J.M.J. den Toonder, Y. Ramone, A.R. van Dijken, J.G.J. Beijer, and G.Q. Zhang. Viscoelastic characterization of low-dielectric-constant silk films using nano-indentation in combination with finite element modeling. *J. Electron. Packag.*, 127:267–285, 2005.
- [44] R.A. Duckett, S. Rabinowitz, and I.M. Ward. The strain-rate, temperature and pressure dependence of yield of isotropic poly(methylmethacrylate) and poly(ethylene terephthalate). *J. Mater. Sci.*, 5(10):909–915, 1970.
- [45] R.A. Duckett, B.C. Goswami, L.S.A. Smith, I.W. Ward, and A.M. Zihlif. Yielding and crazing behaviour of polycarbonate in torsion under superposed hydrostatic pressure. *Br. Polym. J.*, 10(1):11–16, 1978.
- [46] T.A.P. Engels, L.E. Govaert, G.W.M. Peters, and H.E.H. Meijer. Processing-induced properties in glassy polymers: Application of structural relaxation to yield stress development. *J. Polym. Sci. Part B*, 44(8):1212–1225, 2006.
- [47] T.A.P. Engels, L.C.A. van Breemen, L.E. Govaert, and H.E.H. Meijer. Predicting age-induced embrittlement of glassy polymers. *Polymer*, 2009. submitted.
- [48] B.L. Evans. The microhardness of injection moulded polystyrene and polyethylene. *J. Mater. Sci.*, 24(1):173–182, 1989.
- [49] H. Eyring. Viscosity, plasticity, and diffusion as examples of absolute reaction rates. *J. Chem. Phys.*, 4(4):283–291, 1936.
- [50] E. Felder and J.L. Bucaille. Mechanical analysis of the scratching of metals and polymers with conical indenters at moderate and large strains. *Tribol. Int.*, 39(2):70–87, 2006.
- [51] J.D. Ferry. *Viscoelastic properties of polymers*. John Wiley & Sons Inc., New York, 1980.

- [52] R.A.W. Fraser and I.M. Ward. The impact fracture behaviour of notched specimens of polycarbonate. *J. Mater. Sci.*, 12(3):459–468, 1977.
- [53] K. Friedrich, K. Varadi, T. Goda, and H. Giertzsich. Finite element analysis of a polymer composite subjected to a sliding steel asperity Part II: Parallel and anti-parallel fibre orientations. *J. Mater. Sci.*, 37(16):3497–3507, 2002.
- [54] C. Gauthier, S. Lafaye, and R. Schirrer. Elastic recovery of a scratch in a polymeric surface: Experiments and analysis. *Tribol. Int.*, 34(7):469–479, 2001.
- [55] A.E. Giannakopoulos, P.L. Larsson, and R. Vestergaard. Analysis of vickers indentation. *Int. J. Solids Struct.*, 31(19):2679–2708, 1994.
- [56] I.W. Gilmour, A. Trainor, and R.N. Haward. Elastic moduli of glassy polymers at low strains. *J. Appl. Polym. Sci.*, 23(10):3129–3138, 1979.
- [57] T. Goda, K. Varadi, K. Friedrich, and H. Giertzsich. Finite element analysis of a polymer composite subjected to a sliding steel asperity: Part i - normal fibre orientation. *J. Mater. Sci.*, 37(8):1575–1583, 2002.
- [58] J.H. Golden, B.L. Hammant, and E.A. Hazell. Effect of thermal pretreatment on strength of polycarbonate. *J. Appl. Polym. Sci.*, 11(8):1571–1579, 1967.
- [59] L.E. Govaert, P.H.M. Timmermans, and W.A.M. Brekelmans. The influence of intrinsic strain softening on strain localization in polycarbonate: Modeling and experimental validation. *J. Eng. Mater.-T. ASME*, 122(2):177–185, 2000.
- [60] L.E. Govaert, H.J. Schellens, H.J.M. Thomassen, R.J.M. Smit, L. Terzoli, and T. Peijs. A micromechanical approach to time-dependent failure in off-axis loaded polymer composites. *Compos. Part A-Appl. S.*, 32(12):1697–1711, 2001.
- [61] L.E. Govaert, T.A.P. Engels, E.T.J. Klompen, G.W.M. Peters, and H.E.H. Meijer. Processing-induced properties in glassy polymers: Development of the yield stress in PC. *Int. Polym. Process.*, 20(2):170–177, 2005.
- [62] L.E. Govaert, P.J. de Vries, P.J. Fennis, W.F. Nijenhuis, and J.P. Keustermans. Influence of strain rate, temperature and humidity on the tensile yield behaviour of aliphatic polyketone. *Polymer*, 41(5):1959–1962, 2000.
- [63] J.A. Greenwood and D. Tabor. The friction of hard sliders on lubricated rubber: The importance of deformation losses. *Proceedings of the Physical Society*, 71(6):989–1001, 1958.
- [64] J.A. Greenwood and J.B.P. Williamson. Contact of nominally flat surfaces. *Proc. R. Soc. London*, 295:300–319, 1966.

- [65] J.A. Greenwood and J.J. Wu. Surface roughness and contact: An apology. *Meccanica*, 36(6):617–630, 2001.
- [66] D.W. Grijpma and A.J. Pennings. (Co)polymers of L-lactide, 2. Mechanical properties. *Macromol. Chem. Phys.*, 195(5):1649–1663, 1994.
- [67] K.A. Grosch. Relation between friction and visco-elastic properties of rubber. *Proc. R. Soc. Lon. Ser.-A*, 274(AUG):21–8, 1963.
- [68] C. G'Sell, J.M. Hiver, A. Dahoun, and A. Souahi. Video-controlled tensile testing of polymers and metals beyond the necking point. *J. Mater. Sci.*, 27(18):5031–5039, 1992.
- [69] O.A. Hasan and M.C. Boyce. Constitutive model for the nonlinear viscoelastic viscoplastic behavior of glassy polymers. *Polym. Eng. Sci.*, 35(4):331–344, 1995.
- [70] O.A. Hasan, M.C. Boyce, X.S. Li, and S. Berko. Investigation of the yield and postyield behavior and corresponding structure of poly(methyl methacrylate). *J. Polym. Sci., Part B: Polym. Phys.*, 31(2):185–197, 1993.
- [71] R.N. Haward and G. Thackray. Use of a mathematical model to describe isothermal stress-strain curves in glassy thermoplastics. *Proc. R. Soc. Lon. Ser.-A*, 302(1471):453–472, 1968.
- [72] J. Heijboer. Molecular origin of relaxations in polymers. *Annals Of The New York Academy Of Sciences*, 279(OCT15):104–116, 1976.
- [73] C.P. Hendriks and W.P. Vellinga. Quantitative measurement of sliding friction dynamics at mesoscopic scales: The lateral force apparatus. *Rev. Sci. Instrum.*, 71(6):2391–2402, 2000.
- [74] H. Hertz. Uber die berhrung fester elastischer korper (on the contact of elastic solids). *J. Reine Angew. Math.*, 92:156–171, 1881.
- [75] J.M. Hutchinson. Physical aging of polymers. *Prog. Polym. Sci.*, 20:703–760, 1995.
- [76] M. Ishikawa, I. Narisawa, and H. Ogawa. Criterion for craze nucleation in polycarbonate. *J. Polym. Sci., Part B: Polym. Phys.*, 15(10):1791–1804, 1977.
- [77] V. Jardret, H. Zahouani, J.L. Loubet, and T.G. Mathia. Understanding and quantification of elastic and plastic deformation during a scratch test. *Wear*, 218(1):8–14, 1998.
- [78] K.L. Johnson. The correlation of indentation experiments. *J. Mech. and Phys. Solid*, 18:115–128, 1970.
- [79] K.L. Johnson. *Contact mechanics*. Cambridge University Press, 1985.

- [80] R.P. Kambour and E.A. Farraye. Crazeing beneath notches in ductile glassy polymers: a materials correlation. *Polym. Commun.*, 25(12):357–360, 1984.
- [81] G. Kermouche, J.L. Loubet, and J.M. Bergheau. Extraction of stress-strain curves of elastic-viscoplastic solids using conical/pyramidal indentation testing with application to polymers. *Mech. Mat.*, 40(4-5):271–283, 2008.
- [82] E.T.J. Klompen. *Mechanical properties of solid polymers*. PhD thesis, Eindhoven University of Technology, 2005. URL <http://www.mate.tue.nl/mate/pdfs/4944.pdf>.
- [83] E.T.J. Klompen and L.E. Govaert. Nonlinear viscoelastic behaviour of thermorheologically complex materials: A modelling approach. *Mech. Time-Depend. Mat.*, 3(1):49–69, 1999.
- [84] E.T.J. Klompen, L.E. Govaert, and H.E.H. Meijer. Nonlinear viscoelastic behavior of thermorheologically complex materials. *Proceedings 11th Conference DYFP*, pages 450–453, 2000.
- [85] E.T.J. Klompen, T.A.P. Engels, L.E. Govaert, and H.E.H. Meijer. Modeling of the postyield response of glassy polymers: Influence of thermomechanical history. *Macromolecules*, 38(16):6997–7008, 2005.
- [86] E.T.J. Klompen, T.A.P. Engels, L.C.A. van Breemen, P.J.G. Schreurs, L.E. Govaert, and H.E.H. Meijer. Quantitative prediction of long-term failure of polycarbonate. *Macromolecules*, 38(16):7009–7017, 2005.
- [87] R.S. Kody and D.C. Martin. Quantitative characterization of surface deformation in polymer composites using digital image analysis. *Polym. Eng. Sci.*, 36(2):298–304, 1996.
- [88] P.L. Larsson and S. Carlsson. On microindentation of viscoelastic polymers. *Polym. Test.*, 17:49–75, 1998.
- [89] P.L. Larsson, A.E. Giannakopoulos, E. Söderlund, D.J. Rowcliffe, and R. Vestergaard. Analysis of Berkovich indentation. *Int. J. Solids Struct.*, 33(2):221–248, 1996.
- [90] C.L. Lawson and R.J. Hanson. *Solving least squares problems*. Prentice-Hall, Englewood Cliffs, 1974.
- [91] H. Leaderman. *Elastic and Creep Properties of Filamentous Materials and Other High Polymers*. The Textile Foundation, Washington, DC, 1943.
- [92] J.H. Lee, G.H. Xu, and H. Liang. Experimental and numerical analysis of friction and wear behavior of polycarbonate. *Wear*, 250-251(PART 2):1541–1556, 2001.

- [93] H.X. Li and C.P. Buckley. Evolution of strain localization in glassy polymers: A numerical study. *Int. J. Sol. Struct.*, 46(7-8):1607–1623, 2009.
- [94] Y. Liu and R.W. Truss. Study of tensile yielding of isotactic polypropylene. *J. Polym. Sci., Part B: Polym. Phys.*, 32(12):2037–2047, 1994.
- [95] Y. Lu and D.M. Shinozaki. Deep penetration micro-indentation testing of high density polyethylene. *Mater. Sci. Eng. A*, 249(1-2):134–144, 1998.
- [96] Y. Lu and D.M. Shinozaki. Microindentation induced debonding of polymer thin films from rigid substrates. *J. Mater. Sci.*, 37:1283–1293, 2002.
- [97] K.C. Ludema and D. Tabor. The friction and visco-elastic properties of polymeric solids. *Wear*, 9(5):329–348, 1966.
- [98] D.J. Matz, W.G. Guldemond, and S.L. Cooper. Delayed yielding in glassy polymers. *J. Polym. Sci. Part A-2 Polym. Phys.*, 10(10):1917–1930, 1972.
- [99] N.G. McCrum. Sequential relaxation as the mechanism of physical ageing in amorphous polymers. *Polym. Commun. (Guildford Engl)*, 25(1):2–4, 1984.
- [100] K.G. McLaren and D. Tabor. Visco-elastic properties and the friction of solids: Friction of polymers: Influence of speed and temperature. *Nature*, 197(4870):856–858, 1963.
- [101] H.E.H. Meijer and L.E. Govaert. Multi-scale analysis of mechanical properties of amorphous polymer systems. *Macromol. Chem. Phys.*, 204(2):274–288, 2003.
- [102] L. Monnerie, J.L. Halary, and H.-H. Kausch. Deformation, yield and fracture of amorphous polymers: Relation to the secondary transitions. *Adv. Pol. Sc.*, 187:215–364, 2005.
- [103] MSC.Software. *MSC.Marc Volume B: Element Library*. MSC.Software GmbH, 2006.
- [104] MSC.Software. *MSC.Marc Volume A: Theory and User Information*. MSC.Software GmbH, 2006.
- [105] A.D. Mulliken and M.C. Boyce. Mechanics of the rate-dependent elastic-plastic deformation of glassy polymers from low to high strain rates. *Int. J. Solids Struct.*, 43(5): 1331–1356, 2006.
- [106] Y. Nanzai. Plastic deformation mechanism in pmma under creep stress. *JSME Int. J., Ser.-A: Mech. Mat. Eng.*, 37(2):149–154, 1994.
- [107] I. Narisawa and A.F. Yee. crazing and fracture of polymers. *Mater. Sci. Technol. A Comprehensive Treatment*, 12:699–765, 1993.

- [108] R.P. Nimmer and J.T. Woods. An investigation of brittle failure in ductile, notch-sensitive thermoplastics. *Polym. Eng. Sci.*, 32(16):1126–1137, AUG 1992. ISSN 0032-3888.
- [109] P.A. O'Connell and G.B. McKenna. Large deformation response of polycarbonate: Time-temperature, time-aging time, and time-strain superposition. *Polym. Eng. Sci.*, 37(9): 1485–1495, 1997.
- [110] W.C. Oliver and G.M. Pharr. An improved technique for determining hardness and elastic-modulus using load and displacement sensing indentation experiments. *J. Mat. Res.*, 7(6):1564 – 1583, 1992.
- [111] W.C. Oliver and G.M. Pharr. Measurement of hardness and elastic modulus by instrumented indentation: Advances in understanding and refinements to methodology. *J. Mat. Res.*, 19(1):3–20, 2004.
- [112] C.G.N. Pelletier, E.C.A. Dekkers, L.E. Govaert, J.M.J. den Toonder, and H.E.H. Meijer. The influence of indenter-surface misalignment on the results of instrumented indentation tests. *Polym. Test.*, 26(7):949–959, 2007.
- [113] C.G.N. Pelletier, J.M.J. Den Toonder, L.E. Govaert, N. Hakiri, and M. Sakai. Quantitative assessment and prediction of contact area development during spherical tip indentation of glassy polymers. *Philos. Mag.*, 88(9):1291–1306, 2008.
- [114] H. Pelletier, A.L. Durier, C. Gauthier, and R. Schirrer. Viscoelastic and elastic-plastic behaviors of amorphous polymeric surfaces during scratch. *Tribol. Int.*, 41(11):975–984, 2008.
- [115] H. Pelletier, C. Gauthier, and R. Schirrer. Experimental and finite-element analysis of scratches on amorphous polymeric surfaces. *Mec. Ind.*, 9(4):261–271, 2008.
- [116] H. Pelletier, C. Gauthier, and R. Schirrer. Experimental and finite-element analysis of scratches on amorphous polymeric surfaces. *Proceedings of the Institution of Mechanical Engineers, Part J: Journal of Engineering Tribology*, 222(3):221–230, 2008.
- [117] H. Pelletier, C. Gauthier, and R. Schirrer. Strain and stress fields during scratch tests on amorphous polymers: Influence of the local friction. *Tribol. Letters*, 32(2):109–116, 2008.
- [118] H. Pelletier, C. Gauthier, and R. Schirrer. Experimental measurement and numerical simulation of the plastic strain during indentation and scratch tests on polymeric surfaces. *J. Mater. Res.*, 24(3):1184–1196, 2009.
- [119] S. Rabinowitz, I.M. Ward, and J.S.C. Parry. The effect of hydrostatic pressure on the shear yield behaviour of polymers. *J. Mater. Sci.*, 5(1):29–39, 1970.

- [120] T. Ree and H. Eyring. Theory of non-newtonian flow. i. solid plastic system. *J. Appl. Phys.*, 26(7):793–800, 1955.
- [121] J.A. Roetling. Yield stress behaviour of polymethylmethacrylate. *Polymer*, 6(6):311–317, 1965.
- [122] J.A. Roetling. Yield stress behaviour of poly(ethyl methacrylate) in the glass transition region. *Polymer*, 6(11):615–619, 1965.
- [123] J.A. Roetling. Yield stress behaviour of isotactic polypropylene. *Polymer*, 7(7):303–306, 1966.
- [124] M. Sakai, N. Hakiri, and T. Miyajima. Instrumented indentation microscope: A powerful tool for the mechanical characterization in microscales. *J. Mat. Res.*, 21(9):2298–2303, 2006.
- [125] J.A. Sauer, D.R. Mears, and K.D. Pae. Effects of hydrostatic pressure on the mechanical behaviour of polytetrafluoroethylene and polycarbonate. *Eur. Polym. J.*, 6(7):1015–1022, 1970.
- [126] R.A. Schapery. On characterization of nonlinear viscoelastic materials. *Polym. Eng. Sci.*, 9(4):295–310, 1969.
- [127] F. Schwarzl and A.J. Staverman. Time-temperature dependence of linear viscoelastic behavior. *J. Appl. Phys.*, 23(8):838–843, 1952.
- [128] C. Soanes and A. Stevenson. *Oxford Dictionary of English (Dictionary)*. Oxford University Press, August 2005. ISBN 0198610572.
- [129] W.A. Spitzig and O. Richmond. Effect of hydrostatic pressure on the deformation behavior of polyethylene and polycarbonate in tension and compression. *Polym Eng Sci*, 19(16):1129–1139, 1979.
- [130] L.C.E. Struik. *Physical Ageing in Amorphous Polymers and Other Materials*. Elsevier, Amsterdam, 1978.
- [131] B.H. Stuart. Scratch friction studies of polycarbonate. *Polym. Test.*, 16(5):517–522, 1997.
- [132] B.H. Stuart and B.J. Briscoe. Scratch hardness studies of poly(ether ether ketone). *Polymer*, 37(17):3819–3824, 1996.
- [133] S. Swaddiwudhipong, L.H. Poh, J. Hua, Z.S. Liu, and K.K. Tho. Modeling nano-indentation tests of glassy polymers using finite elements with strain gradient plasticity. *Mat. Sci. Eng. A*, 404(1-2):179–187, 2005.

- [134] D. Tabor. The mechanism of rolling friction. *Philos. Mag.*, 43(345):1055–1059, 1952. ISSN 0031-8086.
- [135] D. Tabor. *Hardness of metals*. Clarendon press, Oxford, 1951.
- [136] M. Takano and L. E. Nielsen. Notch sensitivity of polymeric materials. *J. Appl. Polym. Sci.*, 20(8):2193–2207, 1976.
- [137] T.A. Tervoort and L.E. Govaert. Strain hardening behavior of polycarbonate in the glassy state. *J. Rheol.*, 44(6):1263 – 1277, 2000.
- [138] T.A. Tervoort, E.T.J. Klompen, and L.E. Govaert. A multi-mode approach to finite, three-dimensional, nonlinear viscoelastic behavior of polymer glasses. *J. Rheol.*, 40(5):779–797, 1996.
- [139] T.A. Tervoort, R.J.M. Smit, W.A.M. Brekelmans, and L.E. Govaert. A constitutive equation for the elasto-viscoplastic deformation of glassy polymers. *Mech. Time-Depend. Mat.*, 1(3):269–291, 1997.
- [140] T.A. Tervoort, R.J.M. Smit, W.A.M. Brekelmans, and L.E. Govaert. A constitutive equation for the elasto-viscoplastic deformation of glassy polymers. *Mech. Time-Dep. Mater.*, 1(3):269–291, 1998.
- [141] A.V. Tobolsky. Stress relaxation studies of the viscoelastic properties of polymers. *J. Appl. Phys.*, 27(7):673–685, 1956.
- [142] N.W. Tsjoegl. *The Phenomenological Theory of Linear Viscoelastic Behavior: An Introduction*. Springer-Verlag, Berlin, 1989.
- [143] K.C. Valanis. Theory of viscoplasticity without a yield surface .1. General theory. *Arch. Mech.*, 23(4):517–533, 1971.
- [144] L.C.A. van Breemen. Spectrum determination routine, 2009. URL <http://www.mate.tue.nl/~vanbreemen/>.
- [145] L.C.A. van Breemen, T.A.P. Engels, L.E. Govaert, and H.E.H. Meijer. Modeling thermorheologically complex phenomena in the post-yield response. *Proceedings 13th Conference DYFP*, pages 299–301, 2006.
- [146] L.C.A. van Breemen, T.A.P. Engels, C.G.N. Pelletier, L.E. Govaert, and J.M.J. den Toonder. Numerical simulation of flat-tip micro-indentation of glassy polymers: influence of loading speed and thermodynamic state. *Philos. Mag.*, 89:677–696, 2009.
- [147] L.C.A. van Breemen, E.T.J. Klompen, L.E. Govaert, and H.E.H. Meijer. Constitutive modeling of polymer glasses: a multi-mode approach. *J. Mech. Phys. Sol.*, 2009. submitted.

- [148] H.G.H. Van Melick, O.F.J.T. Bressers, J.M.J. Den Toonder, L.E. Govaert, and H.E.H. Meijer. A micro-indentation method for probing the craze-initiation stress in glassy polymers. *Polymer*, 44(8):2481–2491, 2003.
- [149] H.G.H. Van Melick, L.E. Govaert, and H.E.H. Meijer. On the origin of strain hardening in glassy polymers. *Polymer*, 44(8):2493–2502, 2003.
- [150] H.G.H. Van Melick, L.E. Govaert, and H.E.H. Meijer. Localisation phenomena in glassy polymers: Influence of thermal and mechanical history. *Polymer*, 44(12):3579–3591, 2003.
- [151] M.R. VanLandingham, J.S. Villarrubia, W.F. Guthrie, and G.F. Meyers. Nanoindentation of polymers: an overview. *Macromolecular Symposia*, 167:15–44, 2001.
- [152] M. Wendlandt, T.A. Tervoort, and U.W. Suter. Non-linear, rate-dependent strain-hardening behavior of polymer glasses. *Polymer*, 46(25):11786–11797, 2005.
- [153] M.A. Wilding and I.M. Ward. Creep and recovery of ultra high modulus polyethylene. *Polymer*, 22(7):870–876, 1981.
- [154] J.A. Williams. Analytical models of scratch hardness. *Tribol. Int.*, 29(8):675–694, 1996.
- [155] S.C. Wright, Y. Huang, and N.A. Fleck. Deep penetration of polycarbonate by a cylindrical punch. *Mech. Mater.*, 13(4):277–284, 1992.
- [156] J.J. Wu and C.P. Buckley. Plastic deformation of glassy polystyrene: A unified model of yield and the role of chain length. *J. Polym. Sci., Part B: Polym. Phys.*, 42:2027–2040, 2004.
- [157] P.D. Wu and E. Van Der Giessen. On improved network models for rubber elasticity and their applications to orientation hardening in glassy polymers. *J. Mech. Phys. Solids*, 41(3):427–456, 1993.
- [158] P.D. Wu and E. Van Der Giessen. Analysis of shear-band propagation in amorphous glassy-polymers. *Int. J. Sol. Struct.*, 31(11):1493–1517, 1994.
- [159] P.D. Wu and E. Van Der Giessen. On neck propagation in amorphous glassy-polymers under plane-strain tension. *Int. J. Plast.*, 11(3):211–235, 1995.
- [160] C. Xiang, H.-J. Sue, J. Chu, and B. Coleman. Scratch behavior and material property relationship in polymers. *J. Polym. Sci., Part B: Polym. Phys.*, 39(1):47–59, 2001.
- [161] S.W. Zhang. State-of-the-art of polymer tribology. *Tribol. Int.*, 31(1-3):49–60, JAN-MAR 1998. ISSN 0301-679X.

Samenvatting

Steeds vaker worden polymeren toegepast in applicaties waar goede wrijvings- en slijtage-eigenschappen gewenst zijn. Voorbeelden hiervan zijn de cups in kunstgewrichten en in lagers. Waarom, voornamelijk semikristallijne, polymeren zo goed presteren is echter niet geheel duidelijk en er bestaat geen correlatie tussen intrinsieke polymere eigenschappen en het geobserveerde wrijvings- en slijtagegedrag. Dit proefschrift presenteert een systematische identificatie van de rol van intrinsieke eigenschappen van glasachtige polymeren op single-asperity metingen.

De analyse wordt uitgevoerd door gebruik te maken van een hybride numeriek/experimentele aanpak. Het numerieke deel gebruikt een constitutief model dat het intrinsiek gedrag van polymere glazen perfect beschrijft. De interactie tussen indenter en polymeer kan worden beïnvloed door gebruik te maken van bestaande wrijvingsmodellen.

Het experimentele gedeelte betreft de ontwikkeling van reproduceerbare indentatie en single-asperity sliding experimenten. Deze worden in een later stadium vergeleken met de simulaties, voordat conclusies kunnen worden getrokken. De basis in de eindige elementensimulaties is het constitutief model ontwikkeld in onze groep. Dit model beschrijft nauwkeurig het intrinsieke deformatiegedrag van glasachtige polymeren. Het is toegepast in het bestuderen van reklokalisatie fenomenen, en tevens om de levensduur van producten te voorspellen.

De keuze voor glasachtige polymeren is duidelijk niet vanwege hun relevantie in wrijvings- en slijtageapplicaties, maar vanwege het feit dat ze een goed gekarakteriseerde klasse van polymeren vertegenwoordigen. Allereerst dienen enkele beperkingen van het huidige model verwijderd te worden. Het intrinsieke gedrag voor vloeï is niet-lineair visco-elastisch. Daardoor levert het een significante bijdrage aan het geobserveerde niet-homogene deformatie-gedrag, zoals bijvoorbeeld bij indentatie en single-asperity wrijvingsmetingen. Tot op heden wordt het gedrag voor vloeï gemodelleerd als een lineair elastische samendrukbare vaste stof. Het resultaat is dat details van indentatie en het ontlasten na indentatie niet kwantitatief kunnen worden beschreven. De oplossing is redelijk rechttoe-rechtaan: in plaats van één relaxatietijd

dient een spectrum van relaxatietijden gebruikt te worden. Dit gedrag is gemodelleerd via een multi-mode benadering. Het verbeterde model is nu ook daadwerkelijk in staat om kwantitatief de indentatierespons van polycarbonaat te beschrijven voor verschillende indenter-geometrieën.

Een tweede beperking van het huidige model: het kan niet overweg met meerdere relaxatiemechanismen, zoals in situaties waar meer dan één moleculair proces bijdraagt aan de spanning. Deze materiaalrespons wordt typisch waargenomen bij hoge reksnelheden en lage temperaturen. Het manifesteert zich als een verandering in helling in de afhankelijkheid van de vloeispanning van (de logaritme van) de reksnelheid. De oplossing is het toevoegen van een tweede vloeiproces met zijn eigen niet-lineariteit. Dat resulteert in een multi-proces model. Een glasachtig polymeer dat dit gedrag laat zien is poly(methyl methacrylaat). Ook hier wordt een kwantitatieve voorspelling van het indentatiegedrag bereikt.

In het algemeen wordt een gemeten wrijvingskracht toegewezen aan een additief samenspel tussen deformatie- en adhesie-gerelateerde componenten. Dit suggereert dat beide componenten onafhankelijk opereren en bijdragen aan de respons. Terwijl decompositie in onafhankelijke bijdragen onmogelijk is in een experimentele omgeving, kan het in een numerieke omgeving wel onafhankelijk bestudeerd worden. Simulaties zonder adhesieve interactie tussen een diamanten indenter en een polymeer laten nagenoeg geen invloed zien van de glijnsnelheid op de frictiekracht; experimenten laten dit duidelijk wél zien. Wanneer een additieve decompositie zou gelden, betekent dit automatisch dat de adhesieve component snelheids- en dus tijdsafhankelijk is. Het toepassen van een wrijvingsmodel, i.e. Amontons-Coulomb wrijvingsmodel, tussen indenter tip en polymeer, bewijst dat een additieve decompositie niet mogelijk is. Eveneens bewijst het dat het geobserveerde macroscopisch gedrag het resultaat is van kleine veranderingen in lokale processen. Door toepassing van dit wrijvingsmodel, vormt zich een zogenaamde boeggolf voor de indenter tijdens het glijden. Dit resulteert in een toename van contactoppervlak en dus ook in een toename van de wrijvingskracht. De consequentie is: het tijdsafhankelijke gedrag dat op experimentele schaal wordt waargenomen kan alleen worden toegewezen aan het intrinsieke gedrag van het polymeer. Daarnaast wordt er in numerieke simulaties aangetoond wat de effecten zijn wanneer er intrinsieke materiaaleigenschappen, zoals strain hardening en thermodynamische toestand, veranderd worden. Er is een eerste stap gezet om tribologie, de leer van wrijving en slijtage, voor polymeren te leren begrijpen.

Dankwoord

Zoals iedereen die mij een beetje kent wel weet, ben ik een man van weinig woorden. Toch wil ik via deze pagina iedereen uit de M@te-groep met wie ik de afgelopen jaren met veel plezier heb samengewerkt bedanken voor hun inzet en prettige en tevens inspirerende werkomgeving.

Een woord van dank gaat uit naar de ondersteunende staf; de drie-eenheid op het secretariaat, Marleen, Yvon en Alice, de mannen van de werkplaats, Sjef (a.k.a. the master of prupkes), Rob en Pieter, en de heren van systeem beheer, Patrick en in het bijzonder Leo: bedankt voor de ondersteuning bij mijn zware sommen en voor de *illegale* rekentijd die ik op de nieuwe cluster nodes heb kunnen benutten. Ook de studenten, waarvan sommige inmiddels collega promovendi, die mij geholpen hebben gedurende mijn promotie, verdienen een plek op deze pagina; in willekeurige volgorde: Matthijs den Hartog, Tim van Erp, Joris Wismans, Erik Feron, Elgar Kleijne, Niek de Kruijf, Dirk Senden, Swen Hellenbrand, Peter Roozemond, Paul van Beers, Bennie Luijten, Joep Naninck, Daniel Beckers, Jeroen van Beeck en Mark Haring.

Als familiemens wil ik natuurlijk mijn familie bedanken voor de gezelligheid en broodnodige ontspanning. In het speciaal bedank ik mijn ouders, jullie hebben altijd in mij geloofd, mij gemotiveerd om mezelf te ontplooiën op vele fronten, en mij van jongs af aan geleerd verder te kijken dan mijn neus lang is. Last but absolutely not least, Daantjuh, mijn steun en toeverlaat, samen gaan we van het leven een groot feest maken!

And may the Schwartz be with you all!

Lambert
Eindhoven, Mei 2009

Curriculum vitae

Lambert van Breemen was born on the twenty-eighth of April 1977 in Velsen, the Netherlands. He graduated from his pre-university secondary education in 1996 at the Norbertus College in Roosendaal. He then enrolled as a student in the department of Mechanical Engineering at the Eindhoven University of Technology. After receiving his Bachelors degree in August 1999, he became chairman of the Cultural Festival Virus. In August 2001 he continued his study and joined the Polymer Technology group chaired by prof.dr.ir. Han E.H. Meijer, where in December 2004, under supervision of dr.ir. Leon E. Govaert and dr.ir. Piet J.A. Schreurs, he received his Masters degree (great appreciation) with the thesis entitled 'Implementation and validation of a 3D model describing glassy polymer behaviour'. As part of his master track he performed an international internship at the ESRF in Grenoble, France.

After completion of his Masters degree he was employed as a PhD student in the same group, where he worked on contact phenomena of glassy polymers under supervision of dr.ir. Leon E. Govaert and prof.dr.ir. Han E.H. Meijer. In February 2008 he received the Best plenary lecture award at the Dutch Polymer Days in Lunteren. During his PhD he successfully completed the postgraduate course Register Polymer Science of the National Dutch Research School PTN (Polymeer Technologie Nederland) and is given the title Registered Polymer Scientist as of February 2008. The course consists of the following modules: A - Polymer Chemistry, B - Polymer Physics, C - Polymer Properties, D - Polymer Rheology, E - Polymer Processing and π - Polymer Innovations.

List of publications

This thesis has resulted in the following publications:

- L.C.A. van Breemen, E.T.J. Klompen, L.E. Govaert and H.E.H. Meijer, Constitutive modelling of polymer glasses: a multi-mode approach, *Journal of the Mechanics and Physics of Solids*, *submitted*, (2009)
- L.C.A. van Breemen, T.A.P. Engels, L.E. Govaert and H.E.H. Meijer, Constitutive modelling of polymer glasses: a multi-mode-multi-process approach, *Journal of the Mechanics and Physics of Solids*, *submitted*, (2009)
- L.C.A. van Breemen, T.A.P. Engels, C.G.N. Pelletier, L.E. Govaert and J.M.J. den Toonder, Numerical simulation of flat-tip micro-indentation of glassy polymers: influence of loading speed and thermodynamic state, *Philosophical Magazine*, 89(8) 677–696, (2009)
- L.C.A. van Breemen, L.E. Govaert and H.E.H. Meijer, Friction in a single-asperity contact: relation to intrinsic mechanical properties of glassy polymers, *Tribology International*, *submitted*, (2009)

The author contributed to a number of publications outside the scope of this thesis:

- T.A.P. Engels, L.C.A. van Breemen, L.E. Govaert and H.E.H. Meijer, Predicting age-induced embrittlement of glassy polymers, *Polymer*, *submitted*, (2009)
- T.A.P. Engels, B.A.G. Schrauwen, L.C.A. van Breemen and L.E. Govaert, Predicting the yield stress of polymer glasses directly from processing conditions: application to miscible systems, *International Polymer Processing*, 14(2), 167-173, (2009)
- E.T.J. Klompen, T.A.P. Engels, L.C.A. van Breemen, P.J.G. Schreurs, L.E. Govaert and H.E.H. Meijer, Quantitative prediction of long-term failure of Polycarbonate, *Macromolecules*, 38(16), 7009-7017, (2005)

- J.A.W. van Dommelen, B.A.G. Schrauwen, L.C.A. van Breemen and L.E. Govaert, Micromechanical modeling of the tensile behavior of oriented polyethylene, *Journal of Polymer Science, Polymer Physics Edition*, 42(16), 2983-2994, (2004)
- B.A.G. Schrauwen, L.C.A. van Breemen, A.B. Spoelstra, L.E. Govaert, G.W.M. Peters and H.E.H. Meijer, Structure, deformation and failure of flow-oriented semi-crystalline polymers, *Macromolecules*, 37(23), 8618-8633, (2004)

The following publications are in preparation, and soon to be submitted:

- M. Geerligs, L.C.A. van Breemen, P.A.J. Ackermans, G.W.M. Peters, C.W.J Oomens and F.P.T. Baaijens, Can the anisotropic behaviour of the epidermis be explained by its layered structure?, in preparation for *Nature/Journal of Biomechanics*
- M. Geerligs, L.C.A. van Breemen, P.A.J. Ackermans, G.W.M. Peters, C.W.J Oomens and F.P.T. Baaijens, A new indentation technique to determine the mechanical properties of epidermis and stratum corneum in vitro, in preparation for *Biomaterials*